

Nanotechnologies for Biosensor and Biochip

Guest Editors: Moon Il Kim, Tae Jung Park, Elena E. Paskaleva,
Fangfang Sun, Jin W. Seo, and Krunal K. Mehta





Nanotechnologies for Biosensor and Biochip

Journal of Nanomaterials

Nanotechnologies for Biosensor and Biochip

Guest Editors: Moon Il Kim, Tae Jung Park, Elena E. Paskaleva,
Fangfang Sun, Jin W. Seo, and Krunal K. Mehta



Copyright © 2015 Hindawi Publishing Corporation. All rights reserved.

This is a special issue published in "Journal of Nanomaterials." All articles are open access articles distributed under the Creative Commons Attribution License, which permits unrestricted use, distribution, and reproduction in any medium, provided the original work is properly cited.

Editorial Board

Domenico Acierno, Italy
Katerina Aifantis, USA
Nageh K. Allam, USA
Margarida Amaral, Portugal
Martin Andersson, Sweden
Raul Arenal, Spain
Ilaria Armentano, Italy
Vincenzo Baglio, Italy
Lavinia Balan, France
Thierry Baron, France
Andrew R. Barron, USA
Reza Bayati, USA
Hongbin Bei, USA
Daniel Bellet, France
Stefano Bellucci, Italy
Enrico Bergamaschi, Italy
Samuel Bernard, France
Debes Bhattacharyya, New Zealand
Sergio Bietti, Italy
Giovanni Bongiovanni, Italy
Theodorian Borca-Tasciuc, USA
Mohamed Bououdina, Bahrain
Torsten Brezesinski, Germany
C. Jeffrey Brinker, USA
Christian Brosseau, France
Philippe Caroff, Australia
Victor M. Castaño, Mexico
Albano Cavaleiro, Portugal
Bhanu P. S. Chauhan, USA
Shafiu Chowdhury, USA
Jin-Ho Choy, Republic of Korea
Kwang-Leong Choy, UK
Yu-Lun Chueh, Taiwan
Elisabetta Comini, Italy
Giuseppe Compagnini, Italy
David Cornu, France
Miguel A. Correa-Duarte, Spain
Pantaleo D. Cozzoli, Italy
Shadi A. Dayeh, USA
Luca Deseri, USA
Yong Ding, USA
Philippe Dubois, Belgium
Zehra Durmus, Turkey
Joydeep Dutta, Oman
Ali Eftekhari, USA
Jeffrey Elam, USA
Samy El-Shall, USA
Ovidiu Ersen, France
Claude Estournès, France
Andrea Falqui, KSA
Matteo Ferroni, Italy
Elena J. Foster, USA
Ilaria Fratoddi, Italy
Alan Fuchs, USA
Miguel A. Garcia, Spain
Siddhartha Ghosh, Singapore
P. K. Giri, India
Russell E. Gorga, USA
Jihua Gou, USA
Jean M. Greneche, France
Smrati Gupta, Germany
Kimberly Hamad-Schifferli, USA
Simo-Pekka Hannula, Finland
Michael Harris, USA
Yasuhiko Hayashi, Japan
F. Hernandez-Ramirez, Spain
Michael Z. Hu, USA
Nay Ming Huang, Malaysia
Shaoming Huang, China
David Hui, USA
Zafar Iqbal, USA
Balachandran Jeyadevan, Japan
Xin Jiang, Germany
Rakesh Joshi, Australia
Jeong-won Kang, Republic of Korea
Hassan Karimi-Maleh, Iran
Antonios Kelarakis, UK
Alireza Khataee, Iran
Ali Khorsand Zak, Iran
Philippe Knauth, France
Ralph Krupke, Germany
Christian Kübel, Germany
Prashant Kumar, UK
Michele Laus, Italy
Eric Le Bourhis, France
Burtrand Lee, USA
Jun Li, Singapore
Meiyong Liao, Japan
Shijun Liao, China
Silvia Licocchia, Italy
Wei Lin, USA
Nathan C. Lindquist, USA
Jun Liu, USA
Zainovia Lockman, Malaysia
Nico Lovergine, Italy
Jim Low, Australia
Jue Lu, USA
Songwei Lu, USA
Ed Ma, USA
Laura M. Maestro, Spain
Gaurav Mago, USA
Muhamamd A. Malik, UK
Devanesan Mangalaraj, India
Sanjay R. Mathur, Germany
Tony McNally, UK
Yogendra Mishra, Germany
Paulo Cesar Morais, Brazil
Paul Munroe, Australia
Jae-Min Myoung, Republic of Korea
Rajesh R. Naik, USA
Albert Nasibulin, Russia
Toshiaki Natsuki, Japan
Koichi Niihara, Japan
Natalia Noginova, USA
Sherine Obare, USA
Won-Chun Oh, Republic of Korea
Atsuto Okamoto, Japan
Abdelwahab Omri, Canada
Ungyu Paik, Republic of Korea
Piersandro Pallavicini, Italy
Edward A. Payzant, USA
Alessandro Pegoretti, Italy
Ton Peijs, UK
Oscar Perales-Pérez, Puerto Rico
Jorge Pérez-Juste, Spain
Alexey P. Popov, Finland
Philip D. Rack, USA
Peter Reiss, France
Orlando Rojas, USA
Marco Rossi, Italy
Ilker S. Bayer, Italy
Cengiz S. Ozkan, USA
Sudipta Seal, USA
Shu Seki, Japan
Vladimir Šepelák, Germany

Huaiyu Shao, Japan
Prashant Sharma, USA
Donglu Shi, USA
Bhanu P. Singh, India
Surinder Singh, USA
Vladimir Sivakov, Germany
Ashok Sood, USA
Adolfo Speghini, Italy
Marinella Striccoli, Italy
Xuping Sun, KSA
Ashok K. Sundramoorthy, USA
Angelo Taglietti, Italy
Bo Tan, Canada

Leander Tapfer, Italy
Valeri P. Tolstoy, Russia
Muhammet S. Toprak, Sweden
Ramon Torrecillas, Spain
Achim Trampert, Germany
Takuya Tsuzuki, Australia
Tamer Uyar, Turkey
Bala Vaidhyanathan, UK
Luca Valentini, Italy
Rajender S. Varma, USA
Ester Vazquez, Spain
Antonio Villaverde, Spain
Ajayan Vinu, Australia

Ruibing Wang, Macau
Shiren Wang, USA
Yong Wang, USA
Magnus Willander, Sweden
Ping Xiao, UK
Zhi Li Xiao, USA
Yangchuan Xing, USA
Doron Yadlovker, Israel
Yoke K. Yap, USA
Kui Yu, Canada
William Yu, USA
Michele Zappalorto, Italy
Renyun Zhang, Sweden

Contents

Nanotechnologies for Biosensor and Biochip, Moon Il Kim, Tae Jung Park, Elena E. Paskaleva, Fangfang Sun, Jin W. Seo, and Krunal K. Mehta
Volume 2015, Article ID 420734, 2 pages

Recent Research Trends and Future Prospects in Nanozymes, Ho Yun Shin, Tae Jung Park, and Moon Il Kim
Volume 2015, Article ID 756278, 11 pages

Autophagy in RAW264.7 Cells Treated with Surface-Functionalized Graphene Oxides, Chang Seok Park, Kyoung Soon Choi, In Won Park, Jae Woo Jung, Jae Chol Choi, Jae Yeol Kim, Byoung Whui Choi, Yu Geun Kim, Jong Wook Shin, and Soo Young Kim
Volume 2015, Article ID 704789, 8 pages

Colorimetric Detection System for *Salmonella typhimurium* Based on Peroxidase-Like Activity of Magnetic Nanoparticles with DNA Aptamers, Ji Young Park, Ha Young Jeong, Moon Il Kim, and Tae Jung Park
Volume 2015, Article ID 527126, 9 pages

Density Functional Investigation of Graphene Doped with Amine-Based Organic Molecules, Yeun Hee Hwang, Hyang Sook Chun, Kang Min Ok, Kyung-Koo Lee, and Kyungwon Kwak
Volume 2015, Article ID 917637, 9 pages

Nanotextured Morphology of Poly(methyl methacrylate) and Ultraviolet Curable Poly(urethane acrylate) Blends via Phase Separation, Ju-Hyung Kim, Joon H. Kim, and Soonmin Seo
Volume 2015, Article ID 593084, 8 pages

Detection of Biomarkers Using LSPR Substrate with Gold Nanoparticle Array, Young Min Bae, Seung Oh Jin, Insoo Kim, Ki Young Shin, Duchang Heo, and Dong-Goo Kang
Volume 2015, Article ID 302816, 6 pages

Editorial

Nanotechnologies for Biosensor and Biochip

**Moon Il Kim,¹ Tae Jung Park,² Elena E. Paskaleva,³ Fangfang Sun,⁴
Jin W. Seo,⁵ and Krunal K. Mehta⁶**

¹Department of BioNano Technology, Gachon University, 1342 Seongnamdae-ro, Sujeong-gu, Seongnam, Gyeonggi 461-701, Republic of Korea

²Department of Chemistry, Chung-Ang University, 84 Heukseok-ro, Dongjak-gu, Seoul 06974, Republic of Korea

³Center for Biotechnology and Interdisciplinary Studies, Rensselaer Polytechnic Institute, Troy, NY 12180, USA

⁴College of Life Information Science and Instrument Engineering, Hangzhou Dianzi University, Xiasha, Hangzhou, Zhejiang 310018, China

⁵Departement Materiaalkunde (MTM), KU Leuven, Kasteelpark Arenberg 44, Bus 2450, 3001 Leuven, Belgium

⁶Pivotal Purification Process Development, Amgen, Inc., Cambridge, MA 02142, USA

Correspondence should be addressed to Moon Il Kim; moonil@gachon.ac.kr

Received 3 December 2015; Accepted 3 December 2015

Copyright © 2015 Moon Il Kim et al. This is an open access article distributed under the Creative Commons Attribution License, which permits unrestricted use, distribution, and reproduction in any medium, provided the original work is properly cited.

The biosensing devices are characterized by their biological receptors, which have specificity to their corresponding analytes. These analytes are a vast and diverse group of biological molecules, DNAs, proteins (such as antibodies), fatty acids, or entire biological systems, such as pathogenic bacteria, viruses, cancerous cells, or other living organisms. A main challenge in the development of biosensor applications is the efficient recognition of a biological signal in a low signal-to-noise ratio environment, and its transduction into an electrochemical, optical, or other signals. The advent of nanomaterial technology greatly increased the potential for achieving exquisite sensitivity of such devices, due to the innate high surface-to-volume ratio and high reactivity of the nanomaterial. The second major challenge facing the biosensor application, that of scalability, is addressed by multiplexing and miniaturizing of the biosensor devices into a biochip. In recent years, biosensor and biochip technologies have made significant progress by taking advantages of diverse kinds of nanomaterials that are derived from nanotechnology [1–3].

These materials exhibit unique optical, electronic, magnetic, and catalytic properties, which can be essentially utilized to develop novel biosensors that yield highly enhanced sensitivity, selectivity, and other attributes. Furthermore, the newly developed nanomaterials provide a particularly useful

platform for the development of biochips that are ideally suited to meet the demands of biomolecules to facilitate various kinds of biological events. In this special issue, to provide chemists, biochemists, material engineers, and bioengineers with a perspective on the current state-of-the-art of this emerging nanobiotechnological research field, several excellent research results and a comprehensive review on nanotechnologies for biosensor and biochip were reported.

The paper by Y. M. Bae et al. is focused on the applicability of localized surface plasmon resonance (LSPR) substrate with gold nanoparticle array to detect relevant biomarkers. In this work, the LSPR substrate was first fabricated with a lift-off process and its LSPR phenomenon was confirmed by measuring the optical transmission level of the substrate. Then, the antibodies with a high affinity toward target molecules were immobilized on the gold nanoparticle array. The immobilization was confirmed by observing the shift of LSPR peak of the resultant substrate. These new LSPR substrates conjugated with antibodies were successfully applied to detect low- and high-density lipoproteins, which are biomarkers for diagnosing and monitoring of cardiovascular disease.

The colorimetric activity of magnetic nanoparticles (MNPs) was employed to develop a unique biosensor. J. Y. Park et al. reported a colorimetric biosensor based on the peroxidase-like activity of magnetic nanoparticles and DNA

aptamers having a high affinity toward a target food pathogen *Salmonella typhimurium*. In this assay system, MNPs were first incubated with aptamers that specifically interact with the target bacterial cells, reducing the peroxidase activity of the MNPs through DNA-mediated shielding of the catalytic activity. After the addition of target *Salmonella* cells into the solution, specific aptamers on the MNPs interact with the *Salmonella*, consequently enhancing the peroxidase activity of the MNPs. Overall, the presence and quantity of target *Salmonella* cells were successfully detected by the colorimetric response produced from the peroxidase-like activity of MNPs. Based on the results, the authors propose that this label-free colorimetric biosensor would be invaluable for detecting DNA-DNA, DNA-protein, DNA-cell, and DNA-ligand interactions due to its ease of use, low cost, capability to detect with naked eye, and the high stability of MNPs.

C. S. Park et al. investigated the cytotoxicity, particularly autophagy, in RAW264.7 cells exposed to graphene oxide (GO) and its derivatives including dodecylamine-GO, reduced GO, and sodium dodecyl sulfate-reduced GO. They showed that all the GO types exerted cytotoxic effects on RAW264.7 cells in a concentration-dependent manner. Higher concentrations of the GO types downregulated the expression of PU.1, a unique transcription factor in monocytes and macrophages, and decreased the conversion of LC3A/B-I to LC3A/B-II, suggesting that PU.1 was associated with autophagy in RAW264.7 cells. These results suggest that surface-functionalized GOs exert cytotoxic effects in a concentration-dependent manner by changing the expression of critical genes and inducing autophagy in macrophages.

A binary immiscible polymer blended system with high stability is also reported by J.-H. Kim et al. In this article, domain structures of spin-coated immiscible poly(methyl methacrylate) (PMMA) and ultraviolet curable poly(urethane acrylate) (PUA) blends were studied using atomic force microscopy (AFM). Since the cross-linked PUA in the polymer-blended films provided strong chemical stability in various solvents, target materials for dissolution could be selectively available *via* a simple curing process. In addition, morphology of the PMMA/PUA blends, including domain size, height, and nanoscale features, could be easily controlled by changing composition of the blends. Based on the results, the authors suggest potentials for various applications related to nanotextured surfaces and soft lithography.

The electronic and molecular structure of doped graphene was theoretically investigated with solid-state density functional calculations. Y. H. Hwang et al. studied the graphene-organic molecule complex, referred to as organic doping in material science community. With the density functional calculations, the authors determined the role of amine-based aromatic compounds in graphene doping, binding to graphene through long-range interactions such as π - π interactions and C-H $\cdots\pi$ hydrogen bonding. The electronic structures of pristine graphene were compared to that of doped graphene to help understand the electronic structure of the material at molecular level. In addition to the investigation of the molecular interactions, the paper showed that screening of organic molecules would benefit

from a solid-state density functional calculation to predict the experimental results from doping or sensing organic molecules with graphene.

A comprehensive review on recent nanozyme (nanomaterial-based artificial enzymes) research is presented by H. Y. Shin et al. It covers the fundamentals and the applications for development of novel biosensors, immunoassays, cancer diagnostics, and therapeutics, as well as environmental engineering technologies. The review concludes with discussion on the current challenges and future prospects of using nanozymes in biotechnology.

We hope that this special issue will provide new insights and research motivation to the interested readers for further advancement in biosensor and biochip applications through state-of-the-art nanotechnology.

Acknowledgment

We would like to thank all authors for their valuable contributions to this special issue. We also would like to acknowledge the referees for their indispensable efforts to improve the quality of this special issue.

Moon Il Kim
Tae Jung Park
Elena E. Paskaleva
Fangfang Sun
Jin W. Seo
Krunal K. Mehta

References

- [1] Y. Song, W. Wei, and X. Qu, "Colorimetric biosensing using smart materials," *Advanced Materials*, vol. 23, no. 37, pp. 4215–4236, 2011.
- [2] H. Wei and E. Wang, "Nanomaterials with enzyme-like characteristics (nanozymes): next-generation artificial enzymes," *Chemical Society Reviews*, vol. 42, no. 14, pp. 6060–6093, 2013.
- [3] Y. Xia, Y. Xiong, B. Lim, and S. E. Skrabalak, "Shape-controlled synthesis of metal nanocrystals: simple chemistry meets complex physics?" *Angewandte Chemie—International Edition*, vol. 48, no. 1, pp. 60–103, 2009.

Review Article

Recent Research Trends and Future Prospects in Nanozymes

Ho Yun Shin,¹ Tae Jung Park,² and Moon Il Kim¹

¹Department of BioNano Technology, Gachon University, 1342 Seongnamdae-ro, Sujeong-gu, Seongnam, Gyeonggi 461-701, Republic of Korea

²Department of Chemistry, Chung-Ang University, 84 Heukseok-ro, Dongjak-gu, Seoul 156-756, Republic of Korea

Correspondence should be addressed to Tae Jung Park; tjpark@cau.ac.kr and Moon Il Kim; moonil@gachon.ac.kr

Received 21 July 2015; Accepted 17 November 2015

Academic Editor: Xuping Sun

Copyright © 2015 Ho Yun Shin et al. This is an open access article distributed under the Creative Commons Attribution License, which permits unrestricted use, distribution, and reproduction in any medium, provided the original work is properly cited.

Recently, nanomaterial-based enzyme mimetics (*nanozymes*) have attracted enormous interest. They exhibit unique advantages such as excellent robustness, stability, and low-cost production with easy scale-up, which are critically needed as an alternative to natural enzymes. These nanozymes exhibit natural enzyme-like activity and have been applied to various kinds of detection and treatment methods for biomolecules such as DNA, proteins, cells, and small molecules including glucose. To highlight progress in the field of nanozymes, this review discusses recent nanozyme-based research results and their applications for the development of novel biosensor, immunoassay, cancer diagnostics, therapeutics, and environmental engineering technologies. Current challenges and future prospects of nanozymes for widespread use in biotechnology are also discussed.

1. Introduction

Early diagnosis of diseases is an area of growing importance for the medical community. The early detection of diseases helps improve therapeutic decision-making, which decreases the severity of illness and length of hospital stay. Accordingly, a number of biosensing techniques have been developed for rapid, reliable, and sensitive detection of biomolecules that can be used as indicators of disease. Among various biosensing methods for diagnosing human diseases, natural enzymes such as horseradish peroxidases have been frequently used for bioassay, as they can catalyze various colorimetric reactions in the presence of specially designed substrates, and they display good sensitivity and selectivity towards the target molecules [1]. In spite of their novel catalytic efficiency, natural enzymes have critical limitations for industrial application, such as low stability in harsh conditions (temperature and pH) and relatively high costs for preparation, purification, and storage. Therefore, over the past few decades, researchers have made an intense effort to develop artificial enzymes for a wide range of applications. For example, chemical complexes based on cyclodextrin [2], porphyrin [3, 4], hemin [5, 6], hematin [7], and specially designed biomolecules in the form of nucleic acids and

proteins have been successfully used to mimic the catalytic activity of natural enzymes [8].

In this regard, Fe₃O₄ magnetic nanoparticles (MNPs) have been found to exhibit intrinsic peroxidase activity [9]. This remarkable discovery opens up the way for a new class of enzyme mimetics. To date, various nanostructured materials have been reported to possess intrinsic enzymatic activity, including Fe₃O₄ magnetic nanoparticles (MNPs) [9], platinum nanoparticles (Pt NPs) [10–12], cerium oxide nanoparticles (CeO₂ NPs) [13], gold nanoparticles (Au NPs) [14–16], copper oxide nanoparticles (CuO NPs) [17], BiFeO₃ nanoparticles [18], CoFe₂O₄ nanoparticles [19–21], FeS and FeSe nanoparticles [22], graphene oxide [23], single-wall carbon nanotubes [24], and hemin-graphene hybrid nanosheets [25]. Herein, we name these nanomaterials which have enzyme-like catalytic activity “nanozymes.” In contrast to natural enzymes, nanozymes are inherently robust, stable in harsh conditions (pH and temperature), and easy to mass-produce with simple scale-up. These advantages make them promising candidates for analytical and environmental applications [26].

In this paper, we present a comprehensive review of recent research on nanozymes and their applications categorized by representative fields of application, such as biosensor,

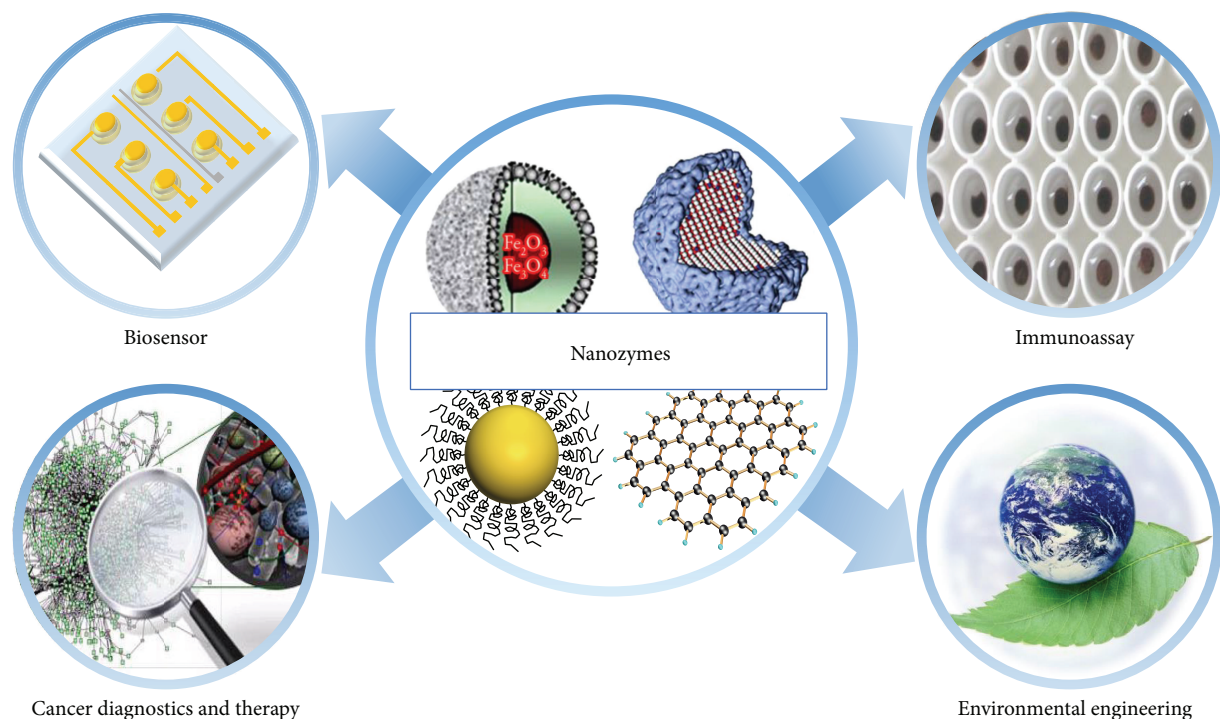


FIGURE 1: A wide range of applications in the field of nanozymes. The images of nanomaterials in the center ring represent (clockwise from top left) Fe_3O_4 nanoparticle, CeO_2 nanoparticle, graphene oxide, and Au nanoparticle, which are the typical nanomaterials exhibiting enzyme-like activities.

immunoassay, cancer diagnostics, therapeutics, and environmental engineering. We also provide challenges and research trends in the emerging nanozyme research field (Figure 1).

2. Fundamentals of Nanozymes

Due to the absence of an active site in nanozymes, where only a specific substrate molecule binds and undergoes a chemical reaction, researchers have developed various strategies to endow nanozymes with specificity to target molecules. The most representative strategies can be divided between the oxidase-coupled method and the surface-modification method. In the oxidase-coupled method, nanozymes with peroxidase-like activity gain their specificity by being coupled with oxidase, which generates H_2O_2 as a product of a catalytic reaction which occurs only in the presence of the target molecule. Peroxidase-like nanozymes subsequently catalyze the oxidation of colorimetric substrates with the resulting H_2O_2 . For the surface-modification method, an antibody is generally conjugated on the surface of the nanozyme to provide specificity toward antigen molecules, mostly in the colorimetric immunoassay system. By conjugation of the antibody specific to the target antigen on the surface of the nanozyme, the nanozyme can act as a target-specific probe, generating a colorimetric signal in the presence of the colorimetric substrate and H_2O_2 . In the same manner, ligand-conjugated nanozymes can specifically bind to target receptors and produce a colorimetric signal when the targeted molecules bind on the nanozymes' surface. Aptamers are attracting interest in the fields of therapeutics and diagnostics

and are becoming promising candidates for use in giving specificity to nanozyme-based biosensors.

The intrinsic enzyme-like activities of nanozymes are generally believed to be produced by atoms present on the surface as well as in the nanozyme's inside core. Thus, the atomic composition of nanozymes is the most important factor in determining their catalytic activity, although other factors such as size, morphology, surface coating and modification, pH, and temperature can also have an impact [8]. Based on the type of composition, nanozymes can be distributed into three categories: metal oxide-based, metal-based, and carbon-based nanozymes.

2.1. Metal Oxide-Based Nanozymes. Metal oxide nanoparticles have been widely used in the field of biomedical applications such as biosensor, targeted drug delivery, tissue repair, immunoassay, and contrast agents in magnetic resonance imaging (MRI) and cell separation [27]. Since metal oxide nanoparticles are commonly considered chemically and biologically inert, additional surface engineering and subsequent conjugation with functional substances are required to endow metal oxide nanoparticles with functionality. Recently, inspired by the notable discovery of the intrinsic catalytic activity of MNP as a peroxidase [9], metal oxide-type nanozymes have attracted great interest, with a large number of papers discussing newly reported enzyme-like activities of these nanomaterials. A variety of metal oxide-based nanozymes have been discovered to possess enzyme-like catalytic activities (peroxidase, catalase, and superoxide dismutase (SOD)), including MNPs [9], CeO_2 NPs [13],

cobalt oxide nanoparticles (Co_3O_4 NPs) [28], manganese dioxide nanoparticles (MnO_2 NPs) [29], vanadium pentoxide nanoparticles (V_2O_5 NPs) [30], and CuO NPs [31]. Generally, metal oxide-based nanozymes with peroxidase-like activity have been those most widely investigated by researchers, owing to their convenience for constructing amperometric and colorimetric detection systems by utilizing the capability of peroxidase to catalyze certain substrates which generate the corresponding electric and colorimetric signal in the presence of hydrogen peroxide (H_2O_2). Herein, we focus on colorimetric detection systems utilizing peroxidase-like nanozymes and associated applications.

2.2. Metal-Based Nanozymes. Metal-based nanozymes, such as Au NPs and Pt NPs, have been discovered to possess the catalytic activities of oxidase, peroxidase, catalase, and SOD. In addition to the single nanoparticle system mentioned above, nanocomposites which combine a metal-based nanozyme with other nanozymes have been also intensively developed, including Fe_3O_4 -graphene oxide (GO) [32], Fe_3O_4 -Pt [33], Au-Pt [34], and GO- Fe_3O_4 -Pt [35] nanocomposites. Surprisingly, it was reported that metal-based nanozymes often exhibit synergistic effects which significantly enhance catalytic performance when coupled with other nanozymes as a composite [33].

2.3. Carbon-Based Nanozymes. Carbon-based nanozymes, such as fullerene, carbon nanotube, graphene oxide, and carbon dot, are also attracting great interest owing to their unique enzyme-mimicking activities [23–25, 36–43]. They have been found to possess peroxidase and SOD-mimicking abilities and are widely utilized as signaling agents for signal amplification and detection of analytes in the field of biosensors and immunoassays.

3. Recent Applications

3.1. Biosensors. In recent time, horseradish peroxidase (HRP), which can catalyze the oxidation of a variety of substrates by H_2O_2 , has been one of the most commonly used enzymes for the construction of biosensors. In spite of its high catalytic efficiency, HRP-based biosensors have critical problems, in that the catalytic activity of HRP is prone to degradation in long-term storage and harsh conditions, thereby leading to errors in the process of sensing. To solve this problem, a peroxidase-like nanozyme which is highly robust against environmental conditions is utilized in place of HRP, providing a cost-effective method of fabrication of biosensors.

3.1.1. H_2O_2 Detection. H_2O_2 detection plays an essential role in the fields of biology, medicine, environmental engineering, and food industry. Since H_2O_2 , a product of an incompletely reduced metabolite of oxygen, is generated as a by-product of various biological pathways and is a contaminant in several industrial products and wastes, H_2O_2 detection is of practical importance in the field of biosensors. With substantial progress in biosensing technology, various methods for H_2O_2 detection have been reported. Among them is the

colorimetric signal readout strategy, based on a redox reaction between HRP and colorimetric substrates such as 2,2'-azino-bis(3-ethylbenzothiazoline-6-sulphonic acid) (ABTS) and 3,3',5,5'-tetramethylbenzidine (TMB). This strategy has been actively developed due to its high sensitivity, selectivity, and simplicity for detecting H_2O_2 . However, since the colorimetric detection method using HRP has problems of low stability and high cost, nanozymes showing peroxidase-like activity have been intensively utilized to resolve these drawbacks. Beginning with the remarkable discovery that MNPs exhibit intrinsic peroxidase-like activity [9], many researchers have focused on the development of novel H_2O_2 detection methods employing various nanozymes. Here, we discuss recent applications of various nanozymes in H_2O_2 detection.

After Yan's report, H_2O_2 detection methods with MNPs (used as peroxidase-like nanozymes) were further developed by Wei and Wang [44]. This research outlined a colorimetric detection method for H_2O_2 , in which MNPs were used to catalyze the oxidation of ABTS in the presence of H_2O_2 . The catalytic oxidation of ABTS with H_2O_2 generates green-colored products, by which H_2O_2 can be detected by the naked eye. They noted that ABTS could be oxidized by H_2O_2 in the absence of any catalysts but demonstrated that the presence of MNPs gave a 320% higher response of absorption spectra when compared with the absence of MNPs. Not only the peroxidase-like catalytic activity of Fe_3O_4 MNPs but also their high stability in rough conditions (pH and temperature) was confirmed with additional investigations.

Based on the colorimetric detection method above, many approaches have proceeded by varying the colorimetric substrates and nanozymes used. *N,N*-Dimethyl-*p*-phenylenediamine sulfate (DPD) was used as a colorimetric substrate in place of ABTS [45]. The DPD-MNPs analytical system showed several advantages (lower operating temperature and detection limit and higher sensitivity) over the system using ABTS, because DPD is more easily oxidized by H_2O_2 than ABTS and because oxidized DPD (DPD^+) produces a colored product with a strong absorption maximum at 550 nm. Aside from the signal-on colorimetric method above, Jiang's group has developed a new type of fluorescence method using rhodamine B (RhB) as a substrate [46]. In this method, MNPs catalyze H_2O_2 to form the radical OH, which can oxidize RhB to form colorless and nonfluorescent products. In short, the more the H_2O_2 exists, the weaker the fluorescence intensity of RhB is.

Other nanozymes have been also reported to detect H_2O_2 . Au NPs have been discovered to possess intrinsic peroxidase-like activity [47]. Cao's studies reported that positively charged Au NPs can catalyze the oxidation of TMB by H_2O_2 . Carboxyl-modified graphene oxide was shown to possess intrinsic peroxidase-like activity that can catalyze the reaction of TMB in the presence of H_2O_2 to produce a blue-color reaction [23]. Concentrations as low as $5 \times 10^{-8} \text{ mol L}^{-1}$ H_2O_2 were detected with a linear range from 5×10^{-8} to $1 \times 10^{-6} \text{ mol L}^{-1}$.

3.1.2. Glucose Detection. Peroxidase-like nanozymes coupled with glucose oxidase (GOx) have been frequently employed

in the construction of glucose biosensors. Wang et al. developed a colorimetric glucose detection platform by combining the catalytic oxidation of glucose with GOx and the catalytic reaction of ABTS with MNPs [48]. Glucose concentrations as low as 30 μM were detected with a linear range from 50 μM to 1 mM in this study.

There have been several reports of an electrochemical biosensing platform using GOx-coupled nanozymes. A highly efficient and robust electrochemical biosensing strategy employing a nanocomposite harboring GOx-coupled nanozymes was developed by our group [49]. In this report, MNPs and GOx were entrapped in the pores of mesoporous carbon, in which GOx immobilized in the nanocomposite generates H_2O_2 which then is directly reduced to H_2O , with the electrocatalytic reduction mediated by MNPs. This system showed a linear range of $(0.5 \text{ to } 10) \times 10^{-3} \text{ M}$ and a detection limit of $0.2 \times 10^{-3} \text{ M}$.

3.1.3. Oxidase-Coupled Methods (Except Glucose Oxidase).

On the basis of the mechanism of glucose detection above, several different oxidases have also been coupled with nanozymes for the fabrication of biosensing platforms. A nanostructured multicatalyst system consisting of MNPs and cholesterol oxidase entrapped in large-pore-sized mesoporous silica has been developed for convenient colorimetric detection of cholesterol [50]. This multicatalyst system is composed of MNPs incorporated in the wall of mesocellular silica pores, forming magnetic mesoporous silica (MMS), and cholesterol oxidases. In this system, cholesterol oxidase immobilized in the MMS promotes a reaction with cholesterol to generate H_2O_2 , which subsequently activates MNPs in the mesocellular silica pores to convert a colorimetric substrate into a colored product. The result of this investigation shows the cholesterol oxidase-coupled method to have high selectivity and sensitivity (limit of detection, LOD, of 5 μM in the linear range from 10 to 250 μM) for the detection of cholesterol. A colorimetric method for detection of galactose, which utilizes a nanostructured multicatalyst system consisting of MNPs and galactose oxidase, has also been reported [51]. The clinical applicability of this multicatalytic system was successfully evaluated as a promising analytical tool to diagnose galactosemia, by determining the concentration of galactose eluted from the dried blood specimens provided by clinical hospitals.

Apart from the above oxidases, alcohol oxidase has been used in a colorimetric biosensor for quantification of ethanol and methanol [52]. The nanocomposite system utilizing alcohol oxidase entrapped in mesocellular silica with MNPs provided a rapid and convenient platform for analysis of alcohol, with high stability and reusability. It showed a linear concentration range from 100 to 500 μM with a detection limit as low as 25 μM .

3.1.4. Other Methods. Recently, peroxidase-mimicking nanomaterials such as MNPs, CeO_2 NPs, and Au NPs [15] have been employed for new methods of DNA detection. A label-free colorimetric detection method for nucleic acids has been developed [53]. In this method, the target DNA in the sample, which is amplified by polymerase chain reaction

(PCR), is directly adsorbed on the surface of the MNPs due to electrostatic interactions between the negatively charged phosphate backbone and the positively charged surface of the NPs, thereby inducing a shielding effect against colorimetric substrate binding to MNPs. The peroxidase activity of MNPs will decrease due to the DNA-induced shielding, so that the intensity of the color signal will also be significantly reduced. Using this detection method, researchers successively detected *Chlamydia trachomatis* in human urine, which is one of the common bacteria causing sexually transmitted disease (STD) [54, 55]. CeO_2 NPs were also employed in a label-free colorimetric method for detecting *C. trachomatis*, and this method provided ultrafast detection of the target nucleic acid (target nucleic acids can be determined within a few minutes) [56].

A novel biosensing format using aptamers has been developed by several researchers based on the fact that aptamers, which are ssDNA or ssRNA that can specifically bind to a target, can replace antibodies for the specific recognition of target molecules. A method using chitosan-modified MNPs conjugated with thrombin aptamers was reported by Zhang's group [57]. They constructed a sandwich-type assay for the detection of thrombin with two thrombin aptamers. This aptamer-based assay showed a linear detection range from 1 to 100 nM and a detection limit of 1 nM of thrombin.

3.2. Immunoassays. Immunoassays have been used in hospitals, laboratory, medicine, and research to improve the health and well-being of humans and animals. Information gained by clinical immunoassay testing has shortened the length of hospital stays and decreased the severity of illness by identifying and assessing the progression of disease, thereby leading to improved therapeutic choices. In life science research, immunoassays are used in the study of biological systems for tracking different proteins, hormones, and antibodies. In industry, immunoassays are used to detect contaminants in food and water and in quality control to monitor specific molecules used during product processing. However, the most commonly used enzymes in immunoassay include horseradish peroxidase and alkaline phosphatase [58–62], which lose their enzymatic activities gradually over long-term storage [63]. To overcome these limits, various studies on replacing natural enzymes have been reported, and consequently novel types of immunoassay using nanozymes in place of HRP have been developed.

3.2.1. Sandwich or Antigen-Down Type Immunoassays. Gao and coworkers reported an immunoassay using chitosan-modified MNPs (CS-MNPs) as a replacement for HRP in the traditional immunoassay [63]. They provided protocols for antigen-down and sandwich immunoassays with CS-MNPs and detected mouse IgG and carcinoembryonic antigen (CEA), respectively. Chitosan modified on the surface of MNPs prevented aggregation of MNPs, so that MNPs were easily dispersed in aqueous solutions. Meanwhile, amino groups in the chitosan provided a convenient site for covalent linking of antibodies to MNPs, thereby replacing the linkage of HRP-conjugated antibodies to CS-MNP-conjugated antibodies in the immunoassay. Capture-detection immunoassay

was also developed to detect CEA by employing the magnetic properties of CS-MNPs, which facilitate capturing, separating, and enriching antigens as well as redispersing the MNP aggregation in solution.

Zhang and coworkers reported a novel immunoassay utilizing Prussian blue modified γ -Fe₂O₃ NPs [64]. Prussian blue, a dark blue pigment with the idealized formula Fe₇(CN)₁₈, was modified on the surface of γ -Fe₂O₃ NPs due to its excellent electrochemical behavior that accelerated electron transfer and its catalytic properties that could catalyze the reduction of H₂O₂. Prussian blue modified γ -Fe₂O₃ NPs (PBMNPs) were next conjugated with staphylococcal protein A (SPA) to bind to IgG immobilized in the well, so that PBMNPs could derive a colorimetric reaction in the presence of TMB and H₂O₂.

Ferritins, nanoscale globular protein cages encapsulating a ferric core, were used in immunoassay in Tang et al.'s study [65]. In this study, ferritin showed a thermally stable and pH-tolerable enzyme-mimetic activity derived from the ferric nanocore of ferritin. Two forms of immunoassay systems were constructed: antigen-down type and sandwich type. Avidin was selected as the target molecule of the antigen-down immunoassay and nitrated human ceruloplasmin as the target molecule of the sandwich-type immunoassay. They also reported that the ferritins could be utilized in analytical applications such as H₂O₂ assay. In their assay, ferritin oxidizes the p-HPPA in the presence of H₂O₂ to generate a fluorescent product. This ferritin-based H₂O₂ assay shows a detection limit of 0.16 μ M and a linear detection range of 40 μ M, which is one-order higher sensitivity with a broader linear response range.

Immunoassay systems for detection of rotavirus and breast cancer have been developed [66], in which MNPs are conjugated to antibodies against rotaviruses and human epidermal growth factor receptor 2 (HER2). In this system, sandwich-type and antigen-down type immunoassay were used to detect rotavirus and HER2, respectively. For the detection of rotavirus, rotavirus antibodies were first immobilized in a well and rotavirus bound to the immobilized antibody. Subsequently, MNP-conjugated antibodies (MNP-Abs) were added to the well in order to bind to captured rotaviruses. Finally, the peroxidase substrate TMB was changed into blue-colored products in the presence of H₂O₂. An antigen-down immunoassay system was used in the case of breast cell detection, which did not require prior immobilization of antibodies in the bare well surface. Breast cells were cultured in a well so that they adsorbed to the surface of the well. MNPs-Abs were then applied to the cell-cultured well, followed by adding TMB and H₂O₂ to induce a colorimetric reaction. This assay system displayed excellent specificity, sensitivity, and linearity for quantitative detection of the target molecules, as well as the production of a color signal that could be detected by the naked eye.

Based on the above system, a nanocomposite-based immunoassay was also performed, in which nanocomposite entrapping MNPs and Pt NPs in ordered mesoporous carbon (OMC) were utilized instead of HRP [33]. This immunoassay generated significantly higher absorption intensity of color signal than the current ELISA and was able to quantify the

target antigen very rapidly within three minutes, while the conventional ELISA requires several tens of minutes for color signal development [67, 68]. It showed a limit of detection (LOD) for HER2 of 1.5 ng mL⁻¹ in the linear range from 2.5 to 100 ng mL⁻¹. The nanocomposite was found to have 50 times higher catalytic efficiency than that of free MNPs, owing to the high catalytic action of Pt NPs.

Graphene oxide (GO) has been used in immunoassay as a peroxidase-mimicking nanozyme [41]. Yan's group developed a sandwich-type immunoassay for the detection of cancer biomarker prostate specific antigen (PSA). In this work, a magnetic bead (MB) was used to immobilize the primary PSA antibody (Ab₁) and then a GO-conjugated secondary antibody (Ab₂) was applied in the presence of PSA. Subsequently, MB-Ab₁ was separated from the immunocomplex by an external magnetic field, and GO catalyzed the oxidation of hydroquinone in the presence of H₂O₂ to generate a brown-colored product.

Conjugating both MNPs and Pt NPs on the surface of GO enabled highly sensitive and rapid colorimetric detection of the target cancer cell [35]. In this work, it was notable that the electron transfer between MNPs and Pt NPs creates a synergistic effect, significantly enhancing the catalytic performance of MNPs-Pt NPs-GO nanohybrids. Using this immunoassay system, human breast adenocarcinoma cells (SKBR-3), which overexpressed HER2, were detected in five minutes with high specificity and sensitivity. The LOD for target SKBR-3 cells was found to be about 100 cells in the linear range from 100 to 1000 cells. Moreover, fluorescence imaging of SKBR-3 was successfully performed with MNPs-Pt NPs-GO nanohybrids.

3.2.2. Other Immunoassays. By employing the superparamagnetic property of MNPs, a capture-detection immunoassay system has been developed by Gao's group [63]. In the procedure, the CS-MNPs were conjugated with carcinoembryonic antibodies (anti-CEA M111147) and then mixed with the sample containing CEA. After the CEA was captured by MNPs, a magnetic field was applied to separate the MNPs which had captured CEA. Finally, the MNPs capturing CEA were injected into microplate wells coated with another monoclonal CEA antibody, creating the sandwich format. Thereby, the MNPs prompted the generation of a color signal upon addition of colorimetric substrate and H₂O₂ to the wells. Cardiac troponin I (TnI) in serum, a well-known biomarker for myocardial infarction, was also detected by a capture-detection immunoassay utilizing the magnetism and peroxidase ability of MNPs [9].

3.3. Cancer Diagnostics without Immune Reaction. Aside from immunoassay using antigen-antibody interaction, other novel assays using nanozymes have been developed particularly for the diagnosis of tumor cells. Asati and coworkers reported an assay for the determination of tumor cells with poly(acrylic acid)-coated CeO₂ NPs (nanoceria) as an oxidase mimic [13]. When the nanoparticles were conjugated with folic acid, they bound to folate receptors on the tumor cell (A-549 lung cancer cells), due to high expression of folate receptors on the tumor cell surface. Polymer-coated

nanoceria as an oxidase mimic made detection of tumor cells easier than with traditional immunoassay, because it directly oxidized a colorimetric substrate to a colored product without H_2O_2 and additional steps to introduce an enzyme-conjugated secondary antibody. Further advances in this technology were also reported by employing a fluorescence-generating substrate, ampliflu, to detect target cancer cells at around neutral pH [69].

Another interesting study to visualize target tumor tissues without the use of any additional targeting ligands has also been described [70]. In this study, peroxidase-like iron oxide nanoparticles were encapsulated inside a recombinant human heavy-chain ferritin (Hfn) protein shell, which binds to tumor cells that overexpress transferrin receptor 1. The iron oxide cores catalyzed the oxidation of peroxidase substrates in the presence of H_2O_2 to produce the colorimetric signal that was used to visualize tumor tissues. Through this strategy, nine types of cancer were successfully verified with enough specificity and sensitivity.

3.4. Therapeutic Applications. As described above, nanozymes have been widely used for detection and diagnostic methods. Besides these applications, many researchers have also studied therapeutic applications including anti-inflammatory effects, neuroprotection, stem cell growth, and antiaging. In general, SOD was often utilized for therapeutic applications owing to its protective role as a scavenger of reactive oxygen intermediates (ROIs). Intracellular concentration of ROI, including hydrogen peroxidase, hypochlorite ions, hydroxyl radicals, hydroxyl ions, and superoxide anions, has been known to be a cause of cell degeneration and associated diseases [71]. Inspired by earlier studies by Seal et al. which revealed the activity of CeO_2 NPs as a SOD-mimic [72, 73], various studies have been attempted to develop SOD-mimicking nanozymes.

Chen et al. reported that nanoceria as a SOD-mimic prevented retinal degeneration by inhibiting the production of ROIs [74]. In their work, nanoceria prevented ROI-induced apoptosis and intracellular accumulation of ROI in cultured retinal neurons in the presence of H_2O_2 . They further demonstrated that nanoceria injected into the eyes of rats protected retina photoreceptor cells from light-induced degeneration. The study by Hirst et al. also demonstrated that nanoceria could be used for anti-inflammation by elimination of the radical oxygen species in J774A.1 murine macrophage cells [75].

Superparamagnetic iron oxide (SPIO) nanoparticles have been employed to promote growth of stem cells. Huang et al. reported that Ferucarbotran, a commercialized SPIO, could promote cell growth in human mesenchymal stem cells (hMSCs) by diminishing intracellular H_2O_2 and also accelerate cell cycle progression [76]. In this report, the intrinsic peroxidase-like activity of SPIO dramatically reduced intracellular H_2O_2 after internalization into hMSCs, as well as free iron ions released from lysosomal degradation of SPIO-affected cell cycle control molecules.

3.5. Environmental Engineering. Recently, environmental problems such as water and air pollution, food safety, and

public health have become growing concerns in society. In addition to the aforementioned applications, nanozyme-based techniques have been explored for use in the field of environmental technology.

3.5.1. Pollutant Detection. Ding et al. developed a simple and rapid colorimetric method for detecting melamine, an organic nitrogenous compound which is toxic when swallowed and has been illegally added to dairy products [77]. The principle of this method is as follows. Melamine inhibits the catalytic oxidation of colorimetric substrates (ABTS) by MNPs in the presence of H_2O_2 , because it competitively reacts with H_2O_2 , forming an additional compound. Consequently, the intensity of the ABTS color signal was dependent on the concentration of melamine. On the basis of this reaction, a colorimetric system using MNPs could enable easy detection by the naked eye of concentrations of melamine above safety limits in dairy products.

Nanocomposite-entrapping MNPs and oxidase in mesoporous carbon were used to detect several phenol compounds amperometrically, such as phenol, cresol, and cathechol [49]. These phenol compounds produced a concentration-dependent increase of cathodic current in this system, which may have great potential in the field of environmental monitoring.

3.5.2. Pollutant Removal. Although there have been many methods for removal of industrial dyestuffs, such as absorption, precipitation, and ultrasonic decomposition, they could not efficiently degrade organic pollutants in wastewater. Nanozyme-based methods have been found to be a powerful, cost-effective, and simple method for degradation and mineralization of organic dyes from industrial processes. Most prominently, MNPs such as peroxidase have been investigated for degradation of organic pollutants, such as methylene blue, phenol, and rhodamine B. A MNP-based degradation method offers distinct advantages over existing degradation methods which use HRP, such as lower cost, high stability, and reusability. MNPs- H_2O_2 could remove 85% of phenol from aqueous solution within three hours [78]. The MNPs-based degradation showed higher efficiency compared to HRP-based degradation and stability in a broad range of temperatures (5–90°C), leading to ease of storage. Furthermore, MNPs could be captured by the application of an external field and recycled for five rounds, retaining almost 100% of their activity. Removal of methylene blue by MNPs- H_2O_2 coupled method has also been successfully performed by Jiang et al. [79]. It was observed that 96% of methylene blue was degraded in 15 minutes at optimized condition.

Gao et al. reported that MNPs- H_2O_2 system could degrade biofilm and kill resident bacteria [80]. Biofilm, especially formed by *Pseudomonas aeruginosa*, occurs in hospital water systems and medical devices with high frequency, becoming a common cause of nosocomial infection [81]. In this report, MNPs- H_2O_2 system exhibited significantly higher efficiency than the use of H_2O_2 in degradation of biofilm. The authors confirmed that additional free hydroxyl radicals generated by MNP catalysis of H_2O_2 facilitated the oxidative cleavage of biofilm components (nucleic acids,

TABLE 1: Various application studies based on nanozymes.

Application field	Nanozymes	Activity	Detection method	Details	Ref.	
Biosensor	MNPs	Peroxidase	Colorimetric	H ₂ O ₂ biosensor	[9]	
	Au NPs	Glucose oxidase	Colorimetric	Nucleic acid detection	[15]	
	Carboxyl-modified graphene oxide	MNPs	Peroxidase	Colorimetric	H ₂ O ₂ and glucose biosensor	[23]
		MNPs	Peroxidase	Colorimetric	H ₂ O ₂ and glucose biosensor	[44]
	MNPs	Peroxidase	Colorimetric	H ₂ O ₂ biosensor	[45]	
	MNPs	Peroxidase	Colorimetric	H ₂ O ₂ biosensor	[46]	
	Au NPs	Peroxidase	Colorimetric	H ₂ O ₂ and glucose biosensor	[47]	
	MNPs	Peroxidase	Electrochemical	Glucose biosensor	[48]	
	MNPs (with oxidase in mesoporous carbon)	Peroxidase	Electrochemical	Glucose biosensor	[49]	
	MNPs (with oxidase in mesoporous silica)	Peroxidase	Colorimetric	Glucose and cholesterol biosensor	[50]	
MNPs (with oxidase in mesoporous silica)	Peroxidase	Colorimetric	Galactose biosensor	[51]		
Immunoassay	MNPs (with oxidase in mesoporous silica)	Peroxidase	Colorimetric	Alcohol biosensor	[52]	
	MNPs	Peroxidase	Colorimetric	Nucleic acid detection (<i>Chlamydia trachomatis</i>)	[53]	
	CeO ₂ NPs	Oxidase	Colorimetric	Nucleic acid detection (<i>Chlamydia trachomatis</i>)	[56]	
	Chitosan-modified MNPs with thrombin aptamers	Peroxidase	Colorimetric	Thrombin detection	[57]	
	MNPs	Peroxidase	Colorimetric	Cardiac troponin I (TnI) detection	[9]	
	MNPs-Pt NPs in mesoporous carbon	Peroxidase	Colorimetric	Rotavirus and HER2 detection	[33]	
	Graphene oxide	Peroxidase	Colorimetric	Prostate specific antigen (PSA) detection	[41]	
	Chitosan-modified MNPs	Peroxidase	Colorimetric	Mouse IgG and carcinoembryonic antigen detection	[63]	
	Prussian blue modified γ -Fe ₂ O ₃ NPs	Peroxidase	Colorimetric	IgG detection	[64]	
	Ferritins	Peroxidase	Fluorometric	Avidin and human ceruloplasmin detection	[65]	
Cancer diagnostics (without immune reaction) and therapy	MNPs	Peroxidase	Colorimetric	Rotavirus and HER2 detection	[66]	
	MNPs-Pt NPs on graphene oxide	Peroxidase	Colorimetric, fluorometric	HER2 detection and imaging	[35]	
	Poly(acrylic acid)-coated CeO ₂ NPs	Oxidase	Colorimetric	Lung cancer cell detection	[13]	
	Poly(acrylic acid)-coated CeO ₂ NPs	Oxidase	Colorimetric	Lung and breast cancer cell detection	[69]	
	Magnetoferritin NPs	Peroxidase	Colorimetric, fluorometric	Cancer cell imaging	[70]	
	CeO ₂ NPs	Superoxide dismutase		Prevention of retinal degeneration	[74]	
	CeO ₂ NPs	Superoxide dismutase		Anti-inflammation	[75]	
	Superparamagnetic iron oxide NPs	Peroxidase		Promotion of stem cell growth	[76]	
	MNPs (with oxidase in mesoporous carbon)	Peroxidase	Electrochemical	Phenol, cresol, and catechol detection	[49]	
	MNPs	Peroxidase	Colorimetric	Melamine detection	[77]	
Environmental engineering	MNPs	Peroxidase		Removal of phenol	[78]	
	MNPs	Peroxidase		Removal of methylene blue	[79]	
	MNPs	Peroxidase		Biofilm degradation	[80]	
	MNPs	Peroxidase				

proteins, and polysaccharides) as well as killing resident bacteria.

4. Conclusions and Future Research Aspects

Nanozymes have recently emerged as a potent alternative to natural enzymes. As discussed above, although they are still in the initial stages of research, their use has developed substantially in many different detection and treatment methods for biomolecules (Table 1). Despite the advantages of nanozymes such as their low cost, high stability, robustness, ease of mass production, and long-term storability, there are several challenges to be tackled for practical use. Firstly, most nanozymes have low activity compared to natural enzymes. Even if the nanomaterial itself is highly active, additional coating and surface modification can decrease its performance. Therefore, development of novel nanozymes exhibiting high activity and appropriate surface-modification techniques are the emerging issues in the field of nanozymes. Nanozymes also have low selectivity to targets, owing to the absence of active sites where a substrate molecule binds and undergoes a chemical reaction in a natural enzyme. Although researchers have designed various types of surface-modified nanozymes with polymers, nucleic acids, and antibodies to provide selectivity mimicking natural enzymes, this is still insufficient for use in practical applications. Toxicity of nanozymes to humans and the ecosystem is also an essential issue to be solved in regard to environmental and therapeutic applications.

In order for nanozymes to be positioned as a novel source technology by efficiently overcoming the limitations of natural enzymes, we offer the following suggestions. The development of new nanozymes with higher activity and other positive properties than existing nanozymes is required. While traditional research on developing nanozymes has been performed by random screening of the enzyme-like activities of existing unspecified nanomaterials, future research will follow a strategy of rational screening of enzyme-like activity based on those atomic compositions which are envisaged to catalyze enzymatic reactions. Furthermore, a strategy to prepare composites can be expected to resolve the current major limitations of nanozymes of low catalytic activity, by exploiting their synergistic effect to facilitate electron transfer between composite materials during redox reaction. Bioinspired synthesis of nanozymes also provides an option to prepare nontoxic nanozymes, by effectively circumventing the use of toxic chemicals in conventional chemical synthesis, thereby accelerating their use in therapeutic applications. Finally, the development of novel surface engineering technology that can make nanozymes selective to target substrates will be important in this field. With the abovementioned research projects, we expect nanozymes to be widely employed in a wide range of applications in the near future.

Conflict of Interests

The authors declare no financial or commercial conflict of interests.

Acknowledgments

This work was supported by the Basic Science Research Program through the National Research Foundation of Korea (NRF) funded by the Ministry of Science, ICT & Future Planning (NRF-2014R1A1A1006016) and by the Gachon University research fund of 2014 (GCU-2014-0110).

References

- [1] D. L. Nelson and M. M. Cox, *Lehninger Principles of Biochemistry*, vol. 6, chapter 6, W. H. Freeman, New York, NY, USA, 2005.
- [2] Z. Liu, R. Cai, L. Mao, H. Huang, and W. Ma, "Highly sensitive spectrofluorimetric determination of hydrogen peroxide with β -cyclodextrin-hemin as catalyst," *Analyst*, vol. 124, no. 2, pp. 173–176, 1999.
- [3] R. P. Bonar-Law and J. K. M. Sanders, "Polyol recognition by a steroid-capped porphyrin. Enhancement and modulation of misfit guest binding by added water or methanol," *Journal of the American Chemical Society*, vol. 117, no. 1, pp. 259–271, 1995.
- [4] X.-M. Huang, M. Zhu, L.-Y. Mao, and H.-X. Shen, "Catalytic determination of hydrogen peroxide by using the molybdenum-porphyrin complex as a mimetic enzyme of peroxidase," *Analytical Sciences*, vol. 13, no. 1, pp. 145–147, 1997.
- [5] L. Fruk and C. M. Niemeyer, "Covalent hemin-DNA adducts for generating a novel class of artificial heme enzymes," *Angewandte Chemie—International Edition*, vol. 44, no. 17, pp. 2603–2606, 2005.
- [6] Q. Wang, Z. Yang, X. Zhang, X. Xiao, C. K. Chang, and B. Xu, "A supramolecular-hydrogel-encapsulated hemin as an artificial enzyme to mimic peroxidase," *Angewandte Chemie International Edition*, vol. 46, no. 23, pp. 4285–4289, 2007.
- [7] Z. Genfa and P. K. Dasgupta, "Hematin as a peroxidase substitute in hydrogen peroxide determinations," *Analytical Chemistry*, vol. 64, no. 5, pp. 517–522, 1992.
- [8] H. Wei and E. Wang, "Nanomaterials with enzyme-like characteristics (nanozymes): next-generation artificial enzymes," *Chemical Society Reviews*, vol. 42, no. 14, pp. 6060–6093, 2013.
- [9] L. Gao, J. Zhuang, L. Nie et al., "Intrinsic peroxidase-like activity of ferromagnetic nanoparticles," *Nature Nanotechnology*, vol. 2, no. 9, pp. 577–583, 2007.
- [10] R. Polsky, R. Gill, L. Kaganovsky, and I. Willner, "Nucleic acid-functionalized Pt nanoparticles: catalytic labels for the amplified electrochemical detection of biomolecules," *Analytical Chemistry*, vol. 78, no. 7, pp. 2268–2271, 2006.
- [11] T. Li, Y. Du, and E. Wang, "Polyethyleneimine-functionalized platinum nanoparticles with high electrochemiluminescence activity and their applications to amplified analysis of biomolecules," *Chemistry—An Asian Journal*, vol. 3, no. 11, pp. 1942–1948, 2008.
- [12] W. W. He, Y. Liu, J. S. Yuan et al., "Au@Pt nanostructures as oxidase and peroxidase mimetics for use in immunoassays," *Biomaterials*, vol. 32, no. 4, pp. 1139–1147, 2011.
- [13] A. Asati, S. Santra, C. Kaitanis, S. Nath, and J. M. Perez, "Oxidase-like activity of polymer-coated cerium oxide nanoparticles," *Angewandte Chemie—International Edition*, vol. 48, no. 13, pp. 2308–2312, 2009.
- [14] W. J. Luo, C. F. Zhu, S. Su et al., "Self-catalyzed, self-limiting growth of glucose oxidase-mimicking gold nanoparticles," *ACS Nano*, vol. 4, no. 12, pp. 7451–7458, 2010.

- [15] X. Zheng, Q. Liu, C. Jing et al., "Catalytic gold nanoparticles for nanoplasmonic detection of DNA hybridization," *Angewandte Chemie International Edition*, vol. 50, no. 50, pp. 11994–11998, 2011.
- [16] Y. J. Long, Y. F. Li, Y. Liu, J. J. Zheng, J. Tang, and C. J. Huang, "Visual observation of the mercury-stimulated peroxidase mimetic activity of gold nanoparticles," *Chemical Communications*, vol. 47, no. 43, pp. 11939–11941, 2011.
- [17] W. Chen, J. Chen, Y.-B. Feng et al., "Peroxidase-like activity of water-soluble cupric oxide nanoparticles and its analytical application for detection of hydrogen peroxide and glucose," *Analyst*, vol. 137, no. 7, pp. 1706–1712, 2012.
- [18] W. Luo, Y.-S. Li, J. Yuan et al., "Ultrasensitive fluorometric determination of hydrogen peroxide and glucose by using multiferric BiFeO₃ nanoparticles as a catalyst," *Talanta*, vol. 81, no. 3, pp. 901–907, 2010.
- [19] S. H. He, W. B. Shi, X. D. Zhang, J. A. Li, and Y. M. Huang, "β-Cyclodextrins-based inclusion complexes of CoFe₂O₄ magnetic nanoparticles as catalyst for the luminol chemiluminescence system and their applications in hydrogen peroxide detection," *Talanta*, vol. 82, no. 1, pp. 377–383, 2010.
- [20] W. B. Shi, X. D. Zhang, S. H. He, and Y. M. Huang, "CoFe₂O₄ magnetic nanoparticles as a peroxidase mimic mediated chemiluminescence for hydrogen peroxide and glucose," *Chemical Communications*, vol. 47, no. 38, pp. 10785–10787, 2011.
- [21] Y. W. Fan and Y. M. Huang, "The effective peroxidase-like activity of chitosan-functionalized CoFe₂O₄ nanoparticles for chemiluminescence sensing of hydrogen peroxide and glucose," *Analyst*, vol. 137, no. 5, pp. 1225–1231, 2012.
- [22] A. K. Dutta, S. K. Maji, D. N. Srivastava et al., "Synthesis of FeS and FeSe nanoparticles from a single source precursor: a study of their photocatalytic activity, peroxidase-like behavior, and electrochemical sensing of H₂O₂," *ACS Applied Materials and Interfaces*, vol. 4, no. 4, pp. 1919–1927, 2012.
- [23] Y. Song, K. Qu, C. Zhao, J. Ren, and X. Qu, "Graphene oxide: intrinsic peroxidase catalytic activity and its application to glucose detection," *Advanced Materials*, vol. 22, no. 19, pp. 2206–2210, 2010.
- [24] Y. Song, X. Wang, C. Zhao, K. Qu, J. Ren, and X. Qu, "Label-free colorimetric detection of single nucleotide polymorphism by using single-walled carbon nanotube intrinsic peroxidase-like activity," *Chemistry—A European Journal*, vol. 16, no. 12, pp. 3617–3621, 2010.
- [25] Y. Guo, J. Li, and S. Dong, "Hemin functionalized graphene nanosheets-based dual biosensor platforms for hydrogen peroxide and glucose," *Sensors and Actuators B: Chemical*, vol. 160, no. 1, pp. 295–300, 2011.
- [26] J. Xie, X. Zhang, H. Wang, H. Zheng, Y. Huang, and J. Xie, "Analytical and environmental applications of nanoparticles as enzyme mimetics," *TrAC—Trends in Analytical Chemistry*, vol. 39, pp. 114–129, 2012.
- [27] A. K. Gupta and M. Gupta, "Synthesis and surface engineering of iron oxide nanoparticles for biomedical applications," *Biomaterials*, vol. 26, no. 18, pp. 3995–4021, 2005.
- [28] J. Mu, Y. Wang, M. Zhao, and L. Zhang, "Intrinsic peroxidase-like activity and catalase-like activity of Co₃O₄ nanoparticles," *Chemical Communications*, vol. 48, no. 19, pp. 2540–2542, 2012.
- [29] Y. Wan, P. Qi, D. Zhang, J. Wu, and Y. Wang, "Manganese oxide nanowire-mediated enzyme-linked immunosorbent assay," *Biosensors and Bioelectronics*, vol. 33, no. 1, pp. 69–74, 2012.
- [30] R. André, F. Natálio, M. Humanes et al., "V₂O₅ nanowires with an intrinsic peroxidase-like activity," *Advanced Functional Materials*, vol. 21, no. 3, pp. 501–509, 2011.
- [31] W. Chen, J. Chen, A.-L. Liu, L.-M. Wang, G.-W. Li, and X.-H. Lin, "Peroxidase-like activity of cupric oxide nanoparticle," *ChemCatChem*, vol. 3, no. 7, pp. 1151–1154, 2011.
- [32] Y.-L. Dong, H.-G. Zhang, Z. U. Rahman et al., "Graphene oxide-Fe₃O₄ magnetic nanocomposites with peroxidase-like activity for colorimetric detection of glucose," *Nanoscale*, vol. 4, no. 13, pp. 3969–3976, 2012.
- [33] M. I. Kim, Y. Ye, M.-A. Woo, J. Lee, and H. G. Park, "A highly efficient colorimetric immunoassay using a nanocomposite entrapping magnetic and platinum nanoparticles in ordered mesoporous carbon," *Advanced Healthcare Materials*, vol. 3, no. 1, pp. 36–41, 2014.
- [34] J. Liu, X. Hu, S. Hou et al., "Au@Pt core/shell nanorods with peroxidase- and ascorbate oxidase-like activities for improved detection of glucose," *Sensors and Actuators B: Chemical*, vol. 166–167, pp. 708–714, 2012.
- [35] M. I. Kim, M. S. Kim, M.-A. Woo et al., "Highly efficient colorimetric detection of target cancer cells utilizing superior catalytic activity of graphene oxide-magnetic-platinum nanohybrids," *Nanoscale*, vol. 6, no. 3, pp. 1529–1536, 2014.
- [36] M. Liu, H. Zhao, S. Chen, H. Yu, and X. Quan, "Interface engineering catalytic graphene for smart colorimetric biosensing," *ACS Nano*, vol. 6, no. 4, pp. 3142–3151, 2012.
- [37] Y. Ye, T. Kong, X. Yu, Y. Wu, K. Zhang, and X. Wang, "Enhanced nonenzymatic hydrogen peroxide sensing with reduced graphene oxide/ferroferric oxide nanocomposites," *Talanta*, vol. 89, pp. 417–421, 2012.
- [38] R. Cui, Z. Han, and J.-J. Zhu, "Helical carbon nanotubes: intrinsic peroxidase catalytic activity and its application for biocatalysis and biosensing," *Chemistry—A European Journal*, vol. 17, no. 34, pp. 9377–9384, 2011.
- [39] M. Liu, H. Zhao, S. Chen, H. Yu, and X. Quan, "Stimuli-responsive peroxidase mimicking at a smart graphene interface," *Chemical Communications*, vol. 48, no. 56, pp. 7055–7057, 2012.
- [40] S. Liu, J. Tian, L. Wang, Y. Luo, and X. Sun, "A general strategy for the production of photoluminescent carbon nitride dots from organic amines and their application as novel peroxidase-like catalysts for colorimetric detection of H₂O₂ and glucose," *RSC Advances*, vol. 2, no. 2, pp. 411–413, 2012.
- [41] F. Qu, T. Li, and M. Yang, "Colorimetric platform for visual detection of cancer biomarker based on intrinsic peroxidase activity of graphene oxide," *Biosensors and Bioelectronics*, vol. 26, no. 9, pp. 3927–3931, 2011.
- [42] W. Shi, Q. Wang, Y. Long et al., "Carbon nanodots as peroxidase mimetics and their applications to glucose detection," *Chemical Communications*, vol. 47, no. 23, pp. 6695–6697, 2011.
- [43] X. Wang, K. Qu, B. Xu, J. Ren, and X. Qu, "Multicolor luminescent carbon nanoparticles: synthesis, supramolecular assembly with porphyrin, intrinsic peroxidase-like catalytic activity and applications," *Nano Research*, vol. 4, no. 9, pp. 908–920, 2011.
- [44] H. Wei and E. Wang, "Fe₃O₄ magnetic nanoparticles as peroxidase mimetics and their applications in H₂O₂ and glucose detection," *Analytical Chemistry*, vol. 80, no. 6, pp. 2250–2254, 2008.
- [45] Q. Chang, K. Deng, L. Zhu, G. Jiang, C. Yu, and H. Tang, "Determination of hydrogen peroxide with the aid of peroxidase-like

- Fe₃O₄ magnetic nanoparticles as the catalyst," *Microchimica Acta*, vol. 165, no. 3-4, pp. 299–305, 2009.
- [46] Z. Jiang, L. Kun, H. Ouyang, A. Liang, and H. Jiang, "A simple and sensitive fluorescence quenching method for the determination of H₂O₂ using rhodamine B and Fe₃O₄ nanocatalyst," *Journal of Fluorescence*, vol. 21, no. 5, pp. 2015–2020, 2011.
- [47] Y. Jv, B. Li, and R. Cao, "Positively-charged gold nanoparticles as peroxidase mimic and their application in hydrogen peroxide and glucose detection," *Chemical Communications*, vol. 46, no. 42, pp. 8017–8019, 2010.
- [48] K. Wang, J.-J. Xu, D.-C. Sun, H. Wei, and X.-H. Xia, "Selective glucose detection based on the concept of electrochemical depletion of electroactive species in diffusion layer," *Biosensors and Bioelectronics*, vol. 20, no. 7, pp. 1366–1372, 2005.
- [49] M. I. Kim, Y. Ye, B. Y. Won, S. Shin, J. Lee, and H. G. Park, "A highly efficient electrochemical biosensing platform by employing conductive nanocomposite entrapping magnetic nanoparticles and oxidase in mesoporous carbon foam," *Advanced Functional Materials*, vol. 21, no. 15, pp. 2868–2875, 2011.
- [50] M. I. Kim, J. Shim, T. Li, J. Lee, and H. G. Park, "Fabrication of nanoporous nanocomposites entrapping Fe₃O₄ magnetic nanoparticles and oxidases for colorimetric biosensing," *Chemistry—A European Journal*, vol. 17, no. 38, pp. 10700–10707, 2011.
- [51] M. I. Kim, J. Shim, T. Li et al., "Colorimetric quantification of galactose using a nanostructured multi-catalyst system entrapping galactose oxidase and magnetic nanoparticles as peroxidase mimetics," *Analyst*, vol. 137, no. 5, pp. 1137–1143, 2012.
- [52] M. I. Kim, J. Shim, H. J. Parab, S. C. Shin, J. Lee, and H. G. Park, "A convenient alcohol sensor using one-pot nanocomposite entrapping alcohol oxidase and magnetic nanoparticles as peroxidase mimetics," *Journal of Nanoscience and Nanotechnology*, vol. 12, no. 7, pp. 5914–5919, 2012.
- [53] K. S. Park, M. I. Kim, D.-Y. Cho, and H. G. Park, "Label-free colorimetric detection of nucleic acids based on target-induced shielding against the peroxidase-mimicking activity of magnetic nanoparticles," *Small*, vol. 7, no. 11, pp. 1521–1525, 2011.
- [54] J. A. Brinkman, M. Z. Rahmani, W. E. Jones, A. K. Chaturvedi, and M. E. Hagensee, "Optimization of PCR based detection of human papillomavirus DNA from urine specimens," *Journal of Clinical Virology*, vol. 29, no. 4, pp. 230–240, 2004.
- [55] L. Hafner, K. Beagley, and P. Timms, "Chlamydia trachomatis infection: host immune responses and potential vaccines," *Mucosal Immunology*, vol. 1, no. 2, pp. 116–130, 2008.
- [56] M. I. Kim, K. S. Park, and H. G. Park, "Ultrafast colorimetric detection of nucleic acids based on the inhibition of the oxidase activity of cerium oxide nanoparticles," *Chemical Communications*, vol. 50, no. 67, pp. 9577–9580, 2014.
- [57] Z. Zhang, Z. Wang, X. Wang, and X. Yang, "Magnetic nanoparticle-linked colorimetric aptasensor for the detection of thrombin," *Sensors and Actuators B: Chemical*, vol. 147, no. 2, pp. 428–433, 2010.
- [58] B. W. Blais and A. Martinez-Perez, "Detection of group D salmonellae including Salmonella enteritidis in eggs by polymyxin-based enzyme-linked immunosorbent assay," *Journal of Food Protection*, vol. 71, no. 2, pp. 392–396, 2008.
- [59] V. Tripathi, S. Nara, S. K. Chaube et al., "Development of rapid and sensitive one-step direct enzyme linked immunosorbent assay for 17- α -OH-progesterone in serum," *Journal of Immunoassay and Immunochemistry*, vol. 29, no. 2, pp. 117–127, 2008.
- [60] K. D. McReynolds, M. J. Hadd, and J. Gervay-Hague, "Synthesis of biotinylated glycoconjugates and their use in a novel ELISA for direct comparison of HIV-1 gp120 recognition of GalCer and related carbohydrate analogues," *Bioconjugate Chemistry*, vol. 10, no. 6, pp. 1021–1031, 1999.
- [61] H. Hocini, S. Iscaki, J.-P. Bouvet, M. D. Kazatchkine, and L. Bélec, "An ELISA method to measure total and specific human secretory IgA subclasses based on selective degradation by IgA1-protease," *Journal of Immunological Methods*, vol. 235, no. 1-2, pp. 53–60, 2000.
- [62] L. Micheli, S. Di Stefano, D. Moscone et al., "Production of antibodies and development of highly sensitive formats of enzyme immunoassay for saxitoxin analysis," *Analytical and Bioanalytical Chemistry*, vol. 373, no. 8, pp. 678–684, 2002.
- [63] L. Gao, J. Wu, S. Lyle, K. Zehr, L. Cao, and D. Gao, "Magnetite nanoparticle-linked immunosorbent assay," *Journal of Physical Chemistry C*, vol. 112, no. 44, pp. 17357–17361, 2008.
- [64] X.-Q. Zhang, S.-W. Gong, Y. Zhang, T. Yang, C.-Y. Wang, and N. Gu, "Prussian blue modified iron oxide magnetic nanoparticles and their high peroxidase-like activity," *Journal of Materials Chemistry*, vol. 20, no. 24, pp. 5110–5116, 2010.
- [65] Z. Tang, H. Wu, Y. Zhang, Z. Li, and Y. Lin, "Enzyme-mimic activity of ferric nano-core residing in ferritin and its biosensing applications," *Analytical Chemistry*, vol. 83, no. 22, pp. 8611–8616, 2011.
- [66] M.-A. Woo, M. I. Kim, J. H. Jung, K. S. Park, T. S. Seo, and H. G. Park, "A novel colorimetric immunoassay utilizing the peroxidase mimicking activity of magnetic nanoparticles," *International Journal of Molecular Sciences*, vol. 14, no. 5, pp. 9999–10014, 2013.
- [67] V. H. C. Bramwell, G. S. Doig, A. B. Tuck et al., "Changes over time of extracellular domain of HER2 (ECD/HER2) serum levels have prognostic value in metastatic breast cancer," *Breast Cancer Research and Treatment*, vol. 114, no. 3, pp. 503–511, 2009.
- [68] K. S. Asgeirsson, A. Agrawal, C. Allen et al., "Serum epidermal growth factor receptor and HER2 expression in primary and metastatic breast cancer patients," *Breast Cancer Research*, vol. 9, no. 6, article R75, 2007.
- [69] A. Asati, C. Kaittanis, S. Santra, and J. M. Perez, "PH-tunable oxidase-like activity of cerium oxide nanoparticles achieving sensitive fluorogenic detection of cancer biomarkers at neutral pH," *Analytical Chemistry*, vol. 83, no. 7, pp. 2547–2553, 2011.
- [70] K. L. Fan, C. Q. Cao, Y. X. Pan et al., "Magnetoferritin nanoparticles for targeting and visualizing tumour tissues," *Nature Nanotechnology*, vol. 7, no. 7, pp. 459–464, 2012.
- [71] S. Beatty, H.-H. Koh, M. Phil, D. Henson, and M. Boulton, "The role of oxidative stress in the pathogenesis of age-related macular degeneration," *Survey of Ophthalmology*, vol. 45, no. 2, pp. 115–134, 2000.
- [72] C. Korsvik, S. Patil, S. Seal, and W. T. Self, "Superoxide dismutase mimetic properties exhibited by vacancy engineered ceria nanoparticles," *Chemical Communications*, no. 10, pp. 1056–1058, 2007.
- [73] E. G. Heckert, A. S. Karakoti, S. Seal, and W. T. Self, "The role of cerium redox state in the SOD mimetic activity of nanoceria," *Biomaterials*, vol. 29, no. 18, pp. 2705–2709, 2008.
- [74] J. Chen, S. Patil, S. Seal, and J. F. McGinnis, "Rare earth nanoparticles prevent retinal degeneration induced by intracellular peroxides," *Nature Nanotechnology*, vol. 1, no. 2, pp. 142–150, 2006.

- [75] S. M. Hirst, A. S. Karakoti, R. D. Tyler, N. Sriranganathan, S. Seal, and C. M. Reilly, "Anti-inflammatory properties of cerium oxide nanoparticles," *Small*, vol. 5, no. 24, pp. 2848–2856, 2009.
- [76] D.-M. Huang, J.-K. Hsiao, Y.-C. Chen et al., "The promotion of human mesenchymal stem cell proliferation by superparamagnetic iron oxide nanoparticles," *Biomaterials*, vol. 30, no. 22, pp. 3645–3651, 2009.
- [77] N. Ding, N. Yan, C. Ren, and X. Chen, "Colorimetric determination of melamine in dairy products by Fe₃O₄ Magnetic nanoparticles-H₂O₂-ABTS detection system," *Analytical Chemistry*, vol. 82, no. 13, pp. 5897–5899, 2010.
- [78] J. Zhang, J. Zhuang, L. Gao et al., "Decomposing phenol by the hidden talent of ferromagnetic nanoparticles," *Chemosphere*, vol. 73, no. 9, pp. 1524–1528, 2008.
- [79] J. Z. Jiang, J. Zou, L. H. Zhu, L. Huang, H. Jiang, and Y. Zhang, "Degradation of methylene blue with H₂O₂ activated by peroxidase-like Fe₃O₄ magnetic nanoparticles," *Journal of Nanoscience and Nanotechnology*, vol. 11, no. 6, pp. 4793–4799, 2011.
- [80] L. Gao, K. M. Giglio, J. L. Nelson, H. Sondermann, and A. J. Travis, "Ferromagnetic nanoparticles with peroxidase-like activity enhance the cleavage of biological macromolecules for biofilm elimination," *Nanoscale*, vol. 6, no. 5, pp. 2588–2593, 2014.
- [81] K. Vickery, A. Pajkos, and Y. Cossart, "Removal of biofilm from endoscopes: evaluation of detergent efficiency," *American Journal of Infection Control*, vol. 32, no. 3, pp. 170–176, 2004.

Research Article

Autophagy in RAW264.7 Cells Treated with Surface-Functionalized Graphene Oxides

Chang Seok Park,¹ Kyoung Soon Choi,² In Won Park,¹ Jae Woo Jung,¹ Jae Chol Choi,¹ Jae Yeol Kim,¹ Byoung Whui Choi,¹ Yu Geun Kim,² Jong Wook Shin,¹ and Soo Young Kim²

¹Department of Internal Medicine, Chung-Ang University College of Medicine, 221 Heukseok-dong, Dongjak-gu, Seoul 156-756, Republic of Korea

²School of Chemical Engineering and Materials Science, Chung-Ang University, 221 Heukseok-dong, Dongjak-gu, Seoul 156-756, Republic of Korea

Correspondence should be addressed to Jong Wook Shin; basthma@cau.ac.kr and Soo Young Kim; sooyoungkim@cau.ac.kr

Received 19 May 2015; Accepted 21 July 2015

Academic Editor: Jin W. Seo

Copyright © 2015 Chang Seok Park et al. This is an open access article distributed under the Creative Commons Attribution License, which permits unrestricted use, distribution, and reproduction in any medium, provided the original work is properly cited.

This study investigated cytotoxicity, particularly autophagy, in RAW264.7 cells exposed to graphene oxide (GO) and its derivatives (dodecylamine-GO (DA-GO), reduced GO (rGO), and sodium dodecyl sulfate-rGO (SDS-rGO)). Appearance of amine stretching bands, out-of-plane C-H stretching vibrations, and S=O stretching bands in infrared spectra indicated the formation of DA-GO, rGO, and SDS-rGO, respectively. Light microscopy and microculture tetrazolium assay showed that all the GO types exerted cytotoxic effects on RAW264.7 cells in a concentration-dependent manner. Higher concentrations of the GO types downregulated the expression of PU.1, a unique transcription factor in monocytes and macrophages, and decreased the conversion of LC3A/B-I to LC3A/B-II, suggesting that PU.1 was associated with autophagy in RAW264.7 cells. These results suggested that surface-functionalized GOs exerted cytotoxic effects in a concentration-dependent manner by changing the expression of critical genes and inducing autophagy in macrophages.

1. Introduction

Nanomaterials have diverse applications because of their extraordinary physicochemical characteristics. In the last decade, several novel nanomaterials have been developed that have found applications in tissue engineering and regenerative medicine. Nanomaterials affect the immune system, especially macrophages and lymphocytes, thus significantly affecting human health [1]. Graphene, which is characterized by a two-dimensional honeycomb lattice carbon structure, is a potential nanomaterial [2]. Different graphene subtypes, for example, graphene made by chemical vapor deposition, graphene nanoribbons, graphene oxide (GO), and reduced GO (rGO), can be obtained by employing different fabrication methods. Uniformly structured graphene is used as an intracellular carrier in immune cells [3]. Its favorable biological properties such as interaction with RNA and DNA, cellular adhesion, cellular uptake, antibacterial activity,

and good biodegradability have increased its application in the biological field. This in turn will increase the industrial production of graphene. As a result, graphene dust may inevitably spread into the environment and may exert harmful effects on human health. Therefore, it is important to analyze the nanosafety and nanotoxicity of graphene materials.

Unique properties of graphene are important under *in vivo* or intracellular conditions as well as under *ex vivo* or extracellular conditions. GO and rGO effectively inhibit the growth of bacteria, with minimal cytotoxic effects [4]. RAW264.7 mouse macrophage cell line has long been used as an *in vitro* model for studying the response of inflammatory molecules to various synthetic stimuli. Macrophages are the first immune response cells that represent the innate immune system. Macrophage response is critical for survival at cell, tissue, organ, and system levels. Therefore, dose- and size-related effects of GO or rGO on the morphology, viability,

and mortality of RAW264.7 cells should be considered while developing biomedical applications of GO. Most previous studies have used rGO or GO without any surface treatments. However, the physicochemical properties of GO depend on its surface [5]. The most critical issue associated with the use of rGO or GO in biomedical applications is to establish versatile functionalization methods for producing GOs that are surface functionalized with biomolecules or biomaterials, with minimal detrimental effects on the bioactivity of these compounds. Therefore, the effect of surface-functionalized GOs on the viability of RAW264.7 cells should be analyzed to determine their nanosafety. Furthermore, surface-functionalized GO-induced intracellular molecular and genetic mechanisms in RAW264.7 cells must be elucidated for determining health care and environmental controls.

Cell death occurs in the form of necrosis, apoptosis, and other forms of programmed or nonprogrammed cell death, including autophagy, which has been acknowledged recently. Autophagy is defined as nanomaterial-associated cellular injury [6]. Autophagy involves degradation of intracellular components in response to stress, and it is negatively controlled by mammalian target of rapamycin complex 1 (mTORC1). Inhibition of mTORC1 kinase activity promotes the formation of an autophagosome containing a complex composed of Beclin 1 and other factors. Formation of the autophagosome also involves the conversion of microtubule-associated protein light chain 3 (LC3A/B-I) to its lipidated form LC3A/B-II. Thus, conversion of LC3A/B-I to LC3A/B-II is a common indicator of autophagy. A study on mechanisms underlying the death of RAW264.7 cells is essential to elucidate the effects of surface-functionalized GOs on the viability of these cells. Therefore, the present study investigated the differential cellular effects of surface-functionalized GOs on the viability of and gene expression in monocytes and macrophages.

GO was produced using a modified Hummers method, and rGO was produced using hydrazine hydrate [7]. Dodecylamine (DA) and sodium dodecyl sulfate (SDS) were used to functionalize GO or rGO. Fourier transform infrared spectroscopy (FTIR) was used to determine the results of surface functionalization. Optical microscopy was used to investigate cell viability. The measurements obtained were used to elucidate the effects of GO, DA-GO, rGO, and SDS-rGO on the viability of RAW264.7 cells and the mechanisms underlying their death.

2. Materials and Methods

2.1. Synthesis of GO. GO was prepared using a modified Hummers method. Briefly, 2 g graphite powder (universal grade, 200 mesh, 99.9995%; Alfa Aesar) was stirred with 2 g NaNO_3 and 100 mL concentrated H_2SO_4 for 1 day in an ice water bath. After stirring, 12 g KMnO_4 was gradually added to the solution. After thoroughly mixing the solution, the ice bath was removed and the solution was stirred at 35°C until a highly viscous liquid was obtained. Next, 200 mL pure water and H_2O_2 were added sequentially to the viscous liquid, and the mixture was centrifuged at 8000 rpm and washed with

HCl and water. The centrifugation and washing steps were repeated at least five times. Finally, the GO obtained was dried at 50°C for 24 h in a vacuum oven.

2.2. Synthesis of DA-GO. GO was dispersed in 200 mL deionized water to obtain a concentration of 2 mg/mL. The dispersed GO was ultrasonicated for 30 min by using WUC-A03H bath-type sonicator (Daihan Scientific, Korea). The GO dispersion was then centrifuged for 15 min at 3000 rpm to remove unexfoliated GO. Next, 100 mL of the brown-colored dispersion was transferred to a 250 mL beaker. DA (0.1853 g) dissolved in 100 mL ethanol was added to the GO dispersion, and the solution was stirred at room temperature for 2 h. Nucleophilic substitution occurred between the amino moiety of DA and the epoxy moiety of GO. This DA-functionalized GO dispersion was washed with ethanol to remove excess DA adsorbed on the surface of the modified GO. The reaction product was washed with deionized water to remove excess ethanol. The dark brown powder was dried under vacuum at 60°C for 24 h to obtain DA-GO.

2.3. Synthesis of rGO. rGO was synthesized from GO by using hydrazine hydrate. First, 0.1 g GO was dispersed in 100 mL deionized water by ultrasonication. Next, 1 mL hydrazine hydrate (N_2H_4 [50%–60%], reagent grade; Sigma-Aldrich) was added to the GO dispersion. After stirring for 10 min, the solution was transferred to an oil bath fitted with a water-cooled condenser, and it was heated at 90°C for 24 h. The reaction product was washed with deionized water to remove excess hydrazine hydrate. The final product was then dried in a vacuum oven at 60°C.

2.4. Synthesis of SDS-rGO. For SDS modification, rGO was dispersed in 200 mL deionized water to achieve a concentration of 2 mg/mL by performing ultrasonication for 30 min in VCX-750 probe-type sonicator (Sonics & Materials, Inc., USA). Next, 14.419 g SDS (ACS reagent, $\geq 99.0\%$; Sigma-Aldrich) was added to the rGO dispersion, and the solution was stirred at room temperature for 2 h. The SDS-modified rGO (SDS-rGO) dispersion was then washed with deionized water to remove excess SDS. The black powder obtained was dried under vacuum at 60°C for 24 h.

2.5. Materials. Dulbecco's modified Eagle's medium (DMEM; Gibco), fetal bovine serum (FBS; Gibco), penicillin/streptomycin (Gibco), 3-(4,5-dimethylthiazol-2-yl)-2,5-diphenyltetrazolium bromide (MTT), NaCl, Tween-20, Trizma base, glycine, and HCl were purchased from Sigma-Aldrich. PRO-PREP Protein Extraction Kit and SMART BCA Protein Assay Kit were purchased from Intron. Antibodies against glyceraldehyde-3-phosphate dehydrogenase (GAPDH), pan-actin (p-Act), LC3A/B-I, LC3A/B-II, and PU.1 were purchased from Cell Signaling.

2.6. Cell Culture and Treatment with the GO Types. Murine RAW264.7 macrophages were purchased from ATCC and cultured in DMEM supplemented with 10% FBS, 100 $\mu\text{g}/\text{mL}$ streptomycin, and 100 U/mL penicillin at 37°C in 5% CO_2 atmosphere. Four GO types, that is, GO, DA-GO, rGO, and

SDS-rGO, were used in the study. For treatment with each GO type, the cells were seeded in proper culture plates (24-well plates, $\sim 100\phi$, and 100 mm diameter) at an appropriate seeding density and cultured overnight with indicated concentrations of each GO type for 24 or 48 h.

2.7. Light Microscopy. Cell morphology was examined under a phase-contrast microscope (Olympus IX71) at 100x magnification. RAW264.7 cells were plated in 12-well plates (cell density, 2.5×10^5 cells per well) and were incubated for 24 h for stabilization. The cells were then treated with GO, DA-GO, rGO, and SDS-rGO at indicated concentrations (5, 25, and 50 $\mu\text{g}/\text{mL}$ for DA-GO and 5, 50, and 200 $\mu\text{g}/\text{mL}$ for GO, rGO, and SDS-rGO, resp.) for 24 or 48 h. RAW264.7 cells cultured in a complete medium without any GO type were used as controls. All images were recorded and digitalized using Olympus DP70 and its software program.

2.8. Cytotoxicity Assay. Cytotoxicity of each GO type was evaluated by performing MTT assay. Briefly, 5 mg/mL MTT solution was prepared in phosphate buffered saline (PBS; Gibco). The solution was sterilized using a syringe filter (0.2 μm pore size, GVS). RAW264.7 cells were plated in 24-well plates (cell density, 1.5×10^5 cells per well) and were incubated for 24 h for stabilization. The cells were then treated separately with GO, DA-GO, rGO, and SDS-rGO at concentrations ranging from 800 to 0.8 $\mu\text{g}/\text{mL}$, which were obtained by diluting the GO types with the culture medium. RAW264.7 cells cultured in a medium without the GO types were used as controls. Culture medium without the RAW264.7 cells or GO types was used as blank. After 24 and 48 h of incubation, the cells were rinsed twice with cold sterile PBS. Next, 10% MTT solution in the complete medium was added to each well, and the cells were incubated for additional 4 h at 37°C. Next, 100 μL 10% SDS solution was added to each well, and the cells were incubated for more than 4 h at 37°C to dissolve formazan precipitates in viable cells. Liquefied samples were agitated for 30 s to mix cells with GO thoroughly. Next, the samples were centrifuged at 14000 rpm for 30 min to precipitate the GO derivatives. Optical density was measured at 540 nm by using a microplate reader (Spectramax 340PC384; Molecular Devices), with 670 nm as the reference wavelength. The experiment was repeated thrice.

2.9. Protein Extraction and Western Blot Analysis. Each GO type was categorized into 3 groups based on its concentration (low, medium, and high concentrations). The concentrations were 5, 25, and 50 $\mu\text{g}/\text{mL}$ for DA-GO and 5, 50, and 200 $\mu\text{g}/\text{mL}$ for the other GO types. Total proteins were extracted by rinsing the treated cells twice with ice-cold PBS and subsequently lysing the cells in the PRO-PREP solution by using cell scrappers. The extracted components were incubated at -20°C for 20 min and then centrifuged at 15000 rpm and 4°C for 30 min. Clear supernatants containing total proteins were collected, and protein concentrations were determined using the SMART BCA Protein Assay Kit. Equal amounts of proteins were separated by performing sodium dodecyl sulfate-polyacrylamide gel electrophoresis and were

transferred onto polyvinylidene fluoride membranes. The membranes were blocked with 5% nonfat milk and were incubated overnight with primary antibodies at 4°C with gentle agitation. The membranes were then incubated with appropriate secondary antibodies, and protein bands were detected using Dogen Pico or Femto Chemiluminescence Kit. Densities of protein bands were quantified using Image Lab imaging processing program. Because the extent of the conversion of LC3A/B-I to LC3A/B-II is correlated with the level of autophagy, levels of LC3A/B-I and LC3A/B-II were detected by performing western blot analysis. Conversion of LC3A/B was determined using the following formula: band density of LC3A/B-II/(band density of LC3A/B-I + band density of LC3A/B-II). Expression of p-Act, GAPDH (internal control), and PU.1 (transcription factor that serves an indicator of RAW264.7 cells) was also examined.

3. Results and Discussion

Figure 1 shows the FTIR spectra of (a) GO, (b) DA-GO, (c) rGO, and (d) SDS-rGO. Expected structures of each GO type are shown in the inset of Figure 1. A broad peak at 3437 cm^{-1} corresponding to O-H stretching was observed for all the samples, suggesting that rGO and SDS-rGO contained some oxygen bonds even though their oxygen content decreased after reduction. Another peak at 1636 cm^{-1} was also observed for all the samples, indicating the presence of graphitic sp_2 bonds. Peaks around $1700\text{--}1733\text{ cm}^{-1}$ and at 1272 cm^{-1} were observed for GO, indicating the presence of carboxyl and epoxy groups, respectively. However, these peaks were not observed for other samples, suggesting that the carboxyl and/or epoxy groups reacted with DA in DA-GO and were reduced in rGO and SDS-rGO. The remaining peaks for GO were observed at 1380 (CH_3 bending) and 1056 cm^{-1} , which is typical for primary alcohols [8]. New peaks at 2955, 2922, and 2852 cm^{-1} for DA-GO corresponded to C-H stretching vibrations of CH_3 , CH_2 , and, CH groups, respectively. Peaks at 1644, 1457, 1265, and 1012 cm^{-1} for DA-GO corresponded to carbonyl stretching vibrations of an amide-carbonyl bond, an amine group, an amine stretching band, and a primary alcohol in phenolic compounds, respectively [9, 10]. Presence of these peaks confirmed that GO was successfully modified with DA. Peaks at 998 and 990 cm^{-1} for rGO and SDS-rGO, respectively, corresponded to out-of-plane C-H stretching vibrations and suggested sufficient reduction of GO. A new peak at 1168 cm^{-1} for SDS-rGO corresponded to S=O stretching and indicated that small amounts of SDS existed on the surface of rGO. These data indicated that all the samples were modified as intended.

The morphology of a cell is an important indicator of its viability. Figure 2 shows microscopic images of RAW264.7 cells treated with (a) GO, (b) DA-GO, (c) rGO, and (d) SDS-rGO. The cells were exposed to 3 concentrations of GOs. Researchers or workers are likely to be exposed to low concentrations (5 $\mu\text{g}/\text{mL}$) of GOs. Intermediate (50 $\mu\text{g}/\text{mL}$) and high (200 $\mu\text{g}/\text{mL}$) concentrations of GO were examined to determine the effect of long-term exposure to GOs. Cellular morphology was conserved in almost all the cells

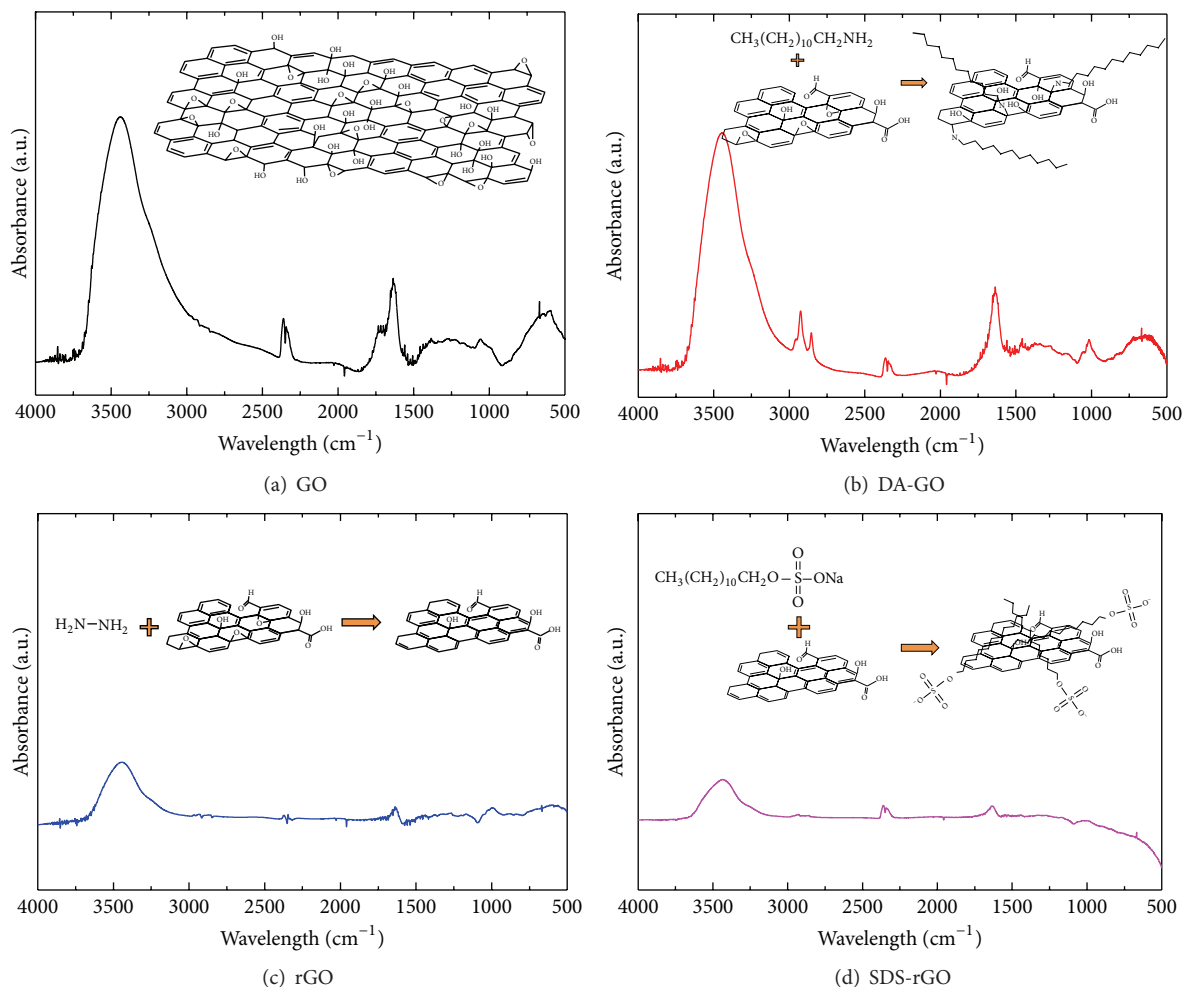


FIGURE 1: FTIR spectra of (a) GO, (b) DA-GO, (c) rGO, and (d) SDS-rGO.

exposed to lower concentrations of each GO type. However, cells exposed to higher concentrations of all the GO types had dysmorphic appearance. RAW264.7 cells showed loosely adherent, spindle, ovoid, or round shapes, which are characteristics of injured cells. Furthermore, cellular debris was detected in cell samples treated with all the GO types, which increased with an increase in the concentration of the GO types.

Figure 3 shows the cytotoxicity of various GO types determined by performing the MTT assay. Cell viability decreased with an increase in the concentration of GOs, regardless of the GO type. Cell viability decreased linearly in cells treated with GO and decreased rapidly in cells treated with higher concentrations ($>25 \mu\text{g/mL}$) of rGO and SDS-rGO. Cells treated with $0.8 \mu\text{g/mL}$ DA-GO showed remarkably decreased viability that was also observed in cells treated with $12.5 \mu\text{g/mL}$ DA-GO. Cells treated with DA-GO concentrations higher than $12.5 \mu\text{g/mL}$ showed a rapid decrease in viability, suggesting that GO types with different functional groups exerted different cytotoxic effects. No difference was observed in the concentration-dependent decrease in cell viability between cells treated for 24 and 48 h.

Figure 4 shows the results of western blot analysis of cells treated with (a) GO, (b) DA-GO, (c) rGO, and (d) SDS-rGO. Expression of p-Act decreased in a dose-dependent manner in all the samples. In contrast, expression of GAPDH was constant in all the samples. Therefore, GAPDH was used as a housekeeping gene for normalizing the semiquantitative analysis of gene expression. PU.1, NF κ B, and AP-1 are representative transcription factors in cells belonging to the monocyte lineage. Surface-functionalized GOs downregulated the expression of PU.1 in a concentration-dependent manner. The ratio of conversion of LC3A/B-I to LC3A/B-II also decreased in a dose-dependent manner except for RAW264.7 cells with SDS-rGO at a concentration of $200 \mu\text{g/mL}$ for 48 h, which was similar to that observed with PU.1.

Based on these observations, the effects of GO and its functionalized derivatives on autophagy in monocytes/macrophages can be explained as follows. Macrophages engulf graphene materials and convert them into biodegradable intracellular nanomaterials [11, 12]. Macrophages inhibit the endocytosis of polyethylene glycol- and bovine serum albumin-functionalized graphene but stimulate the endocytosis of polyetherimide-functionalized graphene [13, 14].

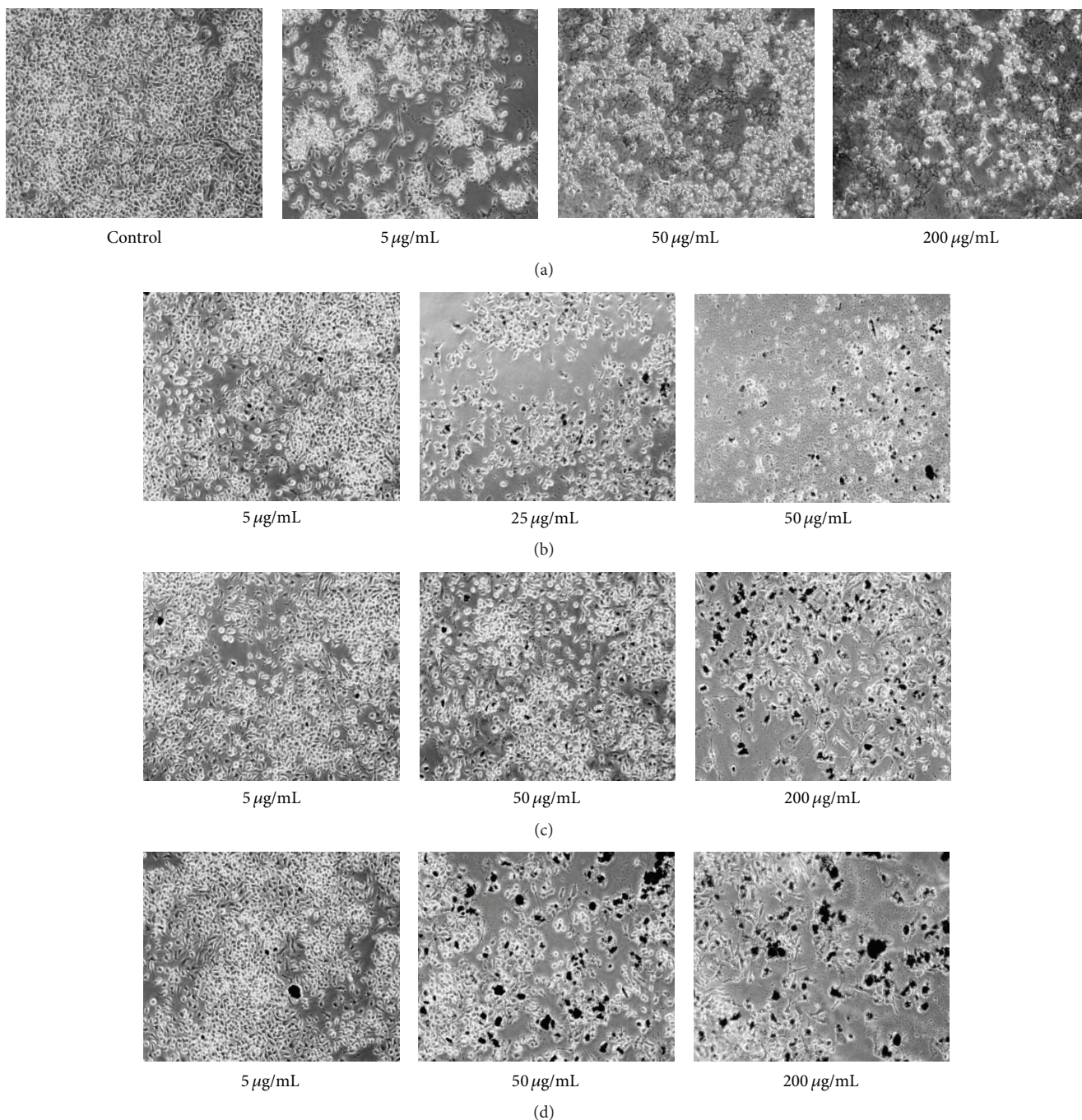


FIGURE 2: Microscopic images showing morphological changes in RAW264.7 cells exposed to (a) GO, (b) DA-GO, (c) rGO, and (d) SDS-rGO at the indicated concentrations for 24 h. Exposure to each GO type exerted cytotoxic effects on RAW264.7 cells.

These results indicate that surface-functionalized graphene exerts diverse effects from biodegradation to nanotoxicity that may injure various organs [15].

Graphene induces apoptosis, autophagy, and inflammation in macrophages through $\text{NF}\kappa\text{B}$ or p38 MAPK by increasing the expression of $\text{TNF-}\alpha$ [16, 17]. Autophagy is a type of programmed cell death, like apoptosis. Autophagy involves multiple processes such as phagocytosis or endocytosis, formation of the autophagosome, recycling of intracellular

proteins, and degradation of extracellular antigens. At the cellular level, autophagy can determine cell fate, that is, survival or death. LC3 processing is a marker of autophagy because it is a major step in the formation of the autophagosome. Generally, conversion of LC3A/B-I to LC3A/B-II indicates the activation of autophagy because it involves ubiquitinase-like enzymes that cause the selective degradation of target molecules [18]. In the present study, the ratio of conversion of LC3A/B-I to LC3A/B-II decreased in a dose-dependent

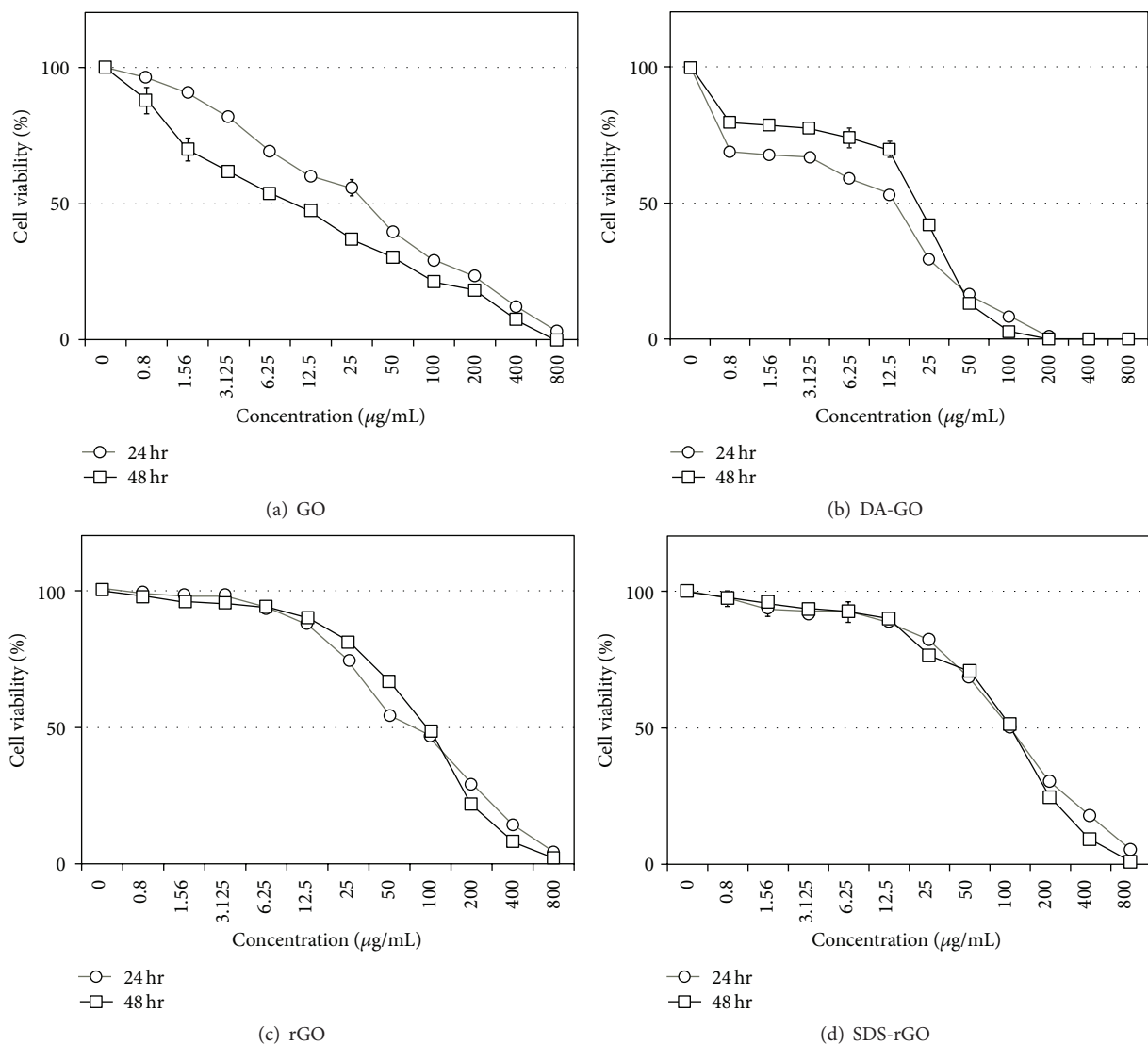


FIGURE 3: Viability of RAW264.7 cells treated with (a) GO, (b) DA-GO, (c) rGO, and (d) SDS-rGO.

manner (Figure 4), suggesting that autophagy was one of the cell death processes in macrophages with the different degrees of contribution. PU.1 is one of the transcription factors in monocytes and plays pivotal roles in the expression of various genes [19, 20]. Expression of PU.1 indicates the involvement of apoptotic pathways [21, 22]. Interestingly, exposure of RAW264.7 cells to higher concentrations of GO types decreased the expression of PU.1 and conversion of LC3A/B-I to LC3A/B-II. These results suggest that PU.1 plays a regulatory role in inducing autophagy in RAW264.7 cells. Furthermore, GAPDH expression was not affected by the increase in the concentrations of GO types. To the best of our knowledge, this is the first report on constant GAPDH expression in macrophages exposed to surface-functionalized GOs. Therefore, GAPDH may be used instead of p-Act to normalize gene expression in macrophages. These results highlight the need for further studies to determine

mechanisms underlying immune response or cellular toxicity, including autophagy, to establish strategies for preventing or treating respiratory and immunological toxicities in humans. Furthermore, these results indicate that appropriate preparation of GOs is necessary in manufacturing plants and industrial environments.

4. Conclusion

This study investigated the cytotoxic effects of GO, DA-GO, rGO, and SDS-rGO on RAW264.7 cells. Appearance of amine stretching bands, out-of-plane C-H stretching vibrations, and S=O stretching in FTIR spectra indicated the formation of DA-GO, rGO, and SDS-rGO, respectively. Light microscopy and MTT assay showed that all the GO types exerted cytotoxic effects in a concentration-dependent manner. Western blot analysis confirmed cytotoxicity, decreased expression

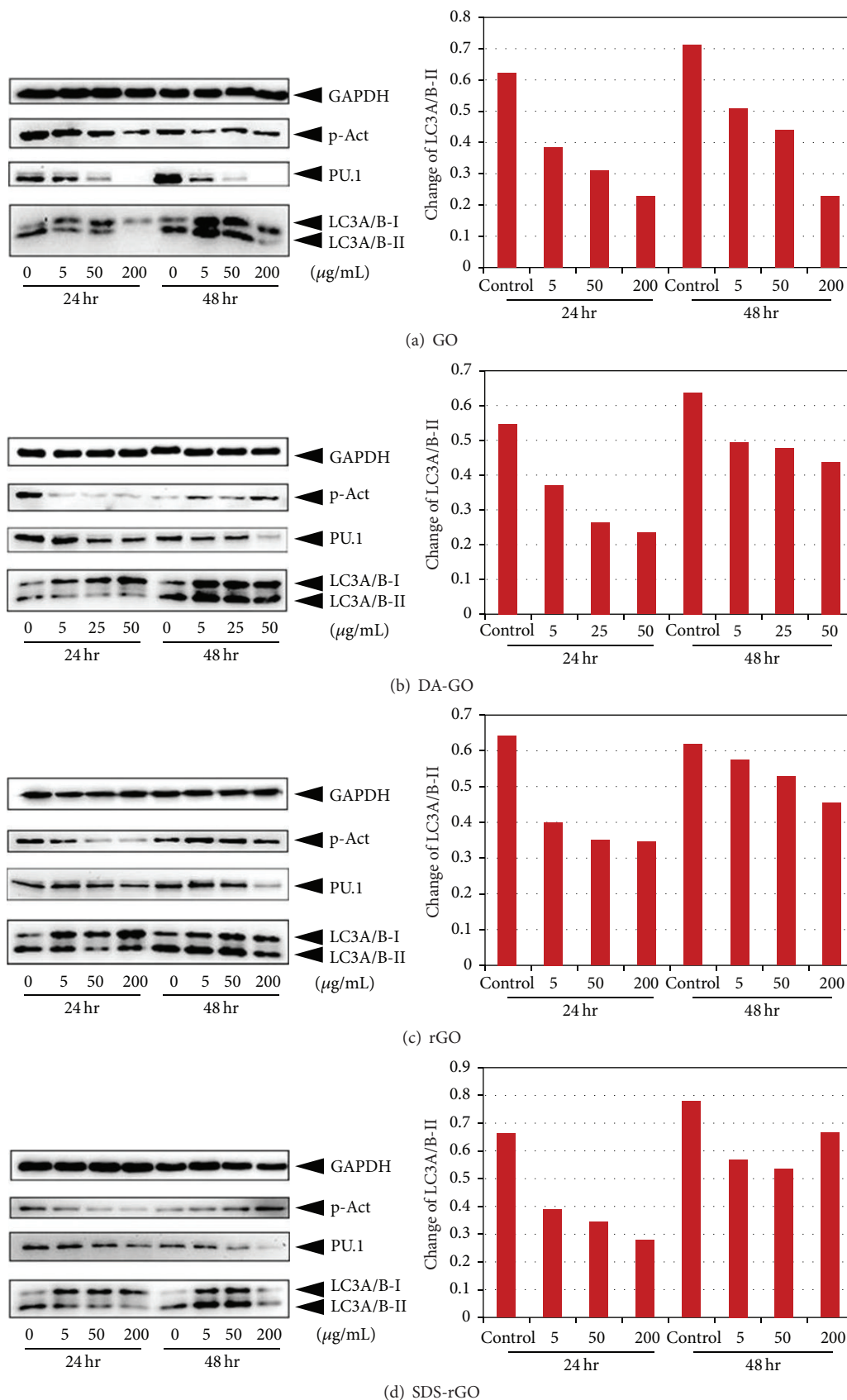


FIGURE 4: Expression of GAPDH, p-Act, PU.1, and autophagy marker proteins in RAW264.7 cells treated with the different concentrations of GO types for different treatment durations. (a) Representative results of western blot analysis of each protein. (b) Changes in the ratio of LC3A/B-II/(LC3A/B-I + LC3A/B-II) as a function of GO concentration and treatment duration. Level of LC3A/B-I and LC3A/B-II expression was analyzed by western blot analysis by using specific antibodies.

of PU.1, and induction of autophagy in a concentration-dependent manner in macrophages treated with the 4 GO types. These results suggested that surface-functionalized GOs exerted cytotoxic effects in a concentration-dependent manner by changing the expression of critical genes and by inducing autophagy.

Conflict of Interests

The authors declare that there is no conflict of interests regarding the publication of this paper.

Authors' Contribution

Chang Seok Park and Kyoung Soon Choi contributed equally to this work.

Acknowledgments

This work was supported in part by a Research Scholarship Grant of 2015 from the Chung-Ang University and by a grant from the National Research Foundation of Korea that is funded by the Korean government (MSIP; no. 2014R1A2A1A11051).

References

- [1] M. Orecchioni, D. Bedognetti, F. Sgarrella, F. M. Marincola, A. Bianco, and L. G. Delogu, "Impact of carbon nanotubes and graphene on immune cells," *Journal of Translational Medicine*, vol. 12, no. 1, article no. 138, 2014.
- [2] K. C. Kwon, K. S. Choi, B. J. Kim, J.-L. Lee, and S. Y. Kim, "Work-function decrease of graphene sheet using alkali metal carbonates," *The Journal of Physical Chemistry C*, vol. 116, no. 50, pp. 26586–26591, 2012.
- [3] J. Sun, J. Chao, J. Huang et al., "Uniform small graphene oxide as an efficient cellular nanocarrier for immunostimulatory CpG oligonucleotides," *ACS Applied Materials & Interfaces*, vol. 6, no. 10, pp. 7926–7932, 2014.
- [4] C. Bussy, H. Ali-Boucetta, and K. Kostarelos, "Safety considerations for graphene: lessons learnt from carbon nanotubes," *Accounts of Chemical Research*, vol. 46, no. 3, pp. 692–701, 2013.
- [5] Y. Li, L. Feng, X. Shi et al., "Surface coating-dependent cytotoxicity and degradation of graphene derivatives: towards the design of non-toxic, degradable nano-graphene," *Small*, vol. 10, no. 8, pp. 1544–1554, 2014.
- [6] B. Wan, Z.-X. Wang, Q.-Y. Lv et al., "Single-walled carbon nanotubes and graphene oxides induce autophagosome accumulation and lysosome impairment in primarily cultured murine peritoneal macrophages," *Toxicology Letters*, vol. 221, no. 2, pp. 118–127, 2013.
- [7] C. Y. Lee, Q. V. Le, C. Kim, and S. Y. Kim, "Use of silane-functionalized graphene oxide in organic photovoltaic cells and organic light-emitting diodes," *Physical Chemistry Chemical Physics*, vol. 17, no. 14, pp. 9369–9374, 2015.
- [8] H. Wang, Q. Hao, X. Yang, L. Lu, and X. Wang, "Effect of graphene oxide on the properties of its composite with polyaniline," *ACS Applied Materials and Interfaces*, vol. 2, no. 3, pp. 821–828, 2010.
- [9] T. Kuila, P. Khanra, A. K. Mishra, N. H. Kim, and J. H. Lee, "Functionalized-graphene/ethylene vinyl acetate co-polymer composites for improved mechanical and thermal properties," *Polymer Testing*, vol. 31, no. 2, pp. 282–289, 2012.
- [10] G. Wang, X. Shen, B. Wang, J. Yao, and J. Park, "Synthesis and characterisation of hydrophilic and organophilic graphene nanosheets," *Carbon*, vol. 47, no. 5, pp. 1359–1364, 2009.
- [11] J. H. Shin, S. G. Han, J. K. Kim et al., "5-Day repeated inhalation and 28-day post-exposure study of graphene," *Nanotoxicology*, pp. 1–9, 2015.
- [12] M. Zhang, M. Yang, C. Bussy, S. Iijima, K. Kostarelos, and M. Yudasaka, "Biodegradation of carbon nanohorns in macrophage cells," *Nanoscale*, vol. 7, no. 7, pp. 2834–2840, 2015.
- [13] N. Luo, D. Ni, H. Yue, W. Wei, and G. Ma, "Surface-engineered graphene navigate divergent biological outcomes toward macrophages," *ACS Applied Materials & Interfaces*, vol. 7, no. 9, pp. 5239–5247, 2015.
- [14] J. Linares, M. C. Matesanz, M. Vila et al., "Endocytic mechanisms of graphene oxide nanosheets in osteoblasts, hepatocytes and macrophages," *ACS Applied Materials & Interfaces*, vol. 6, no. 16, pp. 13697–13706, 2014.
- [15] V. Volarevic, V. Paunovic, Z. Markovic et al., "Large graphene quantum dots alleviate immune-mediated liver damage," *ACS Nano*, vol. 8, no. 12, pp. 12098–12109, 2014.
- [16] Y. Qin, Z.-W. Zhou, S.-T. Pan et al., "Graphene quantum dots induce apoptosis, autophagy, and inflammatory response via p38 mitogen-activated protein kinase and nuclear factor- κ B mediated signaling pathways in activated THP-1 macrophages," *Toxicology*, vol. 327, pp. 62–76, 2015.
- [17] M. J. Feito, M. Vila, M. C. Matesanz et al., "In vitro evaluation of graphene oxide nanosheets on immune function," *Journal of Colloid and Interface Science*, vol. 432, pp. 221–228, 2014.
- [18] D. Glick, S. Barth, and K. F. Macleod, "Autophagy: cellular and molecular mechanisms," *The Journal of Pathology*, vol. 221, no. 1, pp. 3–12, 2010.
- [19] A. Haimovici, D. Brigger, B. E. Torbett, M. F. Fey, and M. P. Tschan, "Induction of the autophagy-associated gene MAP1S via PU.1 supports APL differentiation," *Leukemia Research*, vol. 38, no. 9, pp. 1041–1047, 2014.
- [20] D. Brigger, T. Proikas-Cezanne, and M. P. Tschan, "WIPI-Dependent autophagy during neutrophil differentiation of NB4 acute promyelocytic leukemia cells," *Cell Death & Disease*, vol. 5, no. 7, Article ID e1315, 2014.
- [21] S. Ueno, H. Tatetsu, H. Hata et al., "PU.1 induces apoptosis in myeloma cells through direct transactivation of TRAIL," *Oncogene*, vol. 28, no. 46, pp. 4116–4125, 2009.
- [22] M. Zhao, X.-F. Duan, D.-H. Wen, and G.-Q. Chen, "PU.1, a novel caspase-3 substrate, partially contributes to chemotherapeutic agents-induced apoptosis in leukemic cells," *Biochemical and Biophysical Research Communications*, vol. 382, no. 3, pp. 508–513, 2009.

Research Article

Colorimetric Detection System for *Salmonella typhimurium* Based on Peroxidase-Like Activity of Magnetic Nanoparticles with DNA Aptamers

Ji Young Park,¹ Ha Young Jeong,¹ Moon Il Kim,² and Tae Jung Park¹

¹Department of Chemistry, Chung-Ang University, 84 Heukseok-ro, Dongjak-gu, Seoul 156-756, Republic of Korea

²Department of BioNano Technology, Gachon University, 1342 Seongnamdae-ro, Sujeoung-gu, Seongnam-si, Gyeonggi-do 461-701, Republic of Korea

Correspondence should be addressed to Tae Jung Park; tjpark@cau.ac.kr

Received 2 June 2015; Revised 16 July 2015; Accepted 21 July 2015

Academic Editor: Wei Chen

Copyright © 2015 Ji Young Park et al. This is an open access article distributed under the Creative Commons Attribution License, which permits unrestricted use, distribution, and reproduction in any medium, provided the original work is properly cited.

Recently, much attention has been devoted to food-related health issues. In particular, food-poisoning bacteria are becoming a serious threat to human health. So far, techniques used to detect these bacteria are time-consuming and laborious. To overcome these challenges, a biosensor with a simple platform was developed to detect *Salmonella typhimurium*. The colorimetric strategy is attractive because it enables simple and rapid sensing with the naked eyes. We used magnetic nanoparticles (MNPs), specific aptamers, and a colorimetric substrate, 3,3',5,5'-tetramethylbenzidine (TMB) in the presence of H₂O₂. Because MNPs display enzyme-like activities, they can undergo color changes with the help of a colorimetric substrate. In this system, MNPs were first incubated with aptamers that specifically interact with the *Salmonella* species, reducing the peroxidase activity of the MNPs via DNA-mediated shielding of catalytic activity. After the addition of *Salmonella* cells to the solution, specific aptamers on the MNPs interact with the *Salmonella*, consequently enhancing the peroxidase activity of the MNPs. Considering their low cost, easy separation, and stable activity, MNPs could be applied to various detection systems.

1. Introduction

Food-poisoning bacteria have been a serious threat to human health for the past years. *Salmonella* especially is one of the major pathogens causing intestinal infection. They can spread from poultry, eggs, and vegetables to humans or livestock during handling and distribution [1]. The consumption of food contaminated with bacteria can lead to immune deficiencies and other symptoms such as fever, diarrhea, and even death within 12 to 72 hours. Lately, great attention about well-being food becomes a cause for increasing infection to human bodies, leading to medical costs and mass recall in the food industry. According to the Center for Disease Control and Prevention (CDC), infection by *Salmonella* has been growing every year, and value is estimated to be about 19,000 hospitalizations and 380 deaths [2, 3]. Thus, the whole world has demanded a fast and simple detection method before people consume the contaminated food.

Common procedures for the detection of food-poisoning bacteria involve culture methods and polymerase chain reaction (PCR) followed by gel electrophoretic analysis [4, 5]. However, PCR-based methods require tedious experimental procedures and long analysis times, which cannot prevent distribution among food markets. Recently, colorimetric methods for the detection of bacteria, employing noble metal nanoparticles such as gold and TiO₂, have become popular [6–9]. For example, the aggregation of gold nanoparticles (AuNPs) results in a shift in the absorption spectrum and a color change from red to purple. Furthermore, nanomaterials conjugated with antibodies have a unique possibility in detecting bacteria or other molecules. Nevertheless, these methods have several limitations that depend on experimental conditions (e.g., salt concentration, pH, and temperature) and are subjected to complicated steps during the preparation and conjugation of antibodies on the nanoparticles [10]. In addition, fluorescence-based assays

based on natural enzymes like horseradish peroxidase have been studied. However, enzymes as biological catalysts can be easily digested and denatured [11].

To overcome such challenges, aptamers and magnetic nanoparticles (MNPs) have been provided a substitute choice to meet the requirements. Aptamers are oligonucleotides by SELEX (systematic evolution of ligands by exponential enrichment). Created aptamers can specifically bind to target molecule forming a unique structure similar with antibodies. Furthermore, owing to inexpensive and stable features in various experimental conditions, aptamers are useful in biotechnology [12, 13]. In this study, aptamers that interact with outer membrane protein on the surface of *S. typhimurium* were used [14, 15]. As another well-known materials, MNPs exhibit catalytic stability, ease to separation, and chemical inertness. In this system, MNPs promote the oxidation of 3,3',5,5'-tetramethylbenzidine (TMB) as a colorimetric substrate by peroxidase-like activity within several minutes in the presence of H_2O_2 [16, 17]. Nonetheless, mechanism of enzyme-like activity is not known exactly. Once H_2O_2 molecules are adsorbed onto the surface of MNPs, Fe^{2+} and Fe^{3+} in the MNPs catalyze the disassembly of H_2O_2 to radicals like $\cdot OH$ and $O_2^{\cdot -}/HO_2^{\cdot}$ [18]. Because of the high oxidizing ability of radical, it mediates oxidation of TMB. This reaction produces a blue-colored product, which enables colorimetric detection with naked eyes. Herein, the purpose of colorimetric method using MNPs and DNA aptamers is the prior detection of contaminated food before its distribution among market places. Furthermore, the development of methods for a fast and stable detection of bacteria is of great significance in avoiding and controlling *Salmonella* pathogens.

2. Experimental Details

2.1. Materials. $FeCl_2 \cdot 4H_2O$ (iron(II) chloride tetrahydrate), $FeCl_3 \cdot 6H_2O$ (iron(III) chloride hexahydrate), NaOH (sodium hydroxide), DMSO (dimethyl sulfoxide), Acetate buffer, and TMB were purchased from Sigma-Aldrich (St. Louis, MO). H_2O_2 (hydrogen peroxide) was obtained from Junsei (Tokyo, Japan) and ethanol was purchased from Samchun Chemical (Pyeongtaek, Korea). DNA aptamers with or without fluorophores (oligomer: 5'-GAGGAAAGTCTA-TAGCAGAGGAGATGTGTGAACCGAGTAA-3') were synthesized by Macrogen (Seoul, Korea) with MOPC purification method [14, 15]. Luria-Bertani (LB) broth and agar media were obtained from LPS solution (Daejeon, Korea). All experiments were conducted with ultrapure deionized (DI) water using a Milli-Q water purifier from Merck Millipore (Billerica, MA).

2.2. Synthesis of Fe_3O_4 Magnetic Nanoparticles (MNPs). MNPs were synthesized by a simple and convenient method using precipitation and ultrasonication. $FeCl^{2+}$ (0.25 M) and $FeCl^{3+}$ (0.25 M) ($Fe^{3+}/Fe^{2+} = 2$) were added to 50 mL of ultrapure DI water. Then, a 1 M NaOH solution was added dropwise until the pH reached 10.0. The color of the ferrous and ferric solution changed from bright brown to black. The solution was sonicated at a frequency of 40 kHz and

an ultrasonic power of 100 W at 80°C. After the reaction for 35 min, the resulting black MNPs were collected by neodymium magnetic separation and washed with water and ethanol several times. The final suspension was dried overnight in a vacuum oven at 60°C.

2.3. Characterizations. Field-emission transmission electron microscopy (FE-TEM, 200 kV) (JEM-2100F, Jeol, Japan) and X-ray diffractometry (XRD, NEW D8-Advance, Bruker-AXS, Madison, WI) were used to analyze the morphology and structural features of the synthesized MNPs. The potential of the MNPs was obtained by measuring the zeta potential (ELSZ-1000, Otsuka, Japan) to determine the capture efficiency. A multimode microplate reader (Synergy H1, BioTek, Winooski, VT) was used at all experimental steps.

2.4. MNP-Based Colorimetric Assay with TMB. TMB is used as a typical chromogenic substrate and can act as a donor of hydrogen for reduction of H_2O_2 by peroxidase. In common with enzyme, the resulting change of colors could verify the catalytic activity of the MNPs. To prepare well-dispersed solutions, MNPs in ultrapure DI water (1 mg/mL) were placed in the sonicator bath for 30 min. The white TMB powder (0.5 μM) was dissolved in DMSO, and the solution was diluted in ultrapure water. MNPs were diluted in 0.1 M acetate buffer (pH 4.0) and incubated with TMB and H_2O_2 for 10 min at 42°C. After the reaction, the mixture was immediately separated using an external magnet for 30 s. The supernatant was used to obtain the absorbance intensity at 650 nm.

2.5. Microorganism and Culture Conditions. To validate the colorimetric detection system, we used *S. typhimurium* ATCC 14028. Bacteria were grown in LB broth at 37°C with gentle shaking at 200 rpm. Furthermore, we carried out visible plate counting using agar plates after incubation for 24 h at 37°C. Finally, we determined that the number of *S. typhimurium* ATCC 14028 was 3.75×10^8 CFU/mL at an optical density (OD) of 1.0. In the experiment, the cultured bacteria (1 mL) were centrifuged at 13,000 rpm for 1 min at an OD of 1.0, and the pellet was then diluted in ultrapure DI water before the experimental step.

3. Results and Discussion

3.1. Preparation and Characterization of MNPs. MNPs were prepared by the coprecipitation method with sonication. After introducing sonochemistry, the peroxidase-like activities of Fe_3O_4 MNPs increased and resulted in small spherical particles that were below 20 nm in diameter (Figures 1(a) and 1(b)). The decrease in particle size was necessary to improve the peroxidase-like activities of MNPs [19]. To further identify characteristic features, MNPs were examined using XRD (Figure 1(c)). As a result, all peaks corresponded to Fe_3O_4 (JCPDF card number 00-024-0081).

3.2. Colorimetric Detection Method Using the Peroxidase-Like Activities of MNPs. The basic principle of colorimetric detection is shown in Figure 2. In the procedure, the MNPs

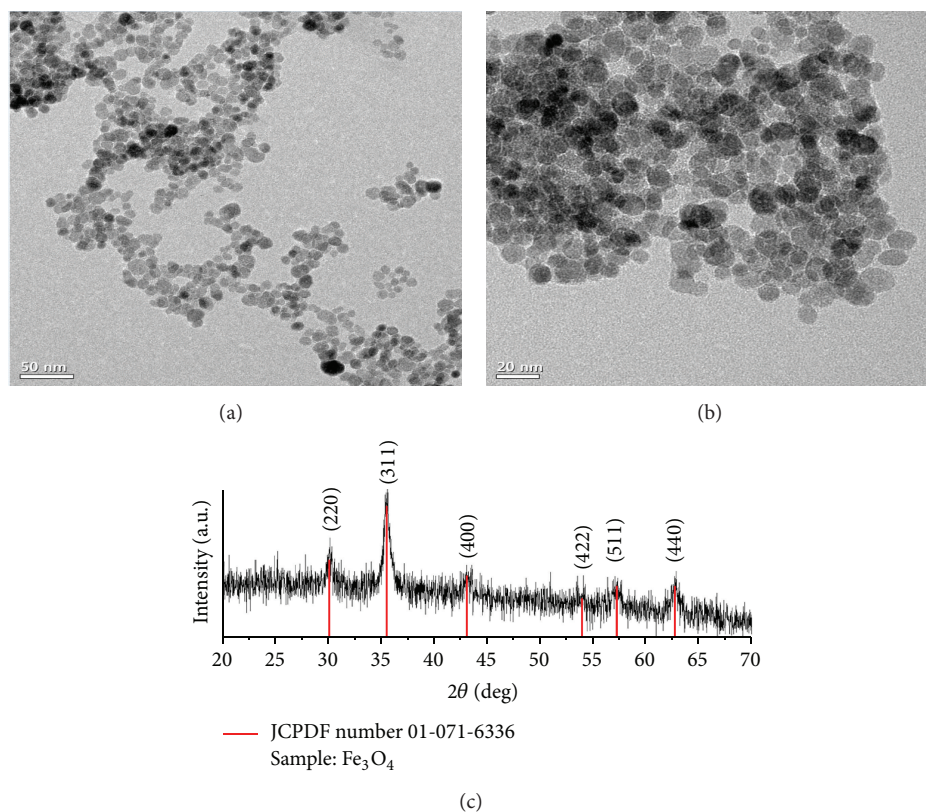


FIGURE 1: TEM images and XRD data of MNPs. Scale bars are 50 nm (a) and 20 nm (b). XRD patterns (c) indicate that the synthesized MNPs were Fe₃O₄ based on JCPDF data.

catalyzed the peroxidase-mediated colorimetric reactions in the solution containing TMB and H₂O₂ (control), generating colored products. The supernatant was separated by external magnetic for measuring the intensity of absorbance by UV-vis spectroscopy, and a color change could easily be seen by the naked eyes. On the other hand, when the MNPs were first incubated with DNA aptamers, blocking the surface of MNPs reduces enzyme-like activity. It is believed that the DNA aptamers rapidly adsorbed onto the surface of the MNPs because of electrostatic interactions between the positively charged surface of the MNPs and the negatively charged phosphate backbone of the DNA aptamers. It is evidenced that contact of TMB with the surface of the MNPs is vital for promoting the oxidation of TMB with H₂O₂. Moreover, DNA aptamers also caused the aggregation of MNPs, considerably reducing the ability of the surfaces and decreasing the colorimetric property. Finally, when *Salmonella* was present in the solution mixed with MNPs and DNA aptamers, the specific DNA aptamers were detached from the MNPs by their strong interaction with *S. typhimurium*. In this step, MNPs recover the peroxidase activity by reexposing the surface to reagents and then produce the blue-colored products again. Consequently, the exposure of MNPs enhanced their activities compared with those in solution containing MNPs and DNA aptamers.

3.3. Effect of Conditions on Catalytic Properties of MNPs. Before starting the experiment, we assessed the catalytic

activity of each component in the system. Where MNPs were present with TMB and H₂O₂, a colorimetric response was observed with a high absorption peak at 650 nm compared with the other samples (red solid line in Figure 3). On the other hand, significantly reduced or no signals were generated when H₂O₂ (blue solid line), TMB (blue dashed line), or MNPs (black dashed line) were excluded. These results indicated that the catalytic activity of MNPs was induced when TMB and H₂O₂ were mixed together. Importantly, no colorimetric signal was observed in the DNA@TMB@H₂O₂ sample (red dash line), showing that the DNA aptamers did not contribute to the oxidation of TMB.

The absorption of DNA aptamers on the surface of the MNPs contributed to colorimetric assay, and this phenomenon led to the inhibition of the peroxidase-mimicking activity. We first evaluated the charge of the MNP surface using zeta potential analysis in order to explore the absorption property of MNPs with or without DNA aptamers. Thus, we confirmed the change in charge on the surface of the MNPs after introducing the DNA aptamers. The potential of pristine MNPs was positive (+16.89), but it turned into a negative value (−27.18) with the presence of DNA aptamers, as shown in Figure 4(a). This result showed that the negatively charged DNA aptamers immediately reacted with the positively charged surface of the MNPs via electrostatic interactions. To further validate the interaction, the amount of DNA aptamers adsorbed onto the MNPs was calculated by measuring the relative fluorescence units (RFU).

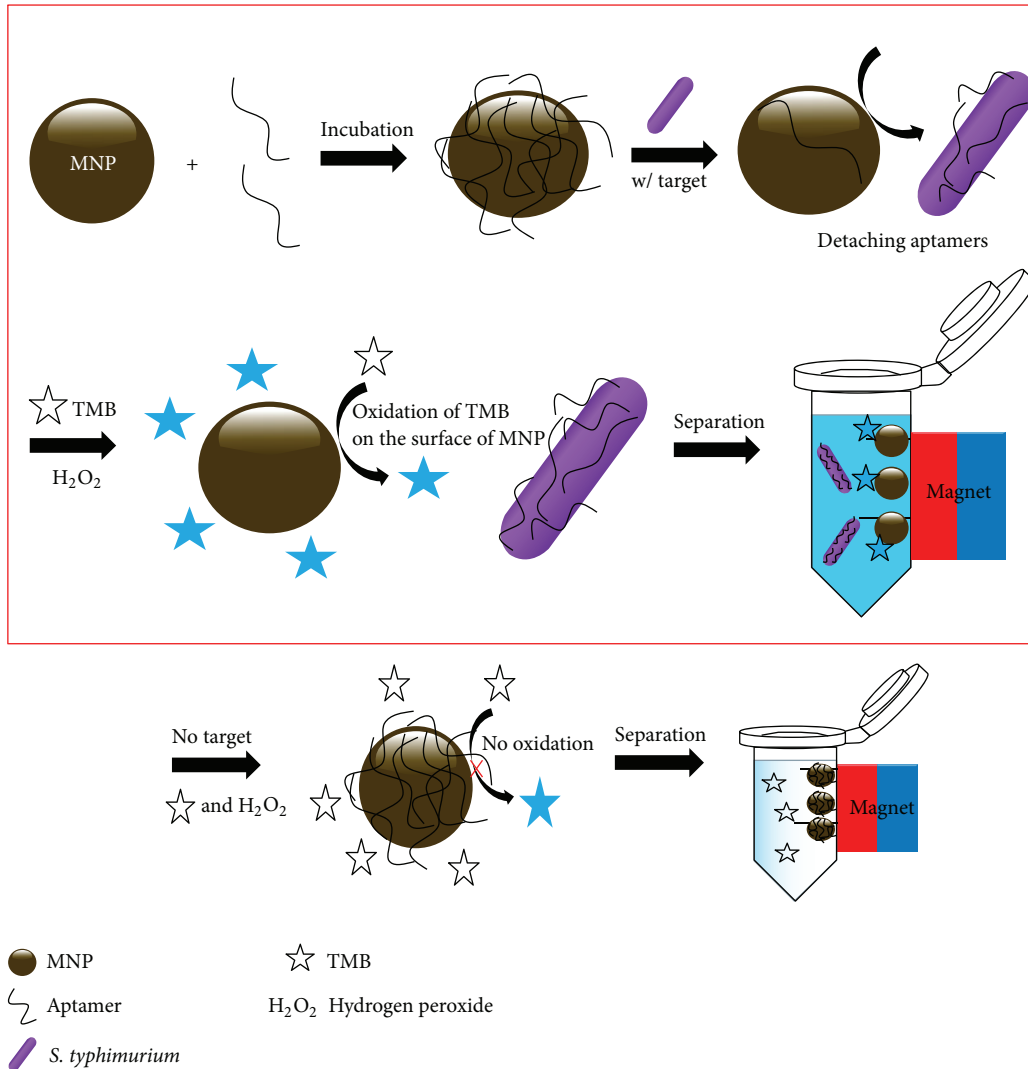


FIGURE 2: Schematic illustration of the MNP-based colorimetric detection using label-free DNA aptamers and TMB.

The aptamers (100 $\mu\text{mol/mL}$), which were combined with carboxyfluorescein (FAM), were incubated with pristine MNPs (500 $\mu\text{g/mL}$) and unbound DNA aptamers were separated in the supernatant. The amount of unbound FAM-aptamers was estimated by measuring the fluorescence. The fluorescent analysis of the supernatant following the separation clearly showed a direct interaction of approximately 58% occurrence between the DNA aptamers and the surface of the MNPs, as shown in Figure 4(b). It is approximately estimated that 0.116 μmol of DNA aptamers has interacted with 1 μg of MNPs. In the same manner, the inhibition of the peroxidase activities of MNPs caused by DNA aptamers (100 $\mu\text{mol/mL}$) was studied by observing the concentration of MNPs in Figure 5. After 15 min of incubation with or without DNA aptamers, the MNP solutions were separated by an external magnet. The intensity of the supernatant was measured by UV-vis spectroscopy. The degree of reduction was decided to be approximately 81% (red solid line and dashed line), 65% (blue solid line and dashed line), and 36% (black solid

line and dashed line), respectively (Figure 5(b)). As a result, considerable signal reduction was generated from the sample containing 500 $\mu\text{g/mL}$ of MNPs. Importantly, the differences in the color and intensity of absorbance could be distinguished easily. If a low volume of MNPs was added to the DNA aptamers, the shielding of MNPs could be improved by the absorption of the aptamers onto the surface of MNPs. However, a decline in MNP concentration would decrease the capture efficiency. This means that the shielding effect of MNPs exhibited differences in ability at various concentrations as a result of steric hindrance and competitive reaction. Additionally, we determined the optimal conditions of this detection system, as shown in Figure 6. After performing buffer tests using Tris-HCl, HEPES, PBS, and acetate buffer in various pH conditions (data not shown), we found that acetate buffer at pH 4.0 was a suitable buffer solution for this system (Figure 6(a)). The significant signal from the oxidation of TMB was correlated with the concentration of MNPs. A concentration that is either too high or too low

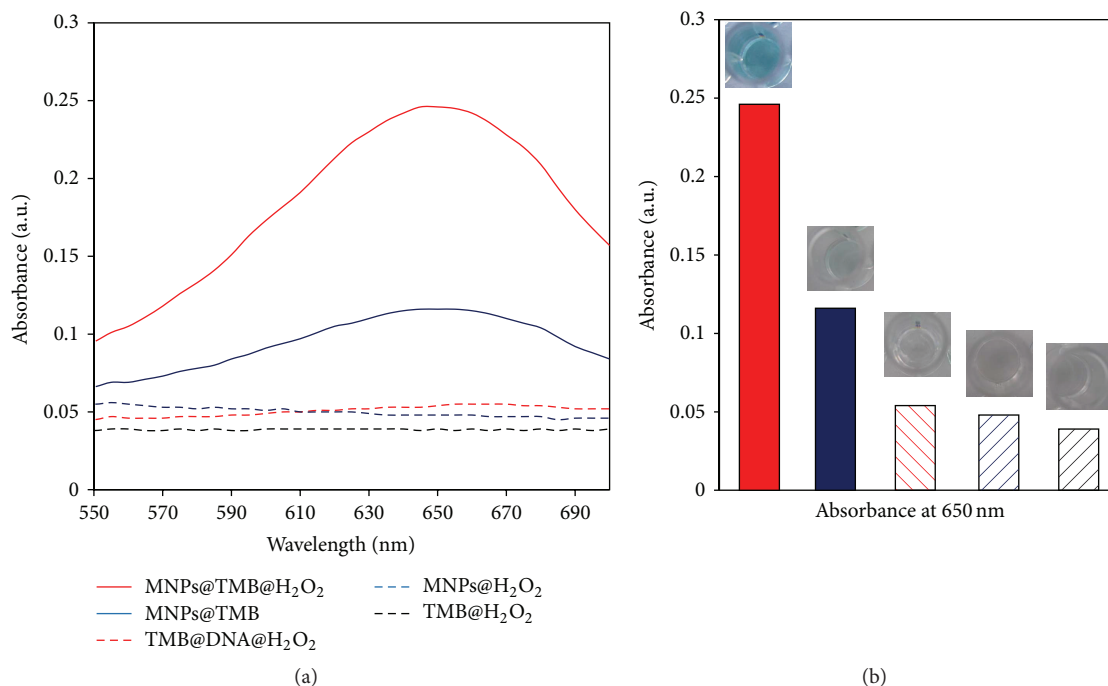


FIGURE 3: UV-vis absorption spectra (a) and bar graph at 650 nm (b). The effect of each reagent was tested in the colorimetric system. MNPs@TMB@H₂O₂: red solid line, MNPs@TMB: blue solid line, MNPs@DNA@H₂O₂: red dashed line, MNPs@H₂O₂: blue dashed line, and TMB@H₂O₂: black dash line. The insets in (b) represent images of the well plates for the different colors in the five cases.

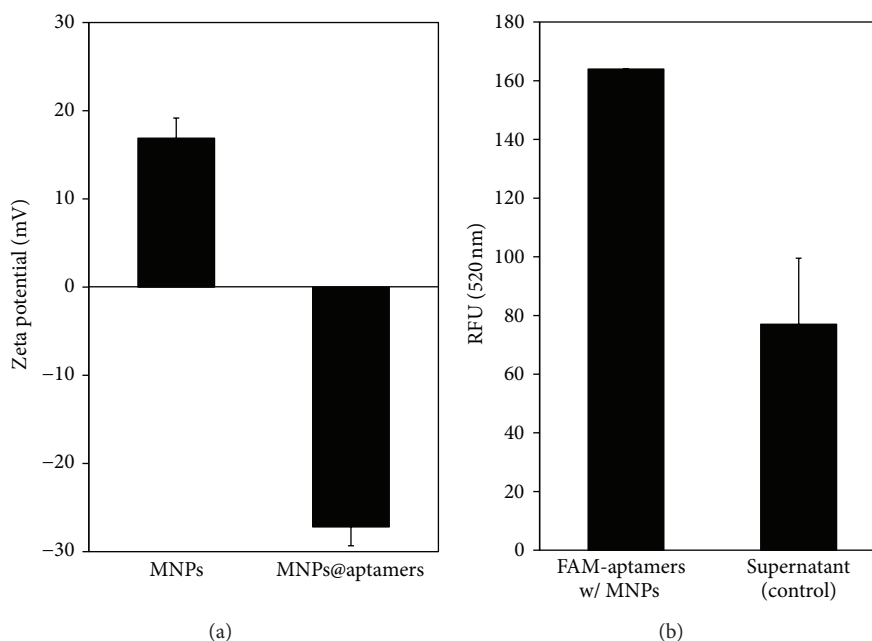


FIGURE 4: Absorption of DNA aptamers onto the MNPs confirmed by zeta potential (a) and relative fluorescence units (RFU) using FAM-aptamers (b).

would lead to a weak intensity in the UV-vis spectrum. We confirmed that the best MNP concentration was 400 $\mu\text{g}/\text{mL}$ (Figure 6(b)). In order to determine the effect of TMB on the generation of blue color, 400 $\mu\text{g}/\text{mL}$ of MNPs has reacted with various concentrations of TMB (Figure 6(c)) and H₂O₂ (Figure 6(d)). The concentrations of TMB and H₂O₂ chosen

in this study were 40 μM and 35 mM, respectively. Finally, the solution was incubated for 10 min (Figure 6(e)).

3.4. Detection of *S. typhimurium* Cells. As shown in Figure 7, *Salmonella* cells were used for the detection experiments. The solution containing the DNA aptamers (black solid

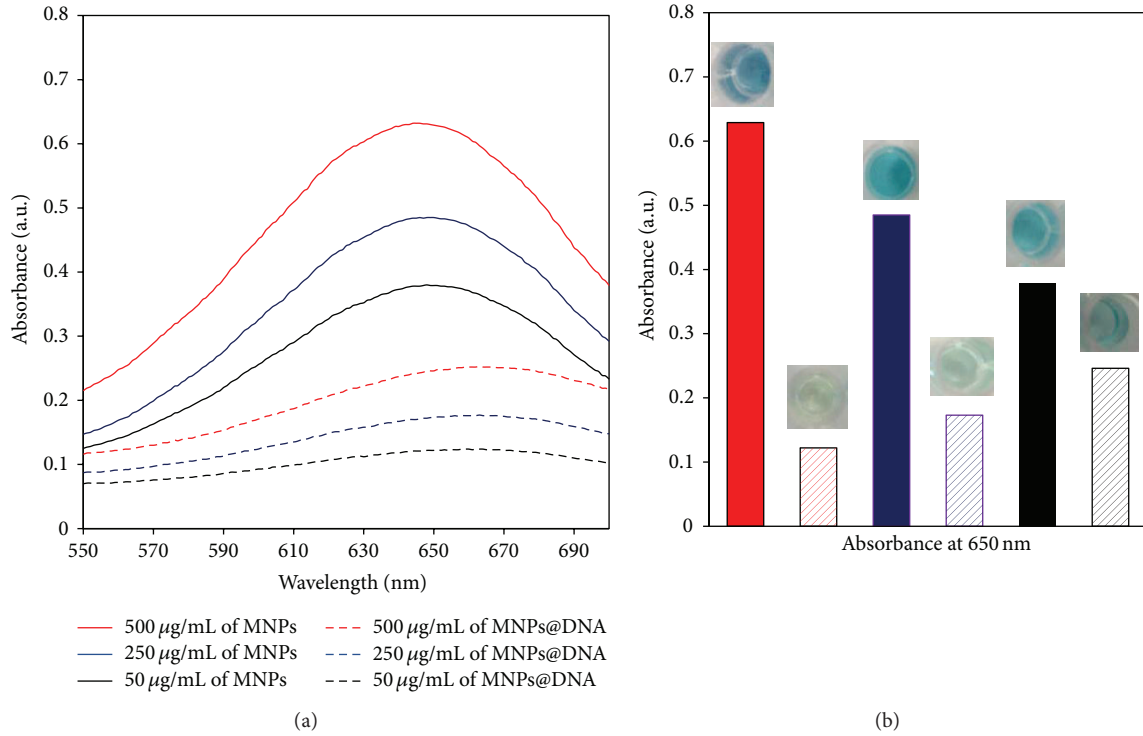


FIGURE 5: UV-vis absorption spectra (a) and bar graph at 650 nm (b) obtained from solutions containing different concentrations of MNPs with DNA aptamers. The insets in (b) represent images of the well plates for the different cases, with or without DNA aptamers.

TABLE I: Comparison of different methods for detection of *Salmonella*.

Nanomaterial	Method	Linear range	LOD	Reference
MNP antibody	Selective filtration	$2 \times 10^1 - 2 \times 10^4$ cells	2×10^1 cells	[10]
MNP antibody	Fluorescence spectrometry	$10^1 - 10^7$ CFU/mL	10 CFU/mL	[11]
MNP antibody TiO ₂ antibody	Absorption spectroscopy	$10^2 - 10^8$ CFU/mL	100 CFU/mL	[8]
MNP antibody	PCR	$10^1 - 10^7$ CFU/mL	10^3 CFU/mL	[5]

line) displayed a significant reduction in color response compared with the control (red solid line) owing to the shielding effect. To demonstrate the capability of the colorimetric system, *Salmonella* (7.5×10^5 CFU/mL) was added to the MNPs@DNA aptamers solution. Immediately, DNA aptamers were detached from the surface of the MNPs because of their strong affinity to *Salmonella*, which led to the reexposure of the MNP surface to TMB. Finally, the intensity of absorbance and color response were regained in comparison with a sample containing DNA aptamers only. Table 1 summarizes the detection of *Salmonella* using various methods. It is presented that our proposed method has no outstanding performance compared to other spectrophotometric or fluorometry methods in the lower detection limit. However, most of the assays introduce antibodies and other nanomaterials. Detection method based on the peroxidase-like activity of MNP and DNA aptamer does not exist. Thus, this study is very meaningful as a proof-of-concept (POC) experiment for the colorimetric detection of pathogen. Much

remains to be done with enhancement of sensitivity at further improvement.

4. Conclusion

In summary, a simple and rapid colorimetric system based on MNPs and DNA aptamers was developed for the detection of *S. typhimurium*, which relies on increasing signal from the peroxidase-like activities of MNPs. The developed colorimetric system required a short assay time of only 10 min, and results could be verified with the naked eyes. Furthermore, MNPs and DNA aptamers did not require surface modification. The method was cost-effective and simple, unlike biosensors based on antibodies or fluorophores. After optimization, the system was able to visibly detect bacteria up to 7.5×10^5 CFU/mL in buffer solution. Compared with antibody-immobilized MNPs that have been reported, the sensitivity of this colorimetric system was efficient.

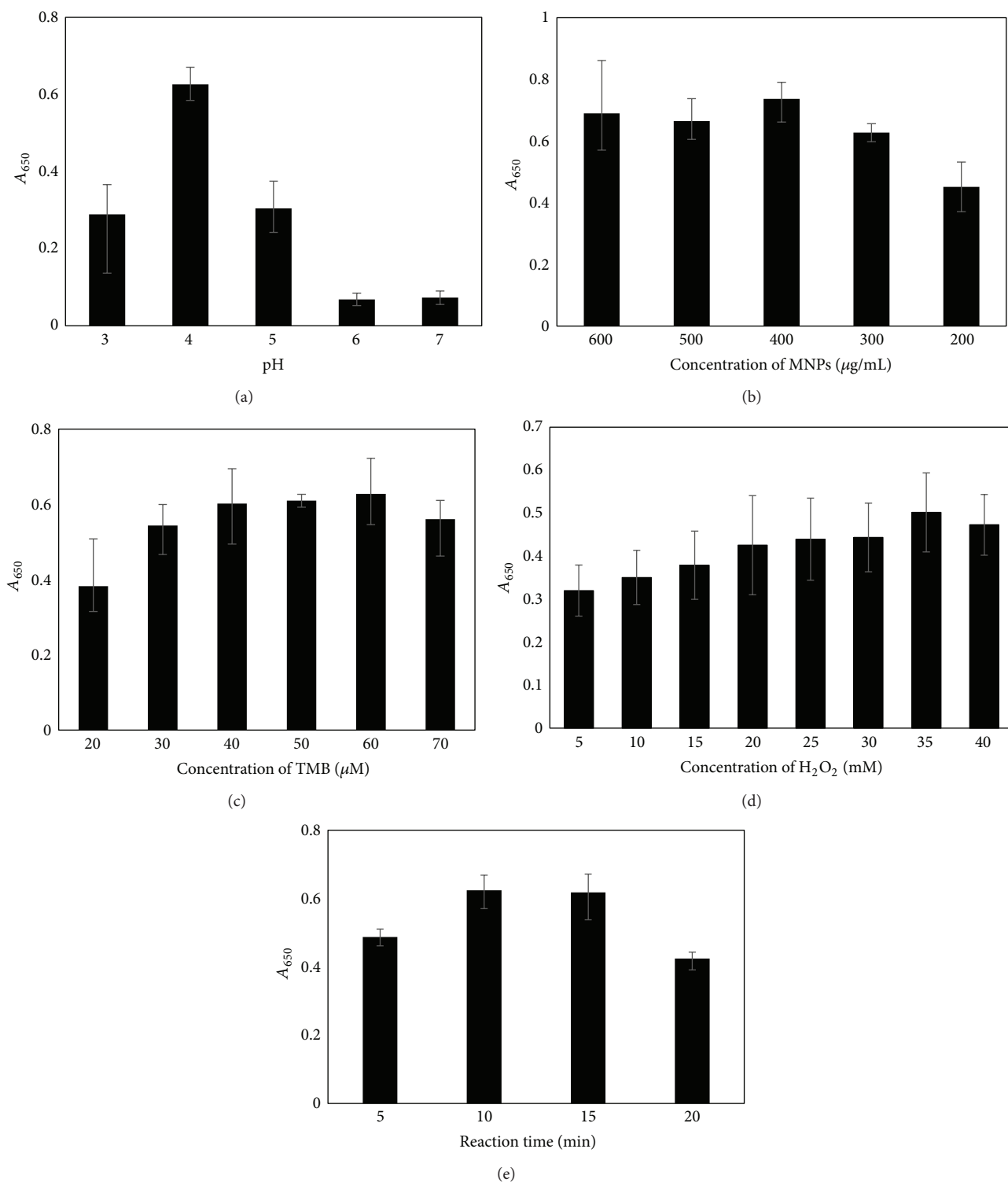


FIGURE 6: Optimization of parameters for the colorimetric system. Acetate buffer at pH 4.0 was optimal for TMB oxidation (a). MNP concentration of 400 $\mu\text{g/mL}$ (b), TMB concentration of 40 μM (c), H_2O_2 concentration of 35 mM (d), and incubation time of 10 min (e) yielded optimal effectiveness.

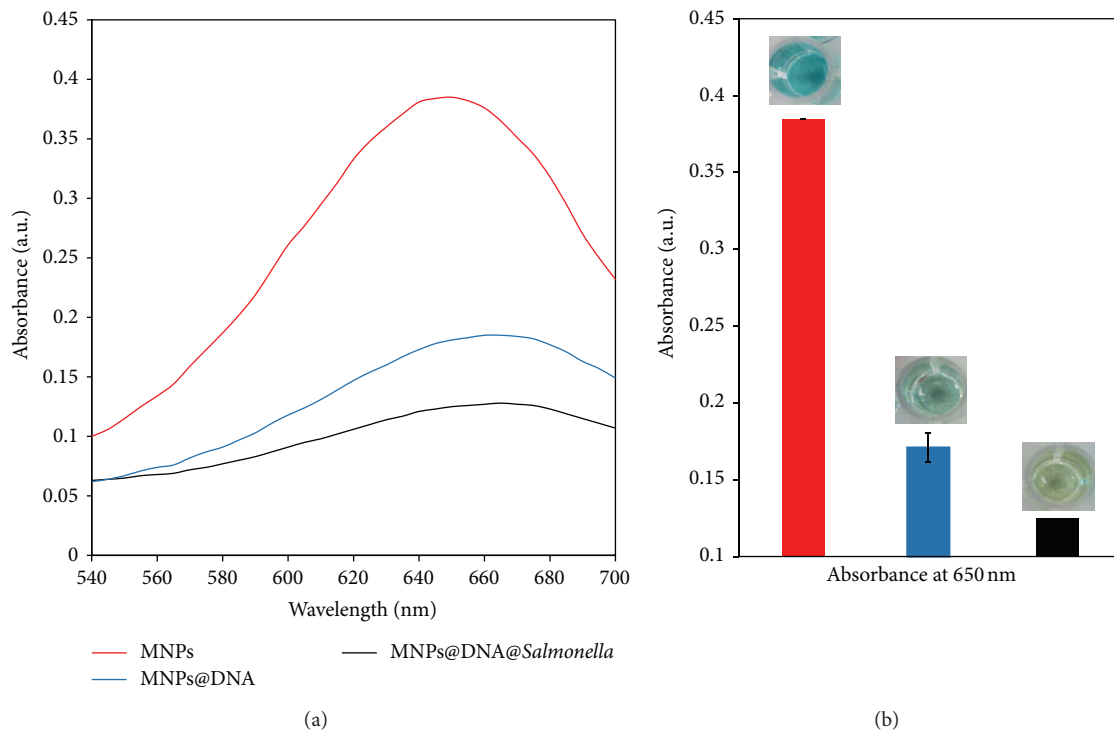


FIGURE 7: UV-vis absorption spectra (a) and bar graph at 650 nm (b). The insets in (b) represent images of the well plates for the colorimetric detection of *Salmonella* sp.

The advantage of the new system reveals its great potential application as a point-of-care testing sensor. Thus, we are still investigating the development of MNPs to enhance the detection limit and to extend the cross-reactivity to other bacteria.

Conflict of Interests

The authors declare that they have no competing interests.

Acknowledgments

This work was supported by the IT R&D program of MoTIE/MISP/KEIT (10044580, Korea) and the Chung-Ang University Excellent Student Scholarship Grants in 2013–2015.

References

- [1] J. R. Glisson, "Bacterial respiratory diseases of poultry," *Poultry Science*, vol. 77, no. 8, pp. 1139–1142, 1998.
- [2] D. C. Rodrigue, R. V. Tauxe, and B. Rowe, "International increase in *Salmonella enteritidis*: a new pandemic?" *Epidemiology and Infection*, vol. 105, no. 1, pp. 21–27, 1990.
- [3] E. Scallan, R. M. Hoekstra, F. J. Angulo et al., "Foodborne illness acquired in the United States—Major pathogens," *Emerging Infectious Diseases*, vol. 17, no. 1, pp. 7–15, 2011.
- [4] S. D. Oliveira, L. R. Santos, D. M. T. Schuch, A. B. Silva, C. T. P. Salle, and C. W. Canal, "Detection and identification of salmonellas from poultry-related samples by PCR," *Veterinary Microbiology*, vol. 87, no. 1, pp. 23–35, 2002.
- [5] P. Bakthavathsalam, V. K. Rajendran, U. Saran, S. Chatterjee, and B. M. Jaffar Ali, "Immunomagnetic nanoparticle based quantitative PCR for rapid detection of *Salmonella*," *Microchimica Acta*, vol. 180, no. 13–14, pp. 1241–1248, 2013.
- [6] Y. Yuan, J. Zhang, H. Zhang, and X. Yang, "Label-free colorimetric immunoassay for the simple and sensitive detection of neurogenin3 using gold nanoparticles," *Biosensors and Bioelectronics*, vol. 26, no. 10, pp. 4245–4248, 2011.
- [7] J. Joo, C. Yim, D. Kwon et al., "A facile and sensitive detection of pathogenic bacteria using magnetic nanoparticles and optical nanocrystal probes," *Analyst*, vol. 137, no. 16, pp. 3609–3612, 2012.
- [8] C. M. Niemeyer, "Nanoparticles, proteins, and nucleic acids: biotechnology meets materials science," *Angewandte Chemie International Edition*, vol. 40, no. 22, pp. 4128–4158, 2001.
- [9] N. Duan, S. Wu, C. Zhu et al., "Dual-color upconversion fluorescence and aptamer-functionalized magnetic nanoparticles-based bioassay for the simultaneous detection of *Salmonella typhimurium* and *Staphylococcus aureus*," *Analytica Chimica Acta*, vol. 723, pp. 1–6, 2012.
- [10] W.-B. Shim, J.-E. Song, H. Mun, D.-H. Chung, and M.-G. Kim, "Rapid colorimetric detection of *Salmonella typhimurium* using a selective filtration technique combined with antibody-magnetic nanoparticle nanocomposites," *Analytical and Bioanalytical Chemistry*, vol. 406, no. 3, pp. 859–866, 2014.
- [11] Z. Zhang, Y. Liu, C. Zhang, and W. Luan, "Horseradich peroxidase and peroxidase and antibody labeled gold nanoparticle probe for amplified immunoassay of ciguatoxin in fish samples

- based on capillary electrophoresis with electrochemical detection,” *Toxicon*, vol. 96, no. 15, pp. 89–95, 2015.
- [12] S. D. Jayasena, “Aptamers: an emerging class of molecules that rival antibodies in diagnostics,” *Clinical Chemistry*, vol. 45, no. 9, pp. 1628–1650, 1999.
- [13] B. Book, J. Chen, and J. Irudayaraj, “Quantification of receptor targeting aptamer binding characteristics using single-molecule spectroscopy,” *Biotechnology and Bioengineering*, vol. 108, no. 5, pp. 1222–1227, 2011.
- [14] R. Joshi, H. Janagama, H. P. Dwivedi et al., “Selection, characterization, and application of DNA aptamers for the capture and detection of *Salmonella enterica* serovars,” *Molecular and Cellular Probes*, vol. 23, no. 1, pp. 20–28, 2009.
- [15] G. Singh, P. Vajpayee, N. Rani, A. Jyoti, K. C. Gupta, and R. Shanker, “Bio-capture of *S. Typhimurium* from surface water by aptamer for culture-free quantification,” *Ecotoxicology and Environmental Safety*, vol. 78, no. 1, pp. 320–326, 2012.
- [16] K. S. Park, M. I. Kim, D.-Y. Cho, and H. G. Park, “Label-free colorimetric detection of nucleic acids based on target-induced shielding against the peroxidase-mimicking activity of magnetic nanoparticles,” *Small*, vol. 7, no. 11, pp. 1521–1525, 2011.
- [17] M.-A. Woo, M. I. Kim, J. H. Jung, K. S. Park, T. S. Seo, and H. G. Park, “A novel colorimetric immunoassay utilizing the peroxidase mimicking activity of magnetic nanoparticles,” *International Journal of Molecular Sciences*, vol. 14, no. 5, pp. 9999–10014, 2013.
- [18] L. Gao, J. Zhuang, L. Nie et al., “Intrinsic peroxidase-like activity of ferromagnetic nanoparticles,” *Nature Nanotechnology*, vol. 2, no. 9, pp. 577–583, 2007.
- [19] N. Wang, L. Zhu, D. Wang, M. Wang, Z. Lin, and H. Tang, “Sono-assisted preparation of highly-efficient peroxidase-like Fe_3O_4 magnetic nanoparticles for catalytic removal of organic pollutants with H_2O_2 ,” *Ultrasonics Sonochemistry*, vol. 17, no. 3, pp. 526–533, 2010.

Research Article

Density Functional Investigation of Graphene Doped with Amine-Based Organic Molecules

Yeun Hee Hwang,¹ Hyang Sook Chun,² Kang Min Ok,¹
Kyung-Koo Lee,³ and Kyungwon Kwak¹

¹Department of Chemistry, Chung-Ang University, 221 Heukseok-dong, Dongjak-gu, Seoul 156-756, Republic of Korea

²School of Food Science and Technology, Chung-Ang University, Ansong, Gyeonggi 456-756, Republic of Korea

³Department of Chemistry, Kunsan National University, Gunsan, Jeollabuk-do 573-701, Republic of Korea

Correspondence should be addressed to Kyung-Koo Lee; kklee@kunsan.ac.kr and Kyungwon Kwak; kkwak@cau.ac.kr

Received 7 June 2015; Accepted 2 July 2015

Academic Editor: Jin W. Seo

Copyright © 2015 Yeun Hee Hwang et al. This is an open access article distributed under the Creative Commons Attribution License, which permits unrestricted use, distribution, and reproduction in any medium, provided the original work is properly cited.

To improve the electronic properties of graphene, many doping techniques have been studied. Herein, we investigate the electronic and molecular structure of doped graphene using density functional theory, and we report the effects of amine-based benzene dopants adsorbed on graphene. Density functional theory (DFT) calculations were performed to determine the role of amine-based aromatic compounds in graphene doping. These organic molecules bind to graphene through long-range interactions such as π - π interactions and C-H $\cdots\pi$ hydrogen bonding. We compared the electronic structures of pristine graphene and doped graphene to understand the electronic structure of doped graphene at the molecular level. Also, work functions of doped graphene were obtained from electrostatic potential calculations. A decrease in the work function was observed when the amine-based organic compounds were adsorbed onto graphene. Because these systems are based on physisorption, there was no obvious band structure change at point *K* at the Fermi level after doping. However, the amine-based organic dopants did change the absolute Fermi energy levels. In this study, we showed that the Fermi levels of the doped graphene were affected by the HOMO energy level of the dopants and by the intermolecular charge transfer between the adsorbed molecules and graphene.

1. Introduction

Graphene, a two-dimensional hexagonal lattice of carbon, has recently attracted much interest as a flexible and transparent conductive electrode due to its high conductivity [1–3] and low optical absorption [3–5]. By controlling the graphene work function, the conductivity can be improved through reducing the contact barriers between graphene and an electrode device [6]. The conductivity can be tuned by doping techniques such as substitution doping [7], chemical doping [8], and spontaneous surface charge transfer between adsorbed materials and carbon atoms [9]. Previous studies have shown that derivatives of benzene can bind to graphene sheets because of the formation of strong π - π interactions between the aromatic ring and the extended π -system of graphene. Also, the degree of doping of graphene can be adjusted by modulating the electron-donating abilities of the benzene derivatives by adding electron-donating or

electron-withdrawing group substituents. Electron-donating groups increase the electron density on aromatic molecules; thus, they lead to n-type doping of graphene. For example, 1,5-naphthalenediamine is an aromatic molecule with an electron-donating amine functional group (-NH₂). In contrast, aromatic molecules with electron-withdrawing groups, for example, tetrasodium 1,3,6,8-pyrenetetrasulfonic acid (TPA), cause p-type doping of graphene because these substituents decrease the electron density on the aromatic ring system of the organic dopant [10]. In addition, amine-based organic compounds are known to be efficient n-type dopants because amine (-NH₂) functional groups have lone pairs, which can donate electrons to the graphene sheet [11, 12]. Density functional theory (DFT) calculations can be used to obtain detailed information about the bond types and electronic structure of doped graphene, enabling the examination and analysis of these systems [13]. Recently, DFT calculations were used to show that both pristine graphene

and Al-doped graphene are potential candidates for the detection of the toxic compound acrolein (C_3H_4O) [14].

In this study, we used amine-based benzene derivatives to investigate the effect of amine-based organic molecules on the electronic and molecular structure of graphene. The properties of the organic molecules were modulated by the addition of functional groups such as phenyl rings (**1**), butylphenyl groups (**2**), and acetylphenyl groups (**3**). To investigate the role of amine derivatives in graphene doping, we carried out DFT calculations. Geometry optimizations were used to find stable equilibrium geometries, and electrostatic potential calculations were performed to obtain the work functions of both pristine graphene sheet and graphene doped with amine-based dopants. In addition, the electronic structure of pristine graphene and that of doped graphene were compared to understand and improve the performance of graphene-based electrode devices at the molecular level.

2. Computational Methods

2.1. Geometry Optimization. All DFT calculations were performed with the DMol³ software package [15] to study the interactions between graphene and the amine-based organic molecules and to predict the electronic structure change of graphene when the organic molecules are physisorbed onto graphene. To mimic the extended structure, we used a periodic boundary condition (PBC). This was used for both the pristine graphene sheet and the adsorbed graphene complex. All calculations employed the DNP (double numerical with d and p polarization) basis set, which is comparable to a 6-31G(d,p) Gaussian-type basis set. Geometry optimization calculations used a generalized gradient approximation (GGA) functional that includes exchange-correlation, that is, the Perdew-Burke-Ernzerhof (PBE) functional [16, 17]. PBE-GGA calculations are known to perform well in the description of long-range interactions compared to the local density approximation (LDA) [18]. To describe more accurately the dispersive interactions between graphene and the adsorbed organic compounds, the Tkatchenko-Scheffler (TS) method [19] was employed for dispersion correction. TS is a parameter-free method for the accurate determination of long-range interactions in self-consistent field (SCF) electronic structure calculations. The geometry optimization procedure was performed without any symmetry restrictions. The criteria for both the SCF convergence and the total energy were set to 10^{-6} Hartree. The maximum force was converged to 0.002 Hartree per Å, and the maximum displacement parameter was set to 0.005 Å. To improve convergence, thermal smearing was used and was set to 0.005 Hartree. To calculate the work function of graphene, the layers were separated by a 20 Å vacuum to minimize interactions between adjacent layers. We used an $8 \times 8 \times 1$ graphene supercell consisting of 128 C atoms.

2.2. Electrostatic Potential Calculations. Electrostatic potential calculations, provided by the DMol³ package, were performed on the periodic structures to obtain the work functions of the pristine graphene sheet and of the graphene

doped with amine-based organic dopants. The average potential was calculated along the c -direction, which is perpendicular to the graphene surface. The work function (W) was determined using the following equation: $W = V_{\text{vacuum}} - E_F$, where V_{vacuum} is the potential in the vacuum, which is calculated as the average potential between two graphene layers. At large separation from the graphene sheet, the calculated electrostatic potential becomes almost independent of the separation. The calculated electrostatic potential at this distance is defined as V_{vacuum} . E_F is the Fermi energy relative to the mean electrostatic potential energy in the graphene layer, and this energy is obtained directly from the electronic state output file generated by DMol³. The work function measures the minimum energy required to separate an electron far from the surface of the graphene and is distinct from the ionization potential because the removed electron is still macroscopically close to the surface and is affected by it. Thus, the vacuum potential is determined as the point at which the calculated average potential becomes flat as distance along the c -axis increases; that is, it is the potential at separation from the surface at which the effect on the electron of the surface is at a minimum.

3. Results and Discussion

3.1. Molecular Structure Change. DFT geometry optimizations were carried out on both extended pristine graphene (PG) and adsorbed graphene sheets. At first, PBE/DNP calculations with the TS dispersion correction were performed for each organic molecule and for pristine graphene to find the equilibrium geometries of the individual components before optimization of the graphene-dopant complex. Figure 1 shows the chemical structures of each amine-based organic molecule: **1**, **2**, and **3**. Generally, because of the lone pairs on the nitrogen atoms, amine-based dopants molecules act as electron donors, causing n-type doping of graphene. The benzene rings of the organic dopants can form stable interactions with the graphene sheet due to the formation of strong π - π interactions. To modulate the electron-donating ability of molecule **1**, electron-donating alkyl groups (**2**) and electron-withdrawing acetyl phenyl groups (**3**) were attached to the benzene rings. To construct the initial input geometry for the graphene-organic complexes, each optimized organic molecule was added to the optimized pristine graphene structure. The benzene rings of the dopants were placed directly above the hexagonal rings of the pristine graphene to maximize the overlap between the carbon atoms. The organic molecules were oriented almost parallel to the graphene sheet with separation of about ~ 3.26 Å, which is characteristic of π - π stacked systems. Here, for the studied compounds, the chosen separation values were in the range of 2.59–3.67 Å and were determined by averaging reported values [20].

The initial and optimized geometries of the complexes in side-on and top-down views are shown in Figure 2. The optimized structures of the organic molecules in the absence of the graphene sheets show that the organic molecules adopt a nonplanar geometry, mainly to reduce the steric hindrance between *ortho*-hydrogen atoms in the benzene rings. The butyl groups in **2** extend away from the benzene ring so

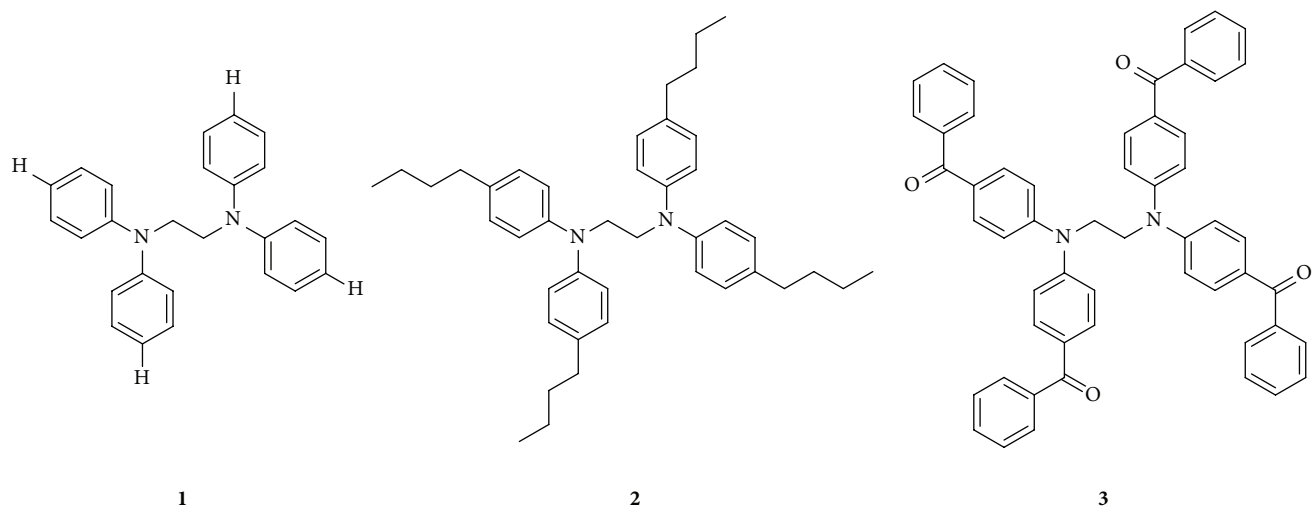


FIGURE 1: Amine-based organic molecules. Unmodified phenyl groups (1), alkylphenyl groups (2), and acetylphenyl groups (3). For clarifying the substituent effect, hydrogen atoms at the paraposition to the nitrogen are shown in 1.

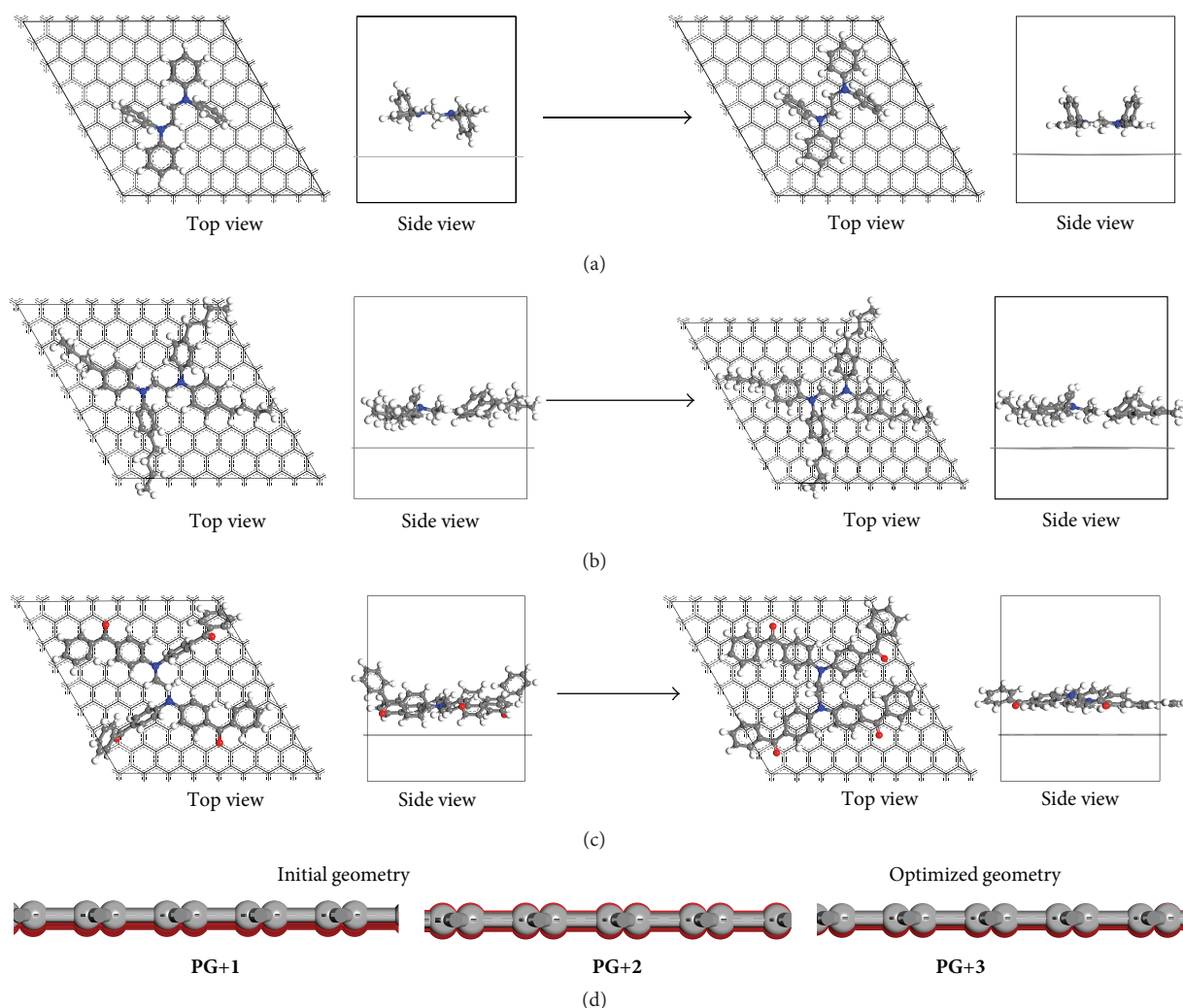


FIGURE 2: Initial and optimized structures of PG and its complexes. (a) PG+1, (b) PG+2, and (c) PG+3. (d) Comparison of the graphene structure before (black) and after (red background) optimization.

that they do not cause significant steric hindrance. Therefore, **2** has a more planar geometry than either **1** or **3**, probably also due to the electron-donating effect of the linear alkyl chains. In **3**, the outer benzene rings are displaced out of the plane of the central benzene rings and this may also be due to the steric hindrance between *ortho*-hydrogen atoms. After structure optimization, **3** showed significant structural changes in comparison with the optimized geometries of the other two adsorbed dopants. The distance between the graphene plane and the nearest nitrogen atom in the organic molecules became 3.35 Å for **1**, 3.38 Å for **2**, and 3.58 Å for **3**. Bending of the graphene sheets was observed in the graphene-organic complexes, as shown in Figure 2(d), where the side-on view of the sheets shows the slight bending of the graphene. Most benzene derivatives of organic molecules tend to be located parallel to the graphene layer with an arrangement similar to Bernal's AB stacking configuration [21]. It is possible that this stacking arrangement maximizes the attractive interactions, while minimizing the repulsive interactions between the π -orbitals of the dopant and graphene. Also, most of the hydrogen atoms of the organic molecule are located in the hexagonal lattice space of the graphene structure, that is, at the centers of hexagons. This could indicate the presence of weak, nonclassical, hydrogen bonding between the electron-rich π -cloud of graphene and the hydrogen atoms of the organic molecules. This is often termed C-H $\cdots\pi$ hydrogen bonding [20]. This type of hydrogen bonding can also increase the adsorption interaction between the graphene sheets and the adsorbed organic molecules.

The organic molecules also changed their structure after adsorption, as shown in Figure 2. The most significant change was the increase in the proximity of the outer benzene rings of the dopant molecules to the graphene sheet in **3**, which changed from its curved initial optimized geometry to a more planar geometry in the graphene-organic complex. However, the equilibrium distance between graphene and the adsorbed organic dopant is greater in **3** than the other two complexes. In addition, the dihedral angles of the ethanediamine linker of the organic molecules (-N-C-C-N-) were measured to give information on changes in the global structure of the organic molecules when they are adsorbed on graphene. The dihedral angles change from 180.122° to 189.173°, 180.703° to 184.237°, and 179.416° to 202.808° for complexes **1**, **2**, and **3**, respectively, a total angular change of +9.051°, +3.534°, and +23.392°, respectively, for each compound. All of these structural changes result in the benzene rings becoming closer to the graphene sheet, increasing π - π interactions through the bending of the backbone structure. The dihedral angle of the ethanediamine linker of compound **3** showed the most change because it has the largest area of interaction with the graphene sheet compared to **1** and **2**.

The adsorption energy (ΔE_{ads}) of the organic compounds on the graphene sheet was calculated to evaluate the degree of interaction for each organic compound on the graphene sheet. The adsorption energy was obtained by using the following equation:

$$\Delta E_{\text{ads}} = E_{\text{doped graphene}} - E_{\text{molecule}} - E_{\text{graphene}}, \quad (1)$$

where $E_{\text{doped graphene}}$, E_{molecule} , and E_{graphene} indicate the total energies of the doped graphene, organic molecule, and graphene, respectively. The adsorption energies of compounds **1**, **2**, and **3** are -3.50 eV, -4.14 eV, and -5.79 eV, respectively. The adsorption energy increases as the size of the adsorbed molecule increases. The large molecular size of compound **3** gives the largest area of orbital overlap; thus, it can interact more with the confined graphene sheet (i.e., confined to the $8 \times 8 \times 1$ graphene supercell). Also, **3** has twice the number of benzene rings as either **1** or **2**, and these aromatic rings are the main contributor to the interaction between graphene and the adsorbed organic molecule. The molecular size of **2** is larger than that of compound **1**; therefore, compound **2** has larger adsorption energy than **1**. However, the dihedral angle change of **2** is smaller than that of **1**. This may be due to the alkyl chains in **2** disrupting the interactions between the benzene rings in the organic molecule and graphene; therefore, the benzene rings of **2** cannot interact with graphene even though they have increased electron-donating ability compared to **1**. That is, although the alkyl chains increase electron density on the benzene ring, their steric bulk decreases the contact with the graphene sheet. Thus, the observed increase in the adsorption energy for **2** is less than we expected based on the electron-donating ability of the alkyl chains. For this reason, it is important to take into account the molecular structure, including steric factors, as well as the electron distribution of the molecule when designing dopants to form stable adsorbates for graphene. Compound **3** has more aromatic rings than either **1** or **2**, and the largest dihedral angle change was observed in compound **3** after geometry optimization was carried out on the adsorbed complex. From these results, we concluded that the graphene and organic molecules affect the structure of each other on the formation of a physisorbed complex and that the interaction between the two is caused by long-range interactions.

Before we close the discussion of the structural changes that occur on adsorption, we must emphasize that here we have only investigated the physisorption of organic molecules onto graphene. There were almost no structural changes to the graphene sheet after the physisorption of the dopant compared to structural changes to the organic dopants, as shown in Figure 2(d). In calculations where the organic molecule was driven closer to the graphene sheet, one carbon atom in graphene protruded out of the plane and formed a chemical bond with a nitrogen atom of the amine. However, this caused the total energy of the complex to increase, mainly due to the steric hindrance; thus, only the results from equilibrium optimized structures have been discussed in this study.

3.2. Changes to the Electronic Structure. The electronic structure of graphene changes on the adsorption of an organic molecule to graphene [22]. We found that the electronic structure of the doped graphene depended on the electronic properties of the adsorbed organic molecule. The calculated band structures for graphene and the graphene-molecule complexes are shown in Figure 3. Because the Fermi level of pristine graphene exactly crosses the Dirac point, it is well-known that graphene is a zero-gap semiconductor [23].

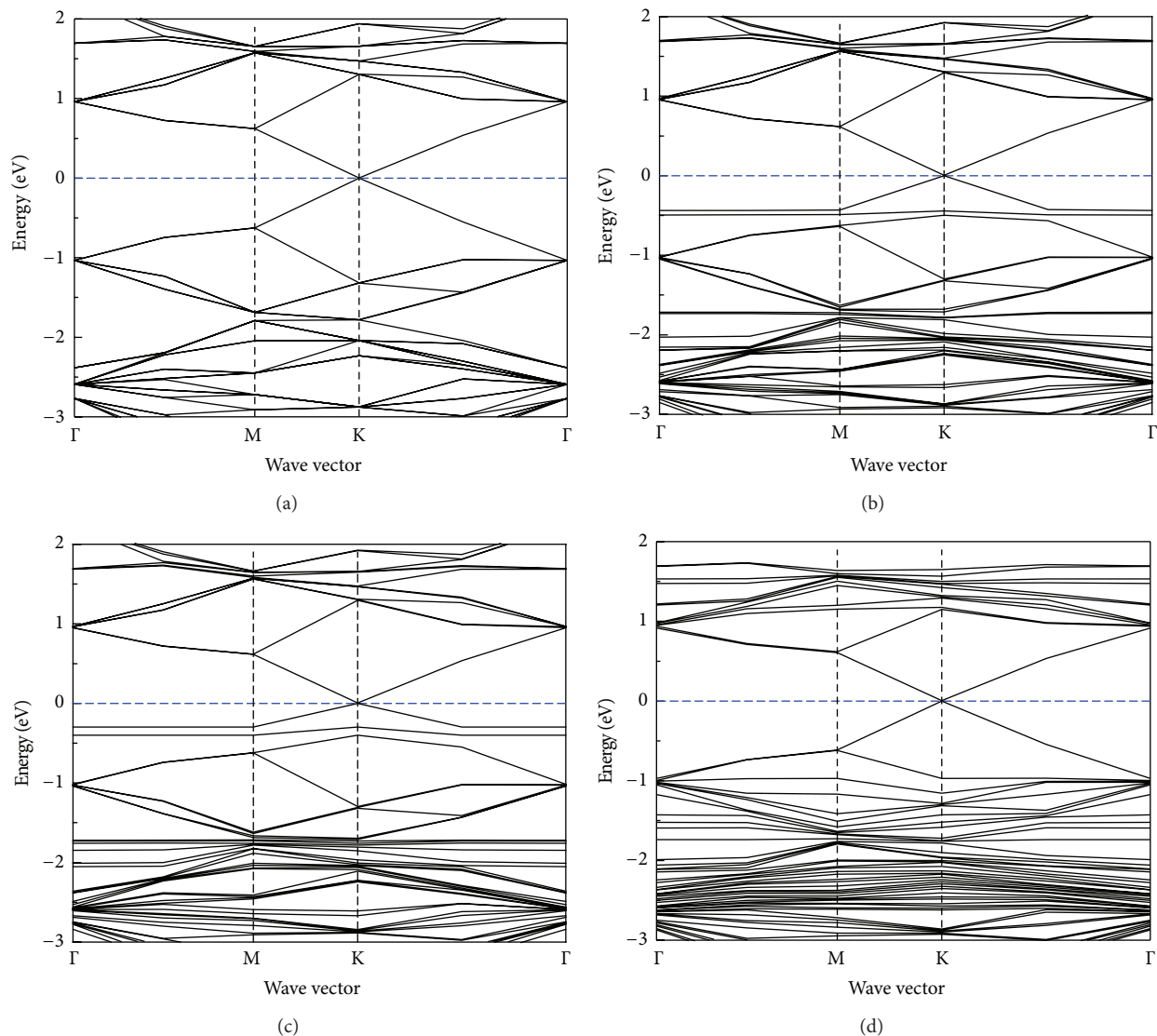


FIGURE 3: Electronic band structures in the proximity of the Fermi level of graphene and its complexes. (a) PG, (b) PG+1, (c) PG+2, and (d) PG+3 along high-symmetric points in the Brillouin zone. The energy at the Fermi level (E_F) is shown as a blue dashed line and is set to zero.

Figure 3(a) shows the electronic band structure of pristine graphene along highly symmetric points in the Brillouin zone. The fractional coordinates of these points are $\Gamma(0,0)$, $M(1/2,0)$, and $K(1/3,1/3)$. The energy of the Fermi level (E_F) is set to zero, indicated as a blue dotted line in Figure 3. The valence and conduction bands touch, and the Fermi level bisects two bands at point K. Thus, the shift in the band structure at point K gives useful information about changes in the mobility of graphene. As seen in Figures 3(b), 3(c), and 3(d), the electronic band structures of the adsorbed graphene systems show no obvious differences at point K close to the Fermi level compared to pristine graphene; therefore, no changes in mobility should occur after the adsorption of dopants onto graphene. No band structure changes at point K of the Fermi level were observed because no defects are formed during physisorption. For this reason, doping by physisorption is different from other

destructive doping techniques such as substitutional doping or the covalent functionalization of graphene [24]. However, when the organic molecules are placed on the graphene sheet, the valence bands become complicated, especially in comparison with the conduction bands. Therefore, we assume that the adsorbed organic molecules have a large impact on the valence band of graphene.

Frontier orbitals and energy diagrams of each adsorbed graphene complex are shown in Figure 4. Analysis of the frontier orbitals of the adsorbed graphene showed that the organic molecules influenced the highest occupied molecular orbital (HOMO) energy of the graphene-molecule complex and the pristine graphene sheet was related to the lowest unoccupied molecular orbital (LUMO) energy of the adsorbed graphene. On formation of the graphene-molecule complex, the HOMO and LUMO energies decreased compared to the energies of the HOMO of the organic molecules

TABLE 1: HOMO and LUMO orbital energies (in eV) for graphene, molecules, and graphene-molecule systems and Fermi-level energies (in eV) for graphene and graphene-molecule systems.

	PG	1	2	3	PG+1	PG+2	PG+3
HOMO	-5.49	-4.61	-4.36	-5.18	-4.90	-4.75	-5.45
LUMO	-3.49	-1.37	-1.19	-3.06	-3.51	-3.59	-3.57
Fermi level	-4.49	—	—	—	-4.42	-4.58	-4.52

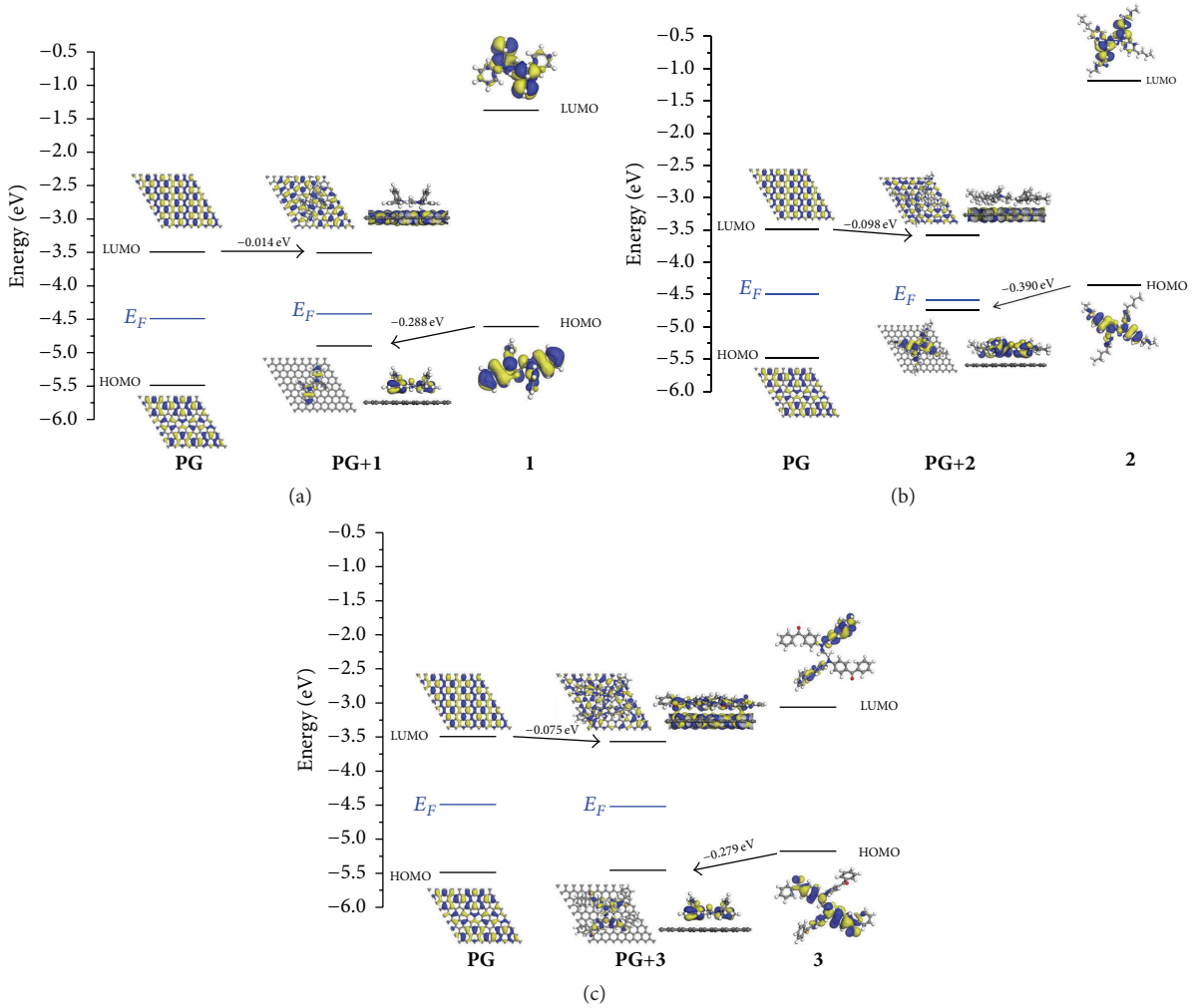


FIGURE 4: HOMO and LUMO isosurfaces and energies for graphene complexes. (a) PG+1, (b) PG+2, and (c) PG+3 systems.

and the LUMO of the pristine graphene sheet. Interestingly, when the isovalue for displaying the LUMO isosurface is set equal to 0.01, the LUMO of **3** is spread over graphene and the organic molecule; in contrast, the LUMOs of **1** and **2** are localized on the graphene sheet. In frontier molecular orbital theory, the HOMO and the LUMO energies are related to the degree of intermolecular charge transfer. If the HOMO energy of the organic molecules is higher than the Fermi energy level of pristine graphene, charge transfer can take place from the molecule to graphene. The obverse is also true; that is, if the LUMO of the molecule is lower than the Fermi energy level of pristine graphene, charge transfer can occur from graphene to the molecule [25]. The HOMOs and LUMOs of graphene, the organic molecules,

and graphene-molecule complexes, and the energies of the Fermi level for both graphene and graphene-molecule systems are summarized in Table 1. The calculated Fermi energy for pristine graphene is -4.49 eV, which is between the HOMO and LUMO energies of graphene. Only the HOMO level of **2** is higher than the Fermi level of pristine graphene; therefore, intermolecular charge transfer could occur from **2** to graphene. Intermolecular charge transfer is one of the reasons why the Fermi energy level of the PG+2 complex is very close to its HOMO energy compared to other adsorbed graphene systems. The Fermi energy level of the graphene-molecule complexes is influenced by the HOMO energy of the adsorbed organic molecules and by the intermolecular charge transfer between the molecule and graphene. Also,

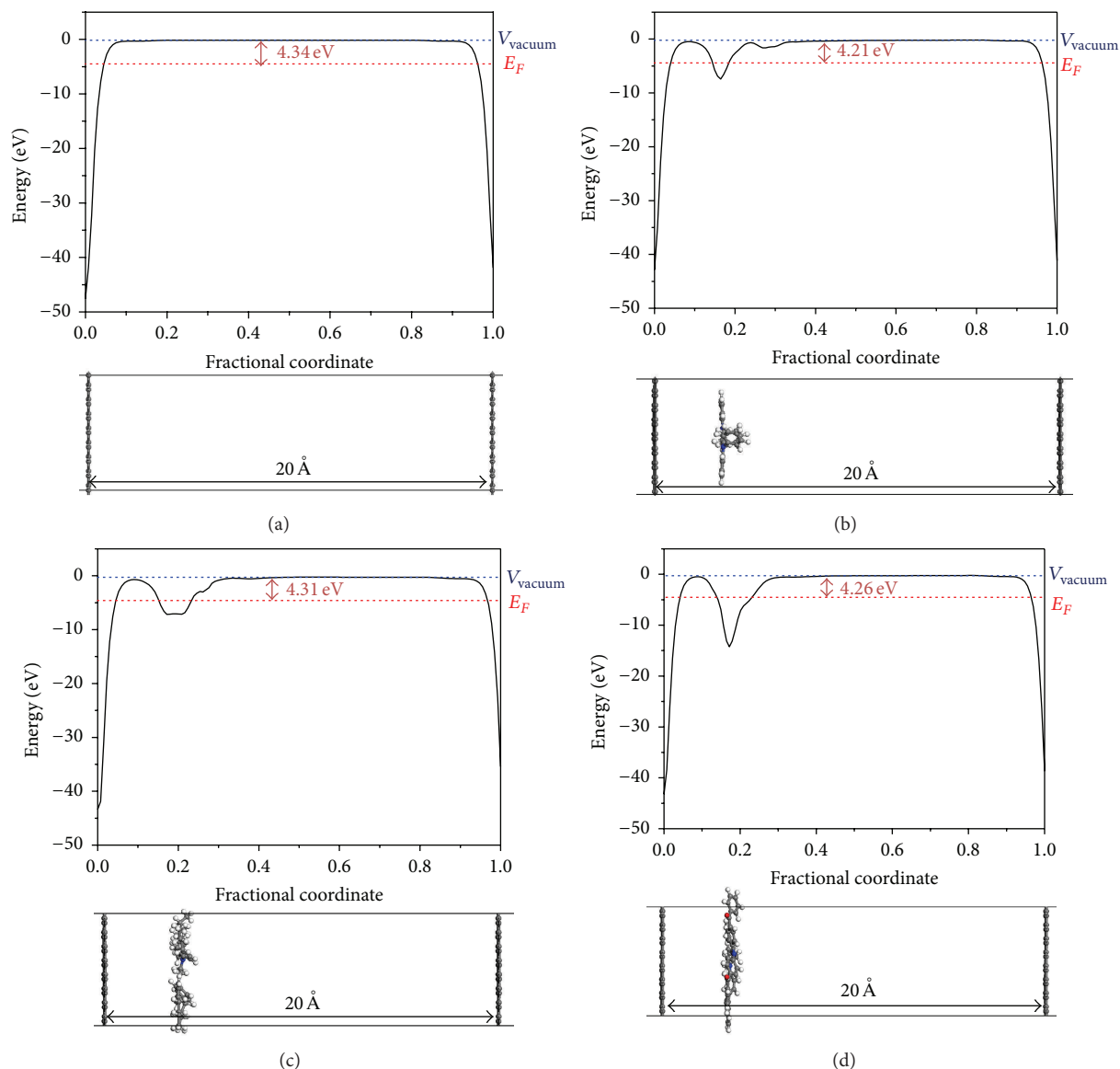


FIGURE 5: Electrostatic potential diagrams for graphene and the adsorbed complexes. Calculated electrostatic potential diagrams along the c -axis for (a) PG, (b) PG+1, (c) PG+2, and (d) PG+3 systems.

this result is indicative of the electron-donating effect of the alkyl chains on the benzene rings. Increased electron density on the benzene ring may facilitate electron transfer from the adsorbed organic molecules to the graphene sheet.

3.3. Work Function Calculations. Electrostatic potential calculations were used to probe changes in the work function on adsorption of the dopants onto graphene. Figure 5 shows the electrostatic potential calculations for pristine graphene and for PG+1, PG+2, and PG+3. Because of the flat average potential between the graphene layers, which are separated by 20 Å, there would be no interaction between the graphene layers. A lower electrostatic potential energy is obtained at regions of greater electron density. Because the graphene sheets have a greater electron density than the

organic molecules, a lower electrostatic potential energy close proximity to graphene was calculated. At a shift along the c -axis of 0.2 (in fractional coordinates), differences were noted in the electrostatic potential profiles that were dependent on the organic dopant; thus, different electrostatic potential diagrams were obtained for each organic compound. The computed vacuum potentials and Fermi energies and work functions are tabulated in Table 2. In a previous report, the work function of CVD-grown monolayer graphene was approximately 4.3 eV [5]. This value corresponds to the work function of our simulations of pristine graphene (4.34 eV); therefore, the DFT electrostatic potential calculation with DMol³ can reproduce experimentally determined work functions quantitatively. The work functions of each graphene-organic complex are smaller than those of pristine graphene.

TABLE 2: Computed Fermi energies, vacuum potentials, work functions, and the type of doping (n or p) effects of **PG** and adsorbed graphene sheets.

	Fermi energy (eV)	Vacuum potential (eV)	Work function (eV)	Doping effect
PG	-4.49	-0.15	4.34	—
PG+1	-4.42	-0.21	4.21	n
PG+2	-4.58	-0.27	4.31	n
PG+3	-4.52	-0.26	4.26	n

The work function is influenced by both the Fermi level and the vacuum potential. However, the vacuum potential in work function detection depends on the surface of solid [26]. Because controlling the surface of doped graphene is practically difficult, it is difficult to tune the vacuum potential to a particular level using different organic adsorbates. Therefore, tuning the Fermi energy level, which is possible, is key to altering the properties of graphene by doping. As described in Section 3.2, the HOMO energy level of the organic molecules and the intermolecular charge transfer between molecule and graphene can change the Fermi energy level of the graphene-organic complex. If we only consider the Fermi energy levels of the graphene-organic complex and pristine graphene, the work functions are in the order $\text{PG+2} > \text{PG+3} > \text{PG} > \text{PG+1}$. However, the presence of the organic molecules on graphene affects the electrostatic environment in the region where the detached electron can escape. As a result, the work functions calculated from our DFT calculations are in the order $\text{PG} > \text{PG+2} > \text{PG+3} > \text{PG+1}$. Interestingly, the energy of the HOMO of organic compounds and of pristine graphene is in the order $2 > 1 > 3 > \text{PG}$, which tells us that DFT calculation on the isolated molecules cannot predict the work function of graphene-organic complex properly. Thus, the molecular design of organic dopants will benefit from solid-state DFT calculations that simulate the graphene-organic complexes.

Using the DFT calculations, we confirmed that the amine-based organic compounds induce an n-type doping effect on graphene even if there is no change in the band structure at the *K* point. As a result, when amine-based organic molecules are adsorbed onto the graphene sheet, the adsorbed molecules have no effect on the mobility of graphene. However, the Fermi energy of the graphene-organic complex is influenced by the different organic molecules.

4. Conclusion

To summarize, DFT calculations using PBE/DNP and TS dispersion correction were performed to investigate the effect of doping graphene with amine-based molecules. Dopant molecules with a larger steric size have greater orbital overlap and have a greater binding energy, which stabilizes the adsorbed dopant. Electron transfer from the dopant organic molecules to the graphene sheet was facilitated by increasing the electron density on the benzene rings of the adsorbed

molecule. Also, directing some hydrogen atoms of the organic dopant towards the graphene to form nonclassical hydrogen bonds increased the stability of the adsorbed molecules. Work function calculations revealed that the amine-based organic molecules induce an n-doping effect on graphene by decreasing the work function of graphene on formation of the graphene-organic complex. However, there is no change in band structure at the *K* point of the Fermi level because these systems are doped by physisorption. Therefore, adsorbed amine-based molecules do not affect the mobility of graphene. However, the work function was affected by changing the Fermi level of graphene, and this was observed in the graphene-organic complexes. In conclusion, solid-state DFT calculation is a useful tool to guide the design of organic dopants on graphene.

Conflict of Interests

The authors declare that there is no conflict of interests regarding the publication of this paper.

Acknowledgments

This research was supported by the Chung-Ang University Excellent Student Scholarship to Yeun Hee Hwang and by the Public Welfare & Safety research program through the National Research Foundation of Korea (NRF) funded by the Ministry of Education, Science and Technology (NRF-2010-0020819).

References

- [1] Z.-S. Wu, W. C. Ren, L. B. Gao et al., "Synthesis of graphene sheets with high electrical conductivity and good thermal stability by hydrogen arc discharge exfoliation," *ACS Nano*, vol. 3, no. 2, pp. 411–417, 2009.
- [2] Y. Xu, Y. Wang, J. Liang et al., "A hybrid material of graphene and poly (3,4-ethyldioxythiophene) with high conductivity, flexibility, and transparency," *Nano Research*, vol. 2, no. 4, pp. 343–348, 2009.
- [3] S. Das Sarma, S. Adam, E. H. Hwang, and E. Rossi, "Electronic transport in two-dimensional graphene," *Reviews of Modern Physics*, vol. 83, no. 2, pp. 407–470, 2011.
- [4] K. S. Kim, Y. Zhao, H. Jang et al., "Large-scale pattern growth of graphene films for stretchable transparent electrodes," *Nature*, vol. 457, no. 7230, pp. 706–710, 2009.
- [5] S. Bae, H. Kim, Y. Lee et al., "Roll-to-roll production of 30-inch graphene films for transparent electrodes," *Nature Nanotechnology*, vol. 5, no. 8, pp. 574–578, 2010.
- [6] H. Ishii, K. Sugiyama, E. Ito, and K. Seki, "Energy level alignment and interfacial electronic structures at organic/metal and organic/organic interfaces," *Advanced Materials*, vol. 11, no. 8, pp. 605–625, 1999.
- [7] L. S. Panchakarla, K. S. Subrahmanyam, S. K. Saha et al., "Synthesis, structure, and properties of boron- and nitrogen-doped graphene," *Advanced Materials*, vol. 21, no. 46, pp. 4726–4730, 2009.
- [8] H. Liu, Y. Liu, and D. Zhu, "Chemical doping of graphene," *Journal of Materials Chemistry*, vol. 21, no. 10, pp. 3335–3345, 2011.

- [9] D. G. Reuven, H. B. M. Shashikala, S. Mandal, M. N. V. Williams, J. Chaudhary, and X.-Q. Wang, "Supramolecular assembly of DNA on graphene nanoribbons," *Journal of Materials Chemistry B*, vol. 1, no. 32, pp. 3926–3931, 2013.
- [10] X. Dong, D. Fu, W. Fang, Y. Shi, P. Chen, and L.-J. Li, "Doping single-layer graphene with aromatic molecules," *Small*, vol. 5, no. 12, pp. 1422–1426, 2009.
- [11] J. Park, W. H. Lee, S. Huh et al., "Work-function engineering of graphene electrodes by self-assembled monolayers for high-performance organic field-effect transistors," *The Journal of Physical Chemistry Letters*, vol. 2, no. 8, pp. 841–845, 2011.
- [12] Y. Jang, J. H. Cho, D.-H. Kim, Y. D. Park, M. Hwang, and K. Cho, "Effects of the permanent dipoles of self-assembled monolayer-treated insulator surfaces on the field-effect mobility of a pentacene thin-film transistor," *Applied Physics Letters*, vol. 90, no. 13, Article ID 132104, 2007.
- [13] T. Schiros, D. Nordlund, L. Pálóvá et al., "Connecting dopant bond type with electronic structure in n-doped graphene," *Nano Letters*, vol. 12, no. 8, pp. 4025–4031, 2012.
- [14] S. F. Rastegar, N. L. Hadipour, M. B. Tabar, and H. Soleymanabadi, "DFT studies of acrolein molecule adsorption on pristine and Al-doped graphenes," *Journal of Molecular Modeling*, vol. 19, no. 9, pp. 3733–3740, 2013.
- [15] B. Delley, "From molecules to solids with the DMol³ approach," *The Journal of Chemical Physics*, vol. 113, no. 18, pp. 7756–7764, 2000.
- [16] J. P. Perdew, K. Burke, and M. Ernzerhof, "Generalized gradient approximation made simple," *Physical Review Letters*, vol. 77, no. 18, pp. 3865–3868, 1996.
- [17] J. P. Perdew, K. Burke, and M. Ernzerhof, "Generalized gradient approximation made simple," *Physical Review Letters*, vol. 77, no. 18, pp. 3865–3868, 1996, Erratum in: *Physical Review Letters*, vol. 78, p. 1396, 1997.
- [18] S. Kurth, J. P. Perdew, and P. Blaha, "Molecular and solid-state tests of density functional approximations: LSD, GGAs, and Meta-GGAs," *International Journal of Quantum Chemistry*, vol. 75, no. 4-5, pp. 889–909, 1999.
- [19] A. Tkatchenko and M. Scheffler, "Accurate molecular van der Waals interactions from ground-state electron density and free-atom reference data," *Physical Review Letters*, vol. 102, no. 7, Article ID 073005, 2009.
- [20] P. P. Zhou and R. Q. Zhang, "Physisorption of benzene derivatives on graphene: critical roles of steric and stereoelectronic effects of the substituent," *Physical Chemistry Chemical Physics*, vol. 17, no. 18, pp. 12185–12193, 2015.
- [21] S. Gowtham, R. H. Scheicher, R. Ahuja, R. Pandey, and S. P. Karna, "Physisorption of nucleobases on graphene: density-functional calculations," *Physical Review B*, vol. 76, no. 3, Article ID 033401, 2007.
- [22] O. Leenaerts, B. Partoens, and F. M. Peeters, "Adsorption of small molecules on graphene," *Microelectronics Journal*, vol. 40, no. 4-5, pp. 860–862, 2009.
- [23] J. Yao, Y. Sun, M. Yang, and Y. Duan, "Chemistry, physics and biology of graphene-based nanomaterials: new horizons for sensing, imaging and medicine," *Journal of Materials Chemistry*, vol. 22, no. 29, pp. 14313–14329, 2012.
- [24] D. Wei, Y. Liu, Y. Wang, H. Zhang, L. Huang, and G. Yu, "Synthesis of N-doped graphene by chemical vapor deposition and its electrical properties," *Nano Letters*, vol. 9, no. 5, pp. 1752–1758, 2009.
- [25] O. Leenaerts, B. Partoens, and F. M. Peeters, "Adsorption of H₂O, N H₃, CO, NO₂, and NO on graphene: a first-principles study," *Physical Review B: Condensed Matter and Materials Physics*, vol. 77, Article ID 125416, 2008.
- [26] R. W. Strayer, W. Mackie, and L. W. Swanson, "Work function measurements by the field emission retarding potential method," *Surface Science*, vol. 34, no. 2, pp. 225–248, 1973.

Research Article

Nanotextured Morphology of Poly(methyl methacrylate) and Ultraviolet Curable Poly(urethane acrylate) Blends via Phase Separation

Ju-Hyung Kim,¹ Joon H. Kim,² and Soonmin Seo³

¹Department of Chemical Engineering, Pukyong National University, Busan 608-739, Republic of Korea

²School of Chemical and Biological Engineering, Seoul National University, Seoul 151-742, Republic of Korea

³College of BioNano Technology, Gachon University, Gyeonggi 461-701, Republic of Korea

Correspondence should be addressed to Soonmin Seo; soonmse@gachon.ac.kr

Received 29 June 2015; Accepted 13 August 2015

Academic Editor: Moon Il Kim

Copyright © 2015 Ju-Hyung Kim et al. This is an open access article distributed under the Creative Commons Attribution License, which permits unrestricted use, distribution, and reproduction in any medium, provided the original work is properly cited.

Domain structures of spin-coated immiscible poly(methyl methacrylate) (PMMA) and ultraviolet (UV) curable poly(urethane acrylate) (PUA) blends were studied using atomic force microscopy (AFM). Spin casting the PMMA/PUA blends in propylene glycol monomethyl ether acetate (PGMEA) was accompanied with phase separation, and PUA was subsequently cross-linked under UV radiation. Selective dissolution of PMMA in the phase-separated films was feasible using tetrahydrofuran (THF) solvent after the UV curing process, because the cured PUA material is highly stable against THF. Morphology of phase-separated structure, including domain size and height, could be controlled by varying total concentration of the blended solution, and various nanoscale features such as island-like and hole-like structures were achieved by changing weight ratio of the two immiscible polymers.

1. Introduction

Morphological control of immiscible polymer blends has been widely studied in regard to phase geometry and dimensions, which can lead to many practical applications [1–5]. Particularly, it is well known that domain structures and surface topography strongly depend on various polymer interactions (i.e., polymer-polymer and polymer-surface interactions) in the blended films, and the relative solubility of polymers in a common solvent can play a crucial role in determination of surface morphology [6]. Previous study also showed that surface structures of the blended films of polystyrene (PS) and poly(methyl methacrylate) (PMMA) are remarkably changed by varying the film thickness [7]. Spin-coating is a simple method for fabricating thin polymer films, which facilitates precise and easy control of film thickness by rotational velocity and concentration of polymer solution [8, 9]. If the blended solution of two different immiscible polymers dissolved in a common solvent is spin-coated, phase separation normally occurs during the evaporation

of solvent. Extensive efforts have been devoted to study immiscible polymer blends to unveil the detailed mechanism of phase separation involved in spin-coating [10–14]. In addition, selective dissolution of one component in phase-separated polymer blends provides important advantages for easy fabrication of micro- or nanosized patterns which are widely used in application fields [15, 16]. However, various interactions, such as polymer-polymer and polymer-surface interactions, cause complexity and difficulty in control of the selective dissolution and fabrication of desired structures.

Here we present a binary immiscible polymer-blended system with high stability which enables complete selective dissolution of one component. For this work, PMMA and ultraviolet (UV) curable poly(urethane acrylate) (PUA) were used [17–19], and the phase separation of PMMA/PUA blend was well-driven via solvent evaporation. Morphological changes in the PMMA/PUA blended film according to total concentration and weight ratio of the blended solution were investigated using atomic force microscopy (AFM). Selective dissolution of PMMA in the phase-separated films

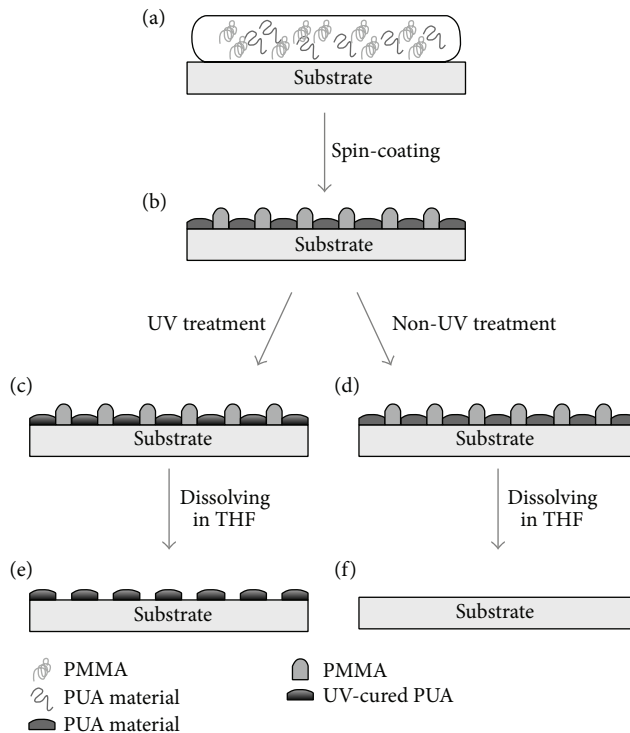


FIGURE 1: Schematic illustration of phase separation of PMMA/PUA upon the spin-coating process and selective dissolution before and after UV curing.

was feasible using tetrahydrofuran (THF) solvent after the UV curing process, because the cured PUA material is highly stable against THF. Morphology of phase-separated structure, including domain size and height, could be controlled by varying total concentration of the blended solution, and various nanoscale features such as island-like and hole-like structures were achieved by changing weight ratio of the two immiscible polymers. These results strongly suggest great potential for various applications in the field of soft lithography, such as antireflection layers, polymer membranes, artificial superhydrophobic surfaces, and nanopatterned structures.

2. Materials and Methods

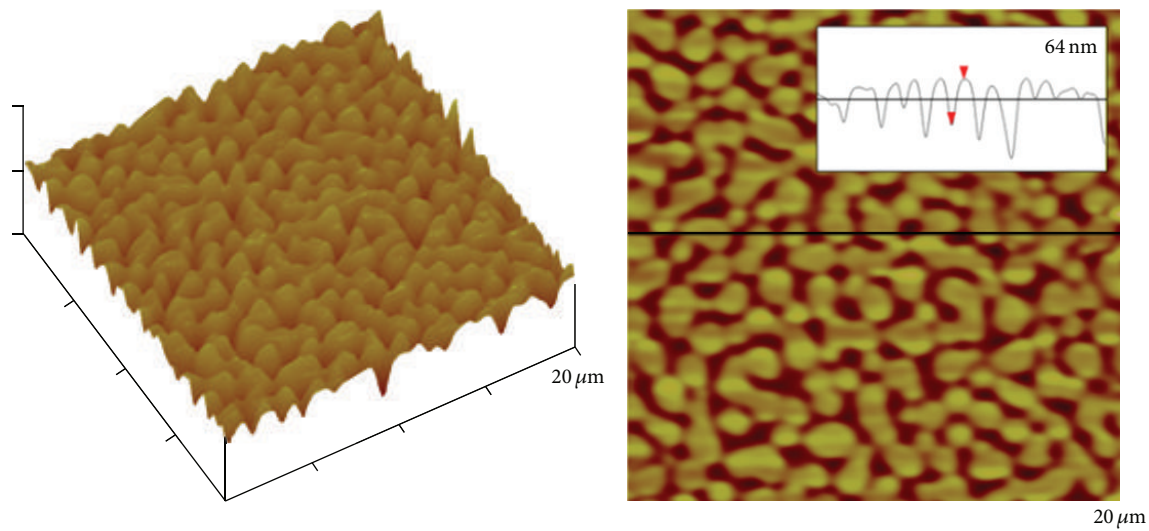
PMMA ($M_n = 11,500$ g/mol, $M_w/M_n = 1.08$, Polymer Source Inc.) was used as received, and the UV curable PUA mixture was synthesized in accordance with the previous reports [17]. The molecular weight of PUA could be altered by adjusting a molecular weight of a functionalized prepolymer with acrylate group, and PUA with a similar molecular weight to PMMA ($M_n = 11,500$ g/mol) was used for this work. Propylene glycol monomethyl ether acetate (PGMEA) was selected for a common solvent for the immiscible polymer blend of PMMA and PUA. The polymer-blended solutions with different concentrations were prepared to evaluate the effects. The blend with 15 wt% PUA and 15 wt% PMMA was used to demonstrate the complete selective dissolution of PMMA. The effects of total concentration with the same weight ratio of PMMA : PUA (35 : 65) were examined using

three solutions: (i) 7 g of 10 wt% PMMA mixed with 13 g of 10 wt% PUA, (ii) 7 g of 15 wt% PMMA mixed with 13 g of 15 wt% PUA, and (iii) 7 g of 20 wt% PMMA mixed with 13 g of 20 wt% PUA, respectively. The PMMA/PUA blends with different weight ratios of PMMA : PUA (3 : 7, 4 : 6, and 5 : 5, resp.) were also prepared by mixing 12 wt% of PMMA and PUA for further evaluation of the mixing effects.

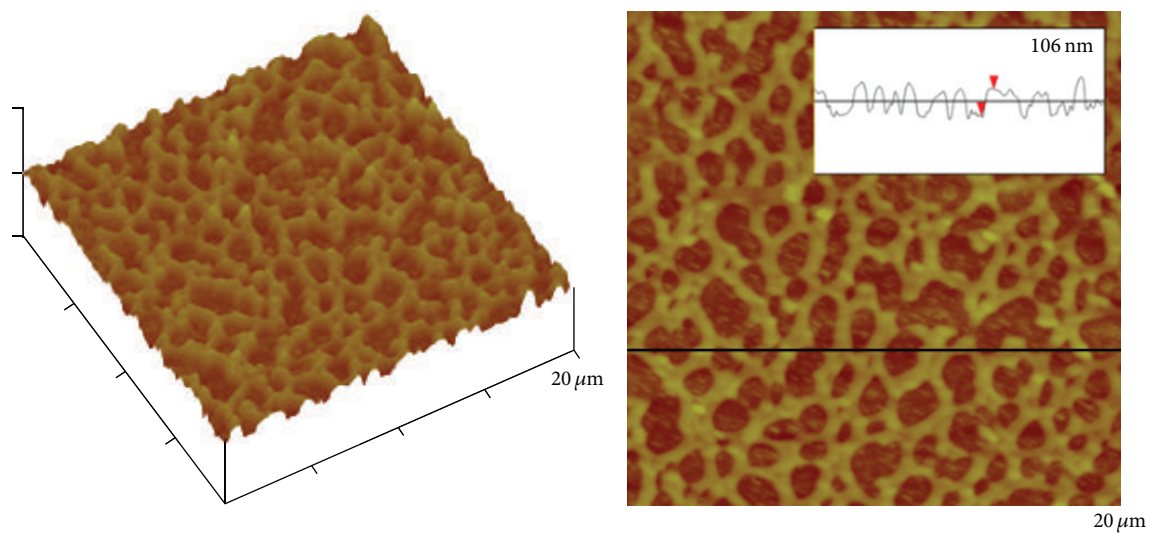
Prior to spin-coating of the solutions, silicon (Si) wafer substrates were cleaned by successive sonication in trichloroethylene, acetone, and isopropyl alcohol for 5 min each. The polymer-blended solutions were then individually spin-coated at 3000 rpm for 30 s onto the prepared Si substrates. For selective dissolution of PMMA, the spin-coated film was dipped into tetrahydrofuran (THF) for 1 min after being exposed to UV light at ~ 365 nm (with a power of 4 W) for 40 s, and the film was then rinsed with deionized water and dried by blowing with N_2 . Note that the UV curing process was performed in the argon purged glove box, because oxygen plays a role as an inhibitor to photoinitiators. The surface morphology of each sample was analyzed by atomic force microscopy (Digital Instrument Dimension 3100) in the tapping mode, and the film thicknesses were measured using reflectometer (Nanospec, K-MAC).

3. Results and Discussion

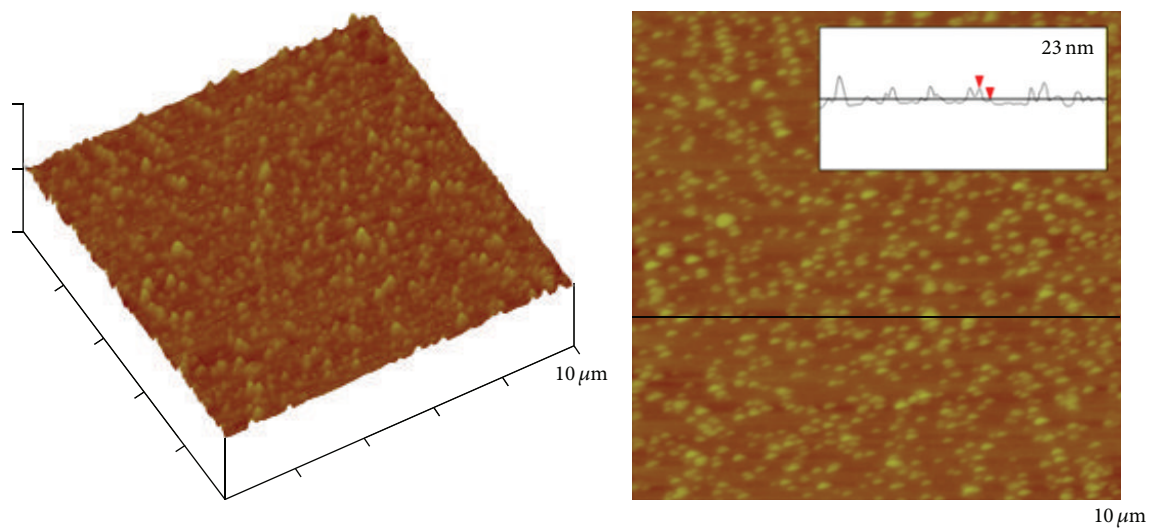
Phase separation and selective dissolution in the PMMA/PUA blend are schematically illustrated in Figure 1. The phase separation of PMMA/PUA blend was well-driven via solvent evaporation during spin-coating. The UV curable



(a)

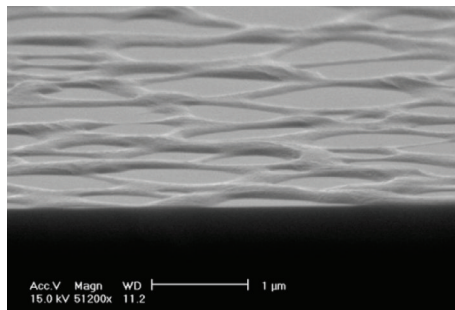


(b)



(c)

FIGURE 2: Continued.



(d)

FIGURE 2: AFM images of (a) the PMMA/PUA (30 : 70) blended film after spin-coating of the 15 wt% blended solution, (b) the cured PUA domains remaining after selective dissolution of PMMA in THF, and (c) the noncured film after dissolving in THF. The height profiles are shown in insets. (d) SEM image of (b).

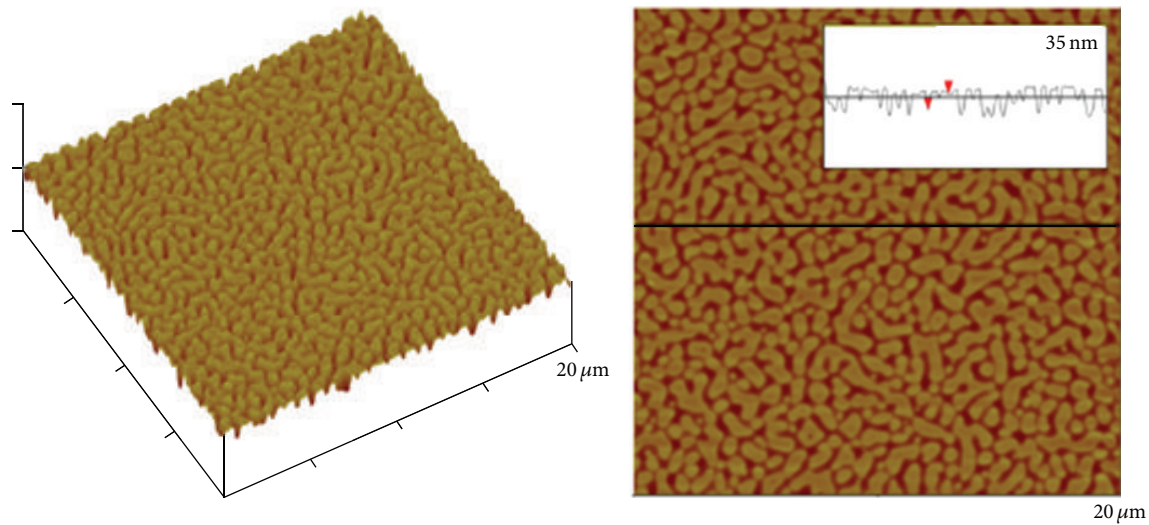
PUA mixture consists of functionalized prepolymer with acrylate group, photoinitiator, and releasing agent for the surface activity, and the UV curing process induces cross-linking in the PUA mixture [17, 18]. Thus the cured PUA mixture is chemically stable against the THF treatment compared to noncured PUA and also shows high durability at high temperature ($\sim 300^\circ\text{C}$). As illustrated in Figure 1, the cross-linked PUA domains remain even after dissolving the blended film in THF, whereas the PMMA domains are completely dissolved in THF. It is worth noting that the noncured PUA domains are also well-dissolved in THF. These results indicate that target materials for dissolution can be selectively available via a simple UV curing process.

Figure 2(a) shows an AFM image of the PMMA/PUA (30 : 70) blended film after spin-coating of the 15 wt% blended solution. The bright and dark regions in Figure 2(a) are corresponding to PMMA and PUA, respectively. Phase separation in spin-coated films is normally explained by various mechanisms, such as polymer-surface interactions, surface energy differences between polymers, and fast solvent evaporation of one component in polymer blends [20, 21]. In consideration of thermodynamic behaviors, PUA material would move to the air-polymer interface to minimize interfacial free energy, because PUA has a lower surface tension than PMMA (i.e., 26 mN/m for PUA and 42 mN/m for PMMA). However, in this work, PUA mostly remains at the polymer-substrate interface, which possibly originates from spinodal decomposition due to the differences of solvent evaporation rate for each polymer and polymer solubility in the common solvent. PGMEA is a better solvent for PUA compared to PMMA, and thus the PUA-rich domains contain more PGMEA than the PMMA domains. As the solvent evaporates during spin-coating, PGMEA in PMMA drains away prior to the PUA domains which are still swollen with PGMEA. Consequently, the solvent in PMMA is quickly depleted in the spin-coating process, which leads to elevation of the PMMA domains onto the PUA-rich domains. Figure 2(b) shows the cured PUA domains remaining after the THF treatment. The bright region in Figure 2(b) corresponds to the PUA domains dispersed on the substrate after spin-coating. However, no apparent domains were left on the noncured film after

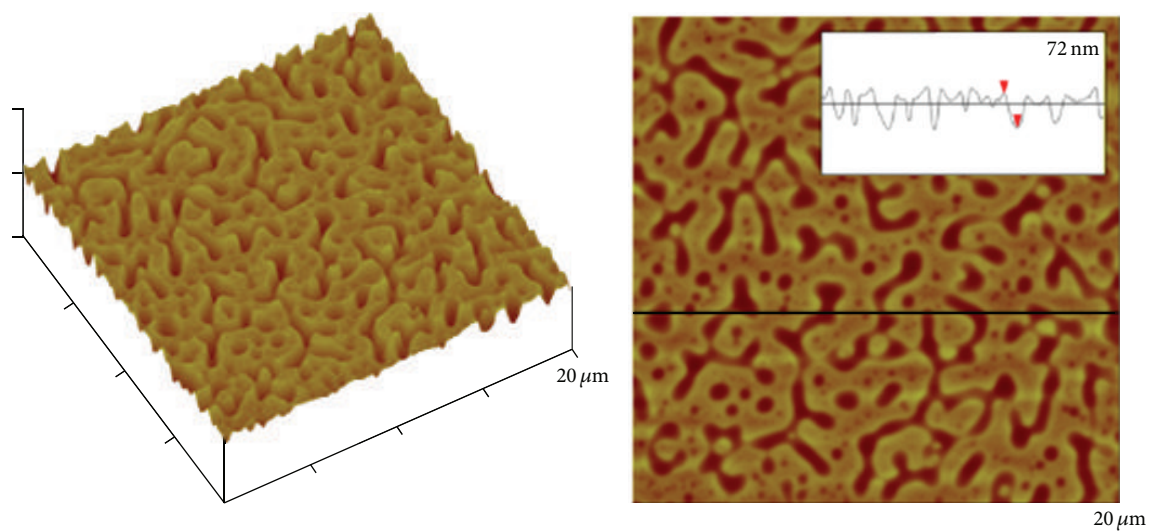
dissolving in THF as shown in Figure 2(c), which implies that the noncured PUA domains are removed with PMMA together during the THF treatment. Although the solubility of PUA in THF is relatively low, the noncured PUA can be dissolved in THF due to the polymer interactions between PUA and PMMA [12].

The film thickness of each sample was measured using reflectometer, as indicated in the insets of Figure 2. Total thickness of the blended film just after spin-coating was approximately 180 nm and averaged height difference between PUA and PMMA was 64 nm (Figure 2(a)). After selective PMMA dissolution, the remaining film thickness was ~ 106 nm (Figure 2(b)). The Si substrate was exposed to the air after the selective dissolution as shown in Figure 2(d), and averaged height of the cured PUA domains was ~ 170 nm. The height of the cured PUA domains was almost the same as the total thickness of the blended film, implying that PUA and PMMA are phase-separated on the substrate as illustrated in Figure 1(b). Note that the substrate exposure induced from the selective dissolution without additional etching process can be applied to further applications, such as antireflection layers.

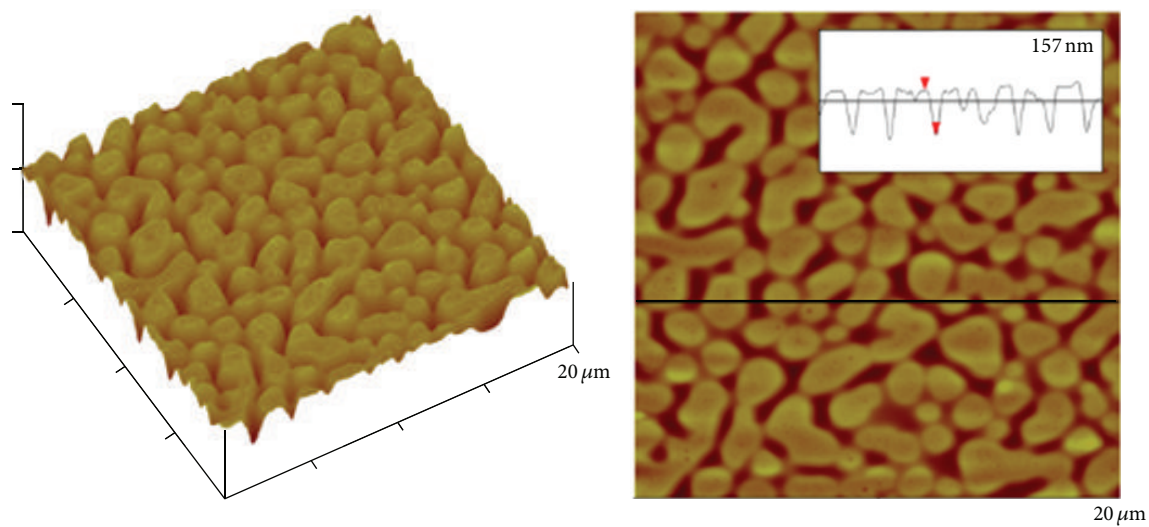
Morphology of the PMMA/PUA blend, including domain size and height, can be varied with the total concentration of solution. Three different total concentrations with the same weight ratio of PMMA : PUA (35 : 65) were used to evaluate the effects of total concentration (see Section 2). Figure 3 shows the morphological change as the total PMMA/PUA concentration increases. Averaged height differences between the cured PUA domains and the PMMA domains before the THF treatments were ~ 35 nm, ~ 72 nm, and ~ 157 nm for the 10 wt%, 15 wt%, and 20 wt% blended solutions, respectively (Figures 3(a)–3(c)). After the THF treatments, the heights of the cured PUA were found to be ~ 61 nm (for 10 wt%), ~ 119 nm (for 15 wt%), and ~ 170 nm (for 20 wt%), respectively (Figures 3(d)–3(f)). These results indicate that both PMMA and PUA heights increase as the total concentration of the blend increases. In addition, the PMMA/PUA blends with different weight ratios of PMMA : PUA were also examined for further evaluation of the mixing effects (see Section 2). Figure 4



(a)



(b)



(c)

FIGURE 3: Continued.

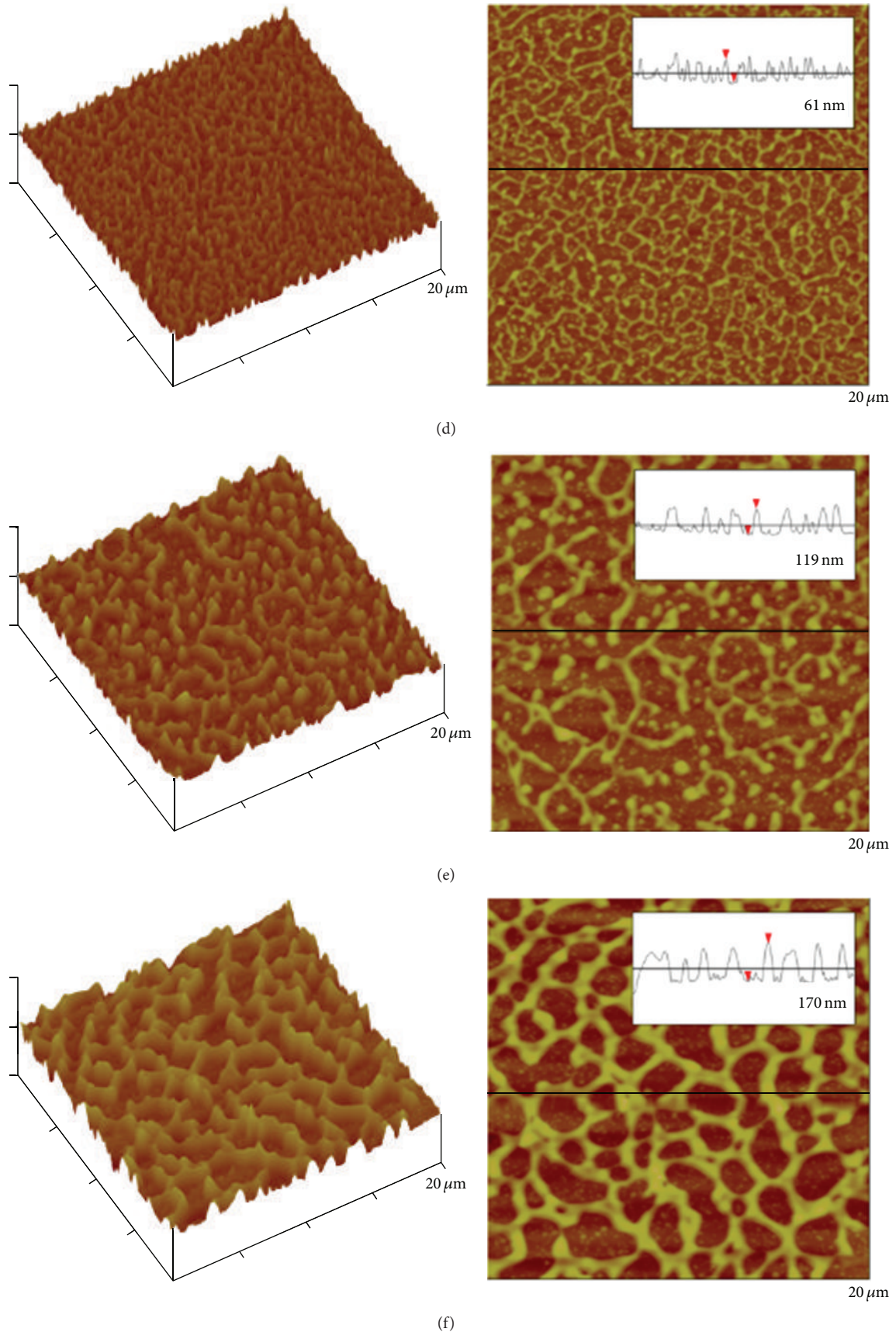


FIGURE 3: AFM images of the PMMA/PUA blended films with different total concentrations. The cured PUA domains and the PMMA domains before the THF treatments for (a) 10 wt%, (b) 15 wt%, and (c) 20 wt% blended solutions, and the cured PUA domains remaining after the THF treatments for (d) 10 wt%, (e) 15 wt%, and (f) 20 wt% blended solutions. The height profiles are shown in insets.

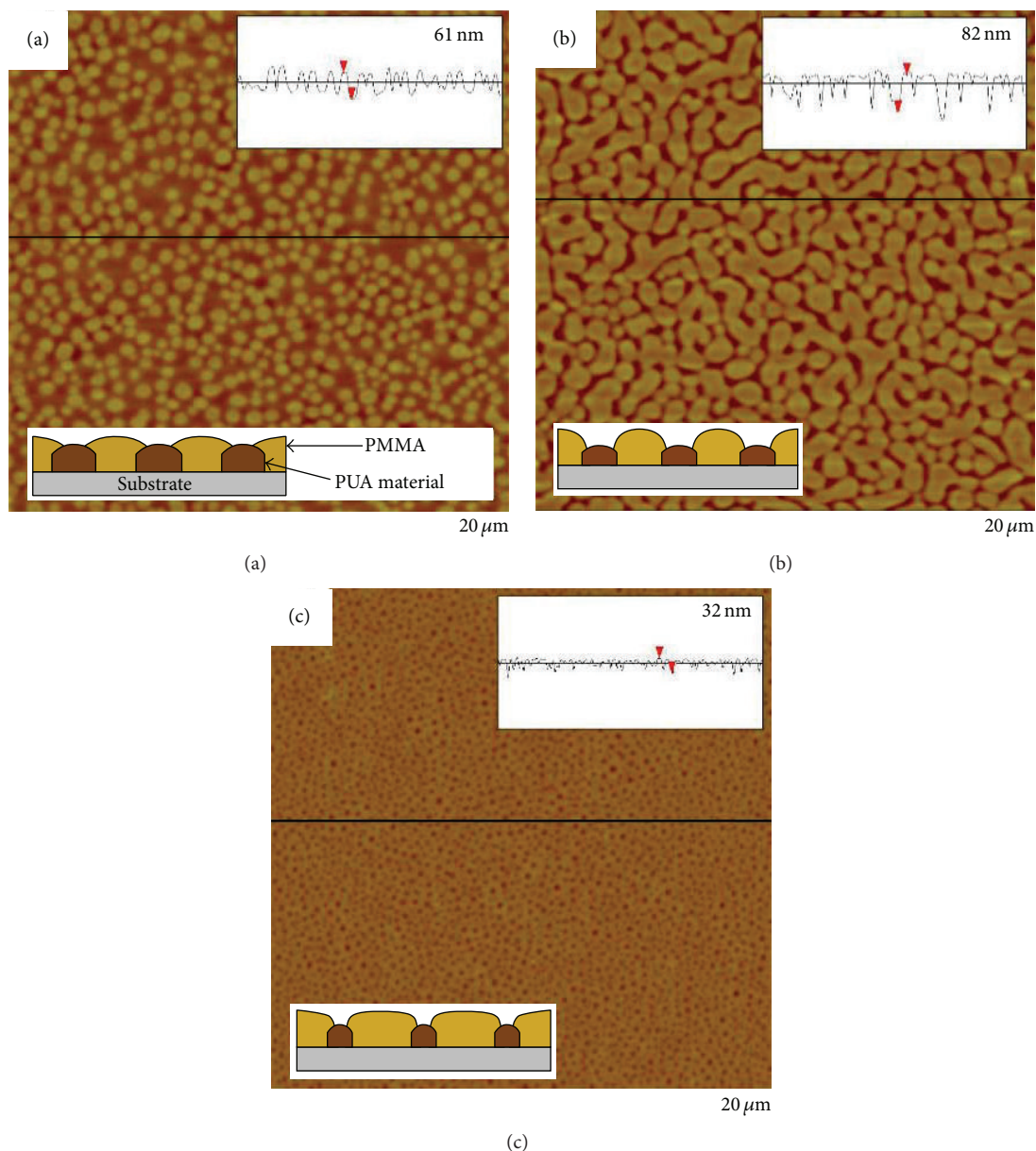


FIGURE 4: Morphology of the PMMA/PUA blended films with different weight ratios of PMMA : PUA in the 12 wt% solutions. The weight ratios of PMMA : PUA are (a) 3 : 7 ($\varphi = 0.3$), (b) 4 : 6 ($\varphi = 0.4$), and (c) 5 : 5 ($\varphi = 0.5$). Height profiles and schematic illustrations of the phase-separated domains are shown in insets.

shows morphology of the PMMA/PUA blended films with different weight ratios of PMMA : PUA (3 : 7, 4 : 6, and 5 : 5 in the 12 wt% solutions). Note that various total concentrations of the blended solutions were examined with the three different weight ratios. Although the blends with the varied concentrations showed similar tendencies according to the weight ratios, the 12 wt% solution most specifically revealed morphological changes in the blended films. Island-like features with the diameter of ~ 600 nm were clearly observed when the PMMA mass fraction (φ) was 0.3 (i.e., PMMA/PUA = 30/70) as shown in Figure 4(a), and the size of island-like features became larger as the value of φ increased. When the value of φ increased up to

~ 0.4 , the island-like PMMA features were finally connected to each other and formed larger domains (Figure 4(b)). Island-like features completely disappeared at $\varphi = 0.5$, and hole-like features with the diameter of ~ 500 nm were rather found as shown in Figure 4(c). The hole diameter decreased to ~ 100 nm as the value of φ increased up to ~ 0.6 . It is worth noting that only one phase was observed on the surface without any evidence of phase separation when the value of φ was below 0.2 or above 0.8, due to the excess amount of one component in the blends. These results imply that morphology of phase-separated structure with varied features can be easily controlled by changing composition of the blends.

4. Conclusions

Spin-coated immiscible PMMA and UV curable PUA blends are phase-separated owing to the differences of solvent evaporation rate for each polymer and polymer solubility in the common solvent. The cross-linked PUA in the polymer-blended films provides strong chemical stability in the solvents such as THF, and thus target materials for dissolution can be selectively available via a simple curing process. The substrate exposure after film deposition also can be achieved by the selective dissolution without additional etching process, which may lead to further applications such as antireflection layers. In addition, morphology of the PMMA/PUA blends can be easily controlled by changing composition (i.e., total concentration and weight ratio) of the blends. The morphological controls include domain size, height, and nanoscale features such as island-like and hole-like structures. We anticipate that these controllable structures originating from the phase separation will be applied to various engineering fields such as soft lithography.

Conflict of Interests

The authors declare that there is no conflict of interests regarding the publication of this paper.

Authors' Contribution

Ju-Hyung Kim and Joon H. Kim contributed equally to this work.

Acknowledgment

This work was supported by a research grant of Pukyong National University (Year 2014).

References

- [1] M. Boltau, S. Walheim, J. Mlynek, G. Krausch, and U. Steiner, "Surface-induced structure formation of polymer blends on patterned substrates," *Nature*, vol. 391, no. 6670, pp. 877–879, 1998.
- [2] S. Walheim, E. Schäffer, J. Mlynek, and U. Steiner, "Nanophase-separated polymer films as high-performance antireflection coatings," *Science*, vol. 283, no. 5401, pp. 520–522, 1999.
- [3] S. Nilsson, A. Bernasik, A. Budkowski, and E. Moons, "Morphology and phase segregation of spin-casted films of polyfluorene/PCBM blends," *Macromolecules*, vol. 40, no. 23, pp. 8291–8301, 2007.
- [4] C. Huang, J. Gao, W. Yu, and C. Zhou, "Phase separation of poly(methyl methacrylate)/poly(styrene-co-acrylonitrile) blends with controlled distribution of silica nanoparticles," *Macromolecules*, vol. 45, no. 20, pp. 8420–8429, 2012.
- [5] S. Kato and A. Sato, "Micro/nanotextured polymer coatings fabricated by UV curing-induced phase separation: creation of superhydrophobic surfaces," *Journal of Materials Chemistry*, vol. 22, no. 17, pp. 8613–8621, 2012.
- [6] S. Walheim, M. Böltau, J. Mlynek, G. Krausch, and U. Steiner, "Structure formation via polymer demixing in spin-cast films," *Macromolecules*, vol. 30, no. 17, pp. 4995–5003, 1997.
- [7] K. Tanaka, A. Takahara, and T. Kajiyama, "Film thickness dependence of the surface structure of immiscible polystyrene/poly(methyl methacrylate) blends," *Macromolecules*, vol. 29, no. 9, pp. 3232–3239, 1996.
- [8] D. B. Hall, P. Underhill, and J. M. Torkelson, "Spin coating of thin and ultrathin polymer films," *Polymer Engineering & Science*, vol. 38, no. 12, pp. 2039–2045, 1998.
- [9] D. W. Schubert and T. Dunkel, "Spin coating from a molecular point of view: its concentration regimes, influence of molar mass and distribution," *Materials Research Innovations*, vol. 7, no. 5, pp. 314–321, 2003.
- [10] J. S. Chiou, J. W. Barlow, and D. R. Paul, "Miscibility of bisphenol-a polycarbonate with poly(methyl methacrylate)," *Journal of Polymer Science Part B: Polymer Physics*, vol. 25, no. 7, pp. 1459–1471, 1987.
- [11] J.-B. Lhoest, P. Bertrand, L. T. Weng, and J.-L. Dewez, "Combined time-of-flight secondary ion mass spectrometry and X-ray photoelectron spectroscopy study of the surface segregation of poly(methyl methacrylate) (PMMA) in bisphenol A polycarbonate/PMMA blends," *Macromolecules*, vol. 28, no. 13, pp. 4631–4637, 1995.
- [12] M. C. Davies, K. M. Shakesheff, A. G. Shard et al., "Surface analysis of biodegradable polymer blends of poly(sebacic anhydride) and poly(DL-lactic acid)," *Macromolecules*, vol. 29, no. 6, pp. 2205–2212, 1996.
- [13] P. Wang and J. T. Koberstein, "Morphology of immiscible polymer blend thin films prepared by spin-coating," *Macromolecules*, vol. 37, no. 15, pp. 5671–5681, 2004.
- [14] T. Kikuchi, M. Kudo, C. Jing, T. Tsukada, and M. Hozawa, "Electrohydrodynamic effect on phase separation morphology in polymer blend films," *Langmuir*, vol. 20, no. 4, pp. 1234–1238, 2004.
- [15] M. Ibn-Elhaj and M. Schadt, "Optical polymer thin films with isotropic and anisotropic nano-corrugated surface topologies," *Nature*, vol. 410, no. 6830, pp. 796–799, 2001.
- [16] J. Kim, M. Inoue, L. Zhao et al., "Tunable and flexible solvent-free liquid organic distributed feedback lasers," *Applied Physics Letters*, vol. 106, no. 5, Article ID 053302, 2015.
- [17] S.-J. Choi, P. J. Yoo, S. J. Baek, T. W. Kim, and H. H. Lee, "An ultraviolet-curable mold for Sub-100-nm lithography," *Journal of the American Chemical Society*, vol. 126, no. 25, pp. 7744–7745, 2004.
- [18] S.-J. Choi, H. N. Kim, W. G. Bae, and K.-Y. Suh, "Modulus- and surface energy-tunable ultraviolet-curable polyurethane acrylate: properties and applications," *Journal of Materials Chemistry*, vol. 21, no. 38, pp. 14325–14335, 2011.
- [19] J.-H. Kim, S. H. Hong, K.-D. Seong, and S. Seo, "Fabrication of organic thin-film transistors on three-dimensional substrates using free-standing polymeric masks based on soft lithography," *Advanced Functional Materials*, vol. 24, no. 16, pp. 2404–2408, 2014.
- [20] A. Bernasik, J. Włodarczyk-Miśkiewicz, W. Łuzny et al., "Lamellar structures formed in spin-cast blends of insulating and conducting polymers," *Synthetic Metals*, vol. 144, no. 3, pp. 253–257, 2004.
- [21] J. Jaczewska, A. Budkowski, A. Bernasik et al., "Humidity and solvent effects in spin-coated polythiophene-polystyrene blends," *Journal of Applied Polymer Science*, vol. 105, no. 1, pp. 67–79, 2007.

Research Article

Detection of Biomarkers Using LSPR Substrate with Gold Nanoparticle Array

**Young Min Bae, Seung Oh Jin, Insoo Kim, Ki Young Shin,
Duchang Heo, and Dong-Goo Kang**

Korea Electrotechnology Research Institute, 111 Hangeul-ro, Ansan 426-170, Republic of Korea

Correspondence should be addressed to Young Min Bae; kimbym@keri.re.kr

Received 3 July 2015; Revised 8 September 2015; Accepted 13 September 2015

Academic Editor: Fangfang Sun

Copyright © 2015 Young Min Bae et al. This is an open access article distributed under the Creative Commons Attribution License, which permits unrestricted use, distribution, and reproduction in any medium, provided the original work is properly cited.

In the biosensing platform, label-free detection technique provides advantages such as the short analysis time and the cost-effectiveness. In this study, we showed the feasibility of the LSPR substrate with gold nanoparticle array for detecting low density lipoprotein (LDL) and high density lipoprotein (HDL) without labeling. The LSPR substrate was fabricated through the lift-off process with the anodized alumina mask, and its LSPR phenomenon was observed by measuring the optical transmission of substrate. The antibodies were immobilized on the gold nanoparticle array via the chemical binding, in which the 11-MUA was used as the linker to bind the antibodies. The binding of antibodies was confirmed by observing the shift of LSPR peak of the substrate. Finally, with the LSPR substrates with the antibodies immobilized, the detection of LDL and HDL was investigated. As a result, LDL and HDL could be detected in the clinically available concentration range, respectively.

1. Introduction

Immunoassay based on antigen-antibody binding is prevalently used for detecting several kinds of analytes such as protein, pathogens, or small molecules. As the method can be quite rapid, it has been applied to develop a point-of-care diagnostic device of which the operation should be simply implemented [1].

The labeling-based detection techniques have been widely employed for detecting the antibody-antigen binding in the point-of-care diagnostic device [1, 2]. For example, a fluorescence detection technique has been used to detect antibody-antigen binding on a solid surface. In the technique, the labeling step, in which the complex of antibody-antigen binding is labeled with the probe antibody, conjugated with fluorescence molecule. Basically, the labeling techniques involving the use of fluorescence, ELISA, and isotropic labeling require one or two intermediate steps for labeling. So, the simpler detection technique should be developed for implementing the point-of-care diagnostic device.

Label-free detection technique would provide a direct approach to the detection of protein-protein binding. Electrochemical impedance technique, surface plasmon resonance (SPR), and mass-sensitive cantilever detection have all been applied to label-free detection methods [3–5]. In particular, the SPR technique has been used as a versatile detection tool for the study of the kinetics of receptor-ligand interaction [6]. In the conventional SPR technique, the plasmon resonance is excited by the light beam incident onto the interface between a metal and a dielectric medium, and the plasmon resonance condition such as the incident angle is attributed to the refractive index in the dielectric medium. So, the complicated optical system or mechanical structure is required to implement the SPR device [7]. On the other hands, the localized surface plasmon resonance (LSPR) is observed in the metal nanoparticle, not presented in the bulk metal [8]. When light is incident on a surface with metal nanoparticles smaller than the wavelength of light, the collective oscillation of conduction electron in them with a resonant frequency is induced. The LSPR is

dependent on the dielectric properties of the local environment surrounding the nanoparticles [9]. This property allows the LSPR to provide the label-free detection method for an antigen-antibody reaction [10]. Also, as the LSPR of metal nanoparticle is easily observed by measuring the adsorption spectrum, the biosensor platforms based on the LSPR can be simply implemented.

The substrate, onto which the nanosized metal structures exhibiting the LSPR phenomenon are deposited, should be developed for the LSPR-based biosensor. There have been several methods reported to fabricate the LSPR substrate, such as the direct deposition of nanoparticles or nanorods in solution onto a solid surface, the growth of nanoparticles on the surface, nanosphere lithography, and nanoimprint lithography [9–14]. Recently, we reported the fabrication of gold nanoparticle array on solid surface [15]. The gold nanoparticle arrays were simply fabricated via the lift-off process, and the absorption peak showing the maximum absorbance in the absorption spectrum (defined as the LSPR peak) could be regulated in the wavelength range of 500–700 nm with the control of thickness.

In this study, we demonstrate the application of the gold nanoparticle array fabricated by the lift-off process to detection of two biomarkers, low density lipoprotein (LDL) and high density lipoprotein (HDL). They are the important biomarkers for diagnosing the cardiovascular diseases [16]. The immobilization of antibody onto the gold nanoparticle array was confirmed by observing the change of the LSPR peak. In addition, we showed the applicability of the gold nanoparticle array to the detection of biomarkers by measuring the change of the LSPR peak with the increasing concentration of the biomarkers.

2. Materials and Methods

2.1. Materials. LDL and antibody against LDL and HDL and antibody against HDL were purchased from Abcam plc company. 11-mercaptoundecanoic acid (11-MUA), 1-ethyl-3-(3-dimethylaminopropyl)carbodiimide hydrochloride (EDAC), and human serum were purchased from Sigma-Aldrich company. The other chemicals used in this study were reagent grade and were obtained commercially.

2.2. Fabrication of Gold Nanoparticle Array. The gold nanoparticle array was fabricated by the method reported previously [15]. After a glass substrate (size: 24 × 24 mm) was cleaned with the piranha solution (1 : 4 of hydrogen peroxide and sulfuric acid), 1 μm thick aluminum film was deposited by electron beam evaporation (EI-5, ULVAC Co., USA). A two-step anodization process was executed to form the alumina mask on the substrate as described elsewhere [17, 18]. In the first anodization process, after the substrate and the carbon electrode were placed in a beaker of 0.3 M oxalic acid, 40 V was applied between the substrate and the carbon electrode to anodize the aluminum film for 13 minutes at 5°C. The alumina film formed on the substrate was removed by immersing it in a solution of 6 wt% H₃PO₄ and 1.5 wt% CrO₃ at 60°C. After the substrate was rinsed and dried, the second anodization process was executed with the aluminum

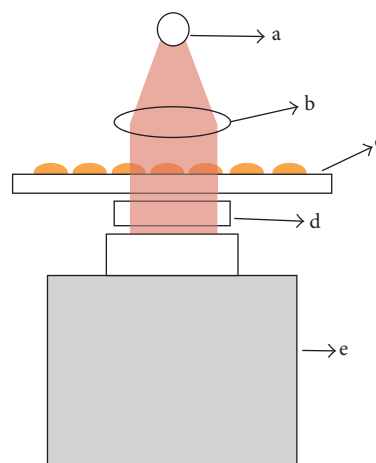


FIGURE 1: Hand-made equipment for measuring the optical transmission of substrate (a: halogen lamp, b: collimator, c: substrate with gold nanodot array, d: optical attenuator, and e: CCD-type spectrophotometer).

film remaining on the substrate under the same conditions as the first anodization. Finally, the substrate was immersed in a beaker of 5 wt% H₃PO₄ to remove the barrier layer and widen the diameter of the pores formed in the alumina film [19].

The gold nanoparticle array was fabricated using the alumina mask lift-off process. To fabricate the gold nanoparticle array, a 2 nm thick layer of chromium and a gold layer were sequentially deposited via electron beam evaporation onto the substrate. After depositing the gold layer, the gold nanoparticle array on the substrate was completed by removing the alumina mask by immersing the substrate in 5 wt% H₃PO₄ at 30°C for 60 minutes.

2.3. Immobilization of Antibody. The antibodies against biomarkers were covalently immobilized on the surface of each gold nanoparticle by the method reported elsewhere [20]. The glass substrate with the gold nanoparticle array was cleaned with ethanol, followed by the oxygen plasma treatment. The monolayer of 11-mercaptoundecanoic acid (11-MUA) was deposited on the gold nanoparticle array by submersing the substrate in the ethanol solution containing 150 mM 11-MUA for at least 12 hours. To bind the antibody covalently, the carboxylic group of the monolayer was activated by submersing the substrate modified with 11-MUA into a solution of 10% EDAC in water/ethanol (10/1 v/v) for 2 hours at room temperature. The immobilization process of antibody was completed by applying the activated surface to 20 μg/mL antibody solution in the phosphate buffer saline (PBS) buffer for at least 2 hours, followed by cleaning the surface.

2.4. Experimental Setup. Absorption spectrums of LSPR substrate were acquired with the hand-made device equipped with the commercial components as shown in Figure 1. The device is composed of the CCD-array type spectrophotometer (BRC115A, B&W Tek Inc.) and the 10 W tungsten lamp (Osram Co.) connected with the collimator and configured to

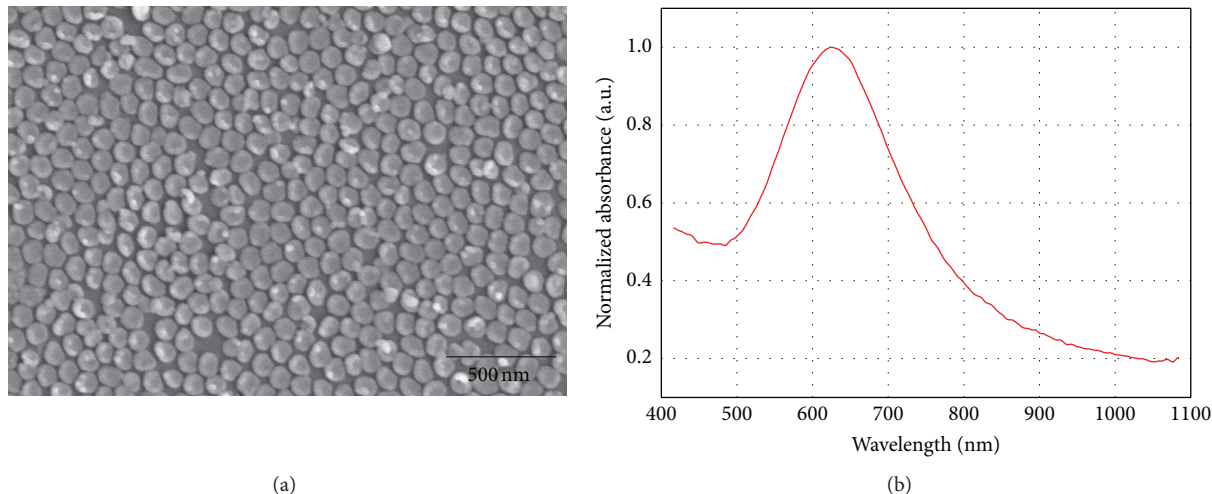


FIGURE 2: (a) Scanning electron micrograph of 10 nm thick gold nanodot array formed on glass substrate. (b) Typical absorption spectrum of the substrate with gold nanodot array.

measure the transmission of the substrate. The transmission value measured was converted into the absorbance value by Beer's law.

3. Results and Discussion

3.1. Gold Nanoparticle Array. As mentioned above, the gold nanoparticle array on the glass substrate was fabricated with the lift-off process of the alumina mask [15]. Previously, we reported that the sensitivity of LSPR substrate defined as the ratio of the shift of LSPR peak to the refractive index unit (RIU) of the medium surrounding the gold nanoparticle array was changed with the thickness of gold layer deposited, and the maximum sensitivity was at the deposition thickness of 10 nm. Here, we used the gold nanoparticle array with the deposition thickness of 10 nm for the LSPR biosensing as shown in Figure 2(a). The diameter of each gold nanoparticle was 94.9 ± 5.9 nm, and the typical absorption spectrum of the substrate was shown in Figure 2(b), in which the position of LSPR peak of the gold nanoparticle array was 626.7 ± 5.9 nm, which is calculated with the centroid algorithm [21].

3.2. Immobilization of Antibody. Several techniques for binding antibody to the substrate have been reported, and are divided into two categories: the physical binding and the chemical binding. The chemical binding technique, in which antibody is covalently immobilized onto the substrate, has been found to show good reproducibility and coverage [22]. In this study, the chemical binding in which the monolayer of 11-MUA was used as the linker to bind antibody was used in order to immobilize the antibody on the gold nanoparticle array. Figure 3 shows the scheme of the immobilization of antibody used in this study. The monolayer of 11-MUA with the carboxylic acid as the terminal group was self-assembled on the surface of each gold nanoparticle. The substrate modified with the 11-MUA monolayer was treated with EDAC to allow the chemical binding between the lysine residues of antibody and the carboxylic group via the amide

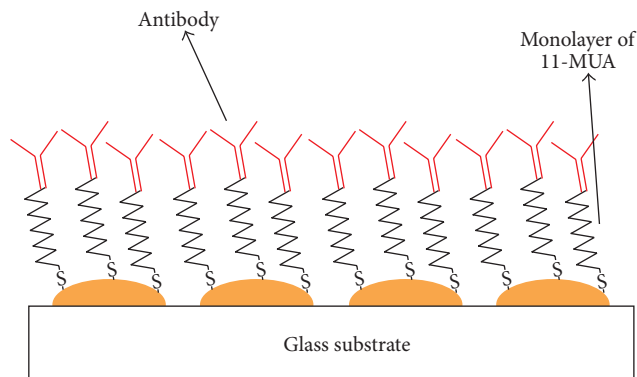


FIGURE 3: Scheme for immobilizing the antibody on the substrate.

bonding. Figures 4(a) and 4(b) show the change of absorption spectra according to sequentially depositing the 11-MUA and antibody onto the substrate. Following the deposition of the monolayer of 11-MUA, the position of LSPR peak was shifted from 626.7 ± 5.9 nm (the LSPR peak position of substrate without the monolayer) to 641.6 ± 4.3 nm. It is known that the closely packed 2-dimensional molecular layer of 11-MUA is formed on the substrate by the van der Waals attractive force among the long alkyl chains [23]. Therefore, the shift of peak position is attributed to the change of RIU near the gold nanoparticle array. After immobilizing the antibody against LDL onto the monolayer of 11-MUA, the LSPR peak was shifted to 676.8 ± 4.2 nm. Also, in case of immobilization of antibody against HDL, the LSPR peak of substrate was shifted to 671.1 ± 5.6 nm.

3.3. Detection of Biomarkers. LDL is the major carrier of cholesterol in the blood, and the accumulation of it on the vessel wall constitutes one of the initial steps in arteriosclerosis [24]. So, the increased level of LDL in blood is associated with atherosclerosis. On the other hand, HDL is

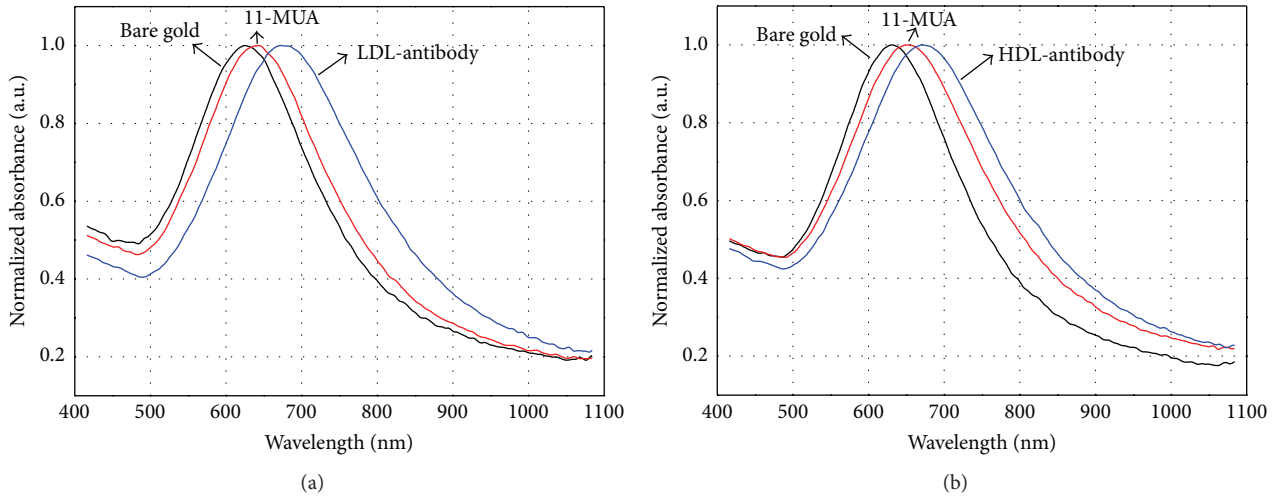


FIGURE 4: Absorption spectra of substrate with depositing the 11-MUA monolayer and immobilizing the antibodies on the monolayer. (a) Immobilization of the antibody against LDL. (b) Immobilization of the antibody against HDL.

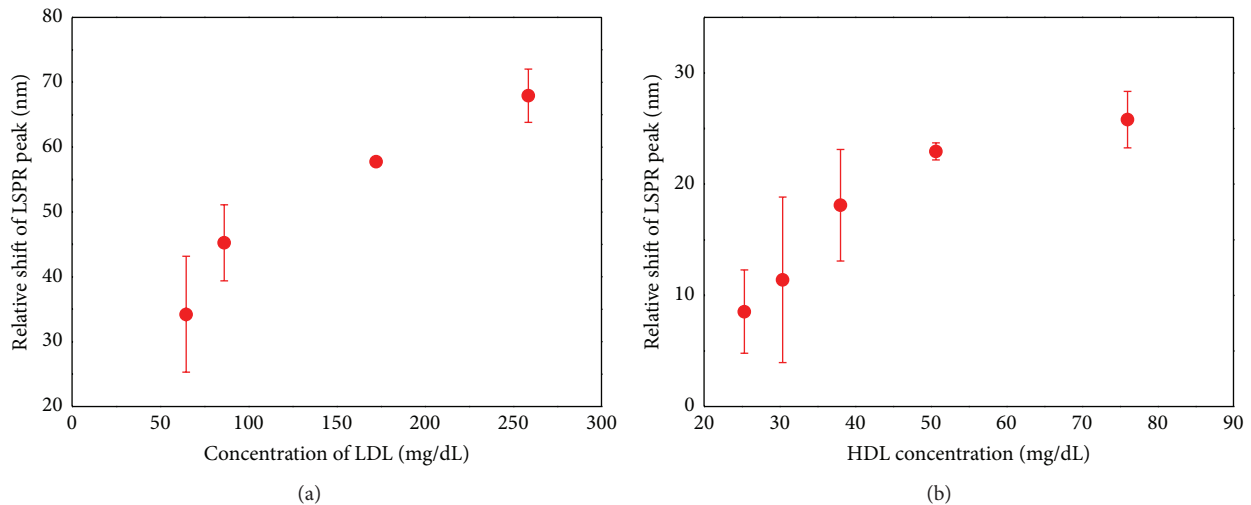


FIGURE 5: Relative shifts of LSPR peak corresponding with reacting with the varying concentration of biomarkers: LDL (a) and HDL (b).

the lipoprotein which has been shown to be able to prevent and reverse arteriosclerosis [16]. So, the level of HDL in blood should be higher than the normal concentration level. Therefore, as LDL and HDL are the import biomarkers to diagnose or monitor the cardiovascular diseases, the detections of them are routinely executed in the laboratory medicine. Here, the detection of LDL and HDL with the LSPR of the gold nanoparticle array substrate was demonstrated.

In the experiment, the LDL and HDL were diluted into the varying concentrations in the human serum purchased from Sigma-Aldrich Co. Then, the substrate with the antibody immobilized was incubated in the biomarker solutions with the varying concentration for 1 hour with gently stirring. After being incubated, the substrate was cleaned with the water, followed by drying under the nitrogen gas. The absorption spectrum of substrate was acquired with the equipment described above. Figure 5(a) shows the relative

shift of LSPR peak as a function of the concentration of LDL. The relative shift of LSPR peak in the vertical axis of the graphs meant the amount of the shift of LSPR peak from the LSPR peak of substrate with the antibody immobilized. The concentrations of LDL prepared in the experiment were 64.6, 86.2, 172.3, and 258.5 mg/dL, respectively. In the range, the relative shift of LSPR peak increased with the increasing concentration of LDL. According to the American Heart Association, the optimal level of LDL in blood is lower than 100 mg/dL, and the value higher than 200 mg/dL is very high LDL level, corresponding to highest increased rates of cardiovascular disease event [25]. The experimental result shows that our LSPR substrate can be used to detect the LDL in the clinical available range of concentration. Figure 5(b) shows the relative shift of LSPR peak as a function of the concentration of HDL. Similar to the experiment of LDL detection, the LSPR peak was positively shifted with the

increasing concentration of HDL. In particular, the relative shift of LSPR is linearly proportional to the concentration in the low concentration range. Contrary to the LDL level, it is known that the optimal level of HDL in blood is higher than 60 mg/dL, and the values under 40 mg/dL for men and under 50 mg/dL for women are risky for heart diseases [25]. The experimental result shows the LSPR substrate with the gold nanoparticle array can be applied to detect the HDL.

In this study, we showed the applicability of the substrate with the gold nanoparticle array to detect the LDL and HDL. The LSPR substrate for the development of biosensor provides two advantages over the conventional analysis [26]. At first, the detection time is short because the step for labeling fluorophores or ELISA is omitted. Moreover, as the probe antibody used for labeling is not needed, it is cost-effective. Second, the equipment for readout is simple. As described above, the antigen-antibody binding can be simply detected by measuring the optical transmission of substrate. In reality, we constructed the equipment for measuring the transmission with the engineering technique not complicated. Our gold nanoparticle array and its fabrication method provide the simple and powerful solution to develop the LSPR-based biosensor. However, there are several hurdles to overcome to apply the LSPR substrate in the clinical area. The sample for analyzing in the clinical diagnostics is the blood, which is the complex of white and red blood cells, and the serum with several proteins. In particular, as the high concentration of red blood cells in blood affects the measurement of transmission, only the plasma should be extracted from blood before analyzing the biomarker. Recently, the microfluidics technology for extracting the plasma from the blood has been reported [27, 28]. In our opinion, the point-of-care device for biosensing LDL and HDL can be developed with the strategy of allocating the LSPR substrate in the downstream of plasma in the microfluidic device.

4. Conclusions

In this study, we showed the feasibility of the LSPR substrate with gold nanoparticle array to detect LDL and HDL, which are the biomarkers for diagnosing and monitoring the cardiovascular diseases. The LSPR substrate was fabricated through the lift-off process with the anodized alumina mask, and its LSPR phenomenon was observed by measuring the optical transmission of substrate. The antibodies were immobilized on the gold nanoparticle array via the chemical binding, in which the 11-MUA was used as the linker to bind the antibodies. The binding of antibodies was confirmed by observing the shift of LSPR peak of the substrate. Finally, with the LSPR substrates with the antibodies immobilized, the detection of LDL and HDL was investigated. As a result, LDL and HDL could be detected in the clinically available concentration range, respectively.

When the LSPR substrate is used for the development of biosensor, it provides the advantages such as the fast detection protocol and the cost-effectiveness. In particular, by fusing the LSPR substrate and the microfluidic device, the development of point-of-care diagnostic device based on the immunoassay can be implemented in the view of practice.

Conflict of Interests

The authors declare that there is no conflict of interests regarding the publication of this paper.

Acknowledgment

This research was supported by Korea Electrotechnology Research Institute (KERI) Primary Research Program through the Korea Research Council for Industrial Science & Technology (ISTK) funded by the Ministry of Science, ICT and Future Planning (MSIP) (no. 15-12-N0101-29).

References

- [1] L. Gervais and E. Delamarche, "Toward one-step point-of-care immunodiagnostics using capillary-driven microfluidics and PDMS substrates," *Lab on a Chip*, vol. 9, no. 23, pp. 3330–3337, 2009.
- [2] H. Xie, J. Mire, Y. Kong et al., "Rapid point-of-care detection of the tuberculosis pathogen using a BlaC-specific fluorogenic probe," *Nature Chemistry*, vol. 4, no. 10, pp. 802–809, 2012.
- [3] E. Stern, A. Vacic, N. K. Rajan et al., "Label-free biomarker detection from whole blood," *Nature Nanotechnology*, vol. 5, no. 2, pp. 138–142, 2010.
- [4] Y. M. Bae, S. Y. Son, K.-H. Lee, K. Kim, S. K. Seol, and D. Kim, "Enhancement of the sensitivity of surface plasmon resonance biosensor by modifying the metal surface," *Journal of Biomedical Nanotechnology*, vol. 9, no. 6, pp. 1060–1064, 2013.
- [5] G. Wu, R. H. Datar, K. M. Hansen, T. Thundat, R. J. Cote, and A. Majumdar, "Bioassay of prostate-specific antigen (PSA) using microcantilevers," *Nature Biotechnology*, vol. 19, no. 9, pp. 856–860, 2001.
- [6] Y. Tang, R. Memaugh, and X. Zeng, "Nonregeneration protocol for surface plasmon resonance: study of high-affinity interaction with high-density biosensors," *Analytical Chemistry*, vol. 78, no. 6, pp. 1841–1848, 2006.
- [7] Y.-B. Shin, H. M. Kim, Y. Jung, and B. H. Chung, "A new palm-sized surface plasmon resonance (SPR) biosensor based on modulation of a light source by a rotating mirror," *Sensors and Actuators, B: Chemical*, vol. 150, no. 1, pp. 1–6, 2010.
- [8] K. A. Willets and R. P. Van Duyne, "Localized surface plasmon resonance spectroscopy and sensing," *Annual Review of Physical Chemistry*, vol. 58, pp. 267–297, 2007.
- [9] K. L. Kelly, E. Coronado, L. L. Zhao, and G. C. Schatz, "The optical properties of metal nanoparticles: the influence of size, shape, and dielectric environment," *Journal of Physical Chemistry B*, vol. 107, no. 3, pp. 668–677, 2003.
- [10] D. A. Gish, F. Nsiah, M. T. McDermott, and M. J. Brett, "Localized surface plasmon resonance biosensor using silver nanostructures fabricated by glancing angle deposition," *Analytical Chemistry*, vol. 79, no. 11, pp. 4228–4232, 2007.
- [11] J. N. Anker, W. P. Hall, O. Lyandres, N. C. Shah, J. Zhao, and R. P. Van Duyne, "Biosensing with plasmonic nanosensors," *Nature Materials*, vol. 7, no. 6, pp. 442–453, 2008.
- [12] C. L. Haynes and R. P. Van Duyne, "Nanosphere lithography: a versatile nanofabrication tool for studies of size-dependent nanoparticle optics," *Journal of Physical Chemistry B*, vol. 105, no. 24, pp. 5599–5611, 2001.

- [13] S.-W. Lee, K.-S. Lee, J. Ahn, J.-J. Lee, M.-G. Kim, and Y.-B. Shin, "Highly sensitive biosensing using arrays of plasmonic Au nanodisks realized by nanoimprint lithography," *ACS Nano*, vol. 5, no. 2, pp. 897–904, 2011.
- [14] M. E. Stewart, C. R. Anderton, L. B. Thompson et al., "Nanostructured plasmonic sensors," *Chemical Reviews*, vol. 108, no. 2, pp. 494–521, 2008.
- [15] Y. M. Bae, K.-H. Lee, J. Yang, and D. Heo, "Fabrication of gold nanodot array for the localized surface plasmon resonance," *Journal of Nanomaterials*, vol. 2014, Article ID 175670, 7 pages, 2014.
- [16] G. Siegel, M. Malmsten, D. Klüßendorf, and F. Michel, "A receptor-based biosensor for lipoprotein docking at the endothelial surface and vascular matrix," *Biosensors and Bioelectronics*, vol. 16, no. 9–12, pp. 895–904, 2001.
- [17] H. Masuda and K. Fukuda, "Ordered metal nanohole arrays made by a two-step replication of honeycomb structures of anodic alumina," *Science*, vol. 268, no. 5216, pp. 1466–1468, 1995.
- [18] K. Nielsch, J. Choi, K. Schwirn, R. B. Wehrspohn, and U. Gösele, "Self-ordering regimes of porous alumina: the 10% porosity rule," *Nano Letters*, vol. 2, pp. 677–680, 2002.
- [19] B. Yan, H. T. M. Pham, Y. Ma, Y. Zhuang, and P. M. Sarro, "Fabrication of in situ ultrathin anodic aluminum oxide layers for nanostructuring on silicon substrate," *Applied Physics Letters*, vol. 91, no. 5, Article ID 053117, 2007.
- [20] Y. M. Bae, B.-K. Oh, W. Lee, W. H. Lee, and J.-W. Choi, "Immunosensor for detection of *Yersinia enterocolitica* based on imaging ellipsometry," *Analytical Chemistry*, vol. 76, no. 6, pp. 1799–1803, 2004.
- [21] S. Zhan, X. Wang, and Y. Liu, "Fast centroid algorithm for determining the surface plasmon resonance angle using the fixed-boundary method," *Measurement Science and Technology*, vol. 22, no. 2, Article ID 025201, 2011.
- [22] Y. M. Bae, B.-K. Oh, W. Lee, W. H. Lee, and J.-W. Choi, "Study on orientation of immunoglobulin G on protein G layer," *Biosensors and Bioelectronics*, vol. 21, no. 1, pp. 103–110, 2005.
- [23] A. Ulman, "Formation and structure of self-assembled monolayers," *Chemical Reviews*, vol. 96, no. 4, pp. 1533–1554, 1996.
- [24] P. A. Serra, *Biosensors for Detection of Low-Density Lipoprotein and Its Modified Forms in Biosensors for Health, Environment and Biosecurity*, chapter 9, Intech, Rijeka, Croatia, 2011.
- [25] S. M. Grundy, G. J. Balady, M. H. Criqui et al., "When to start cholesterol-lowering therapy in patients with coronary heart disease," *Circulation*, vol. 95, no. 6, pp. 1683–1685, 1997.
- [26] Y. Hong, Y.-M. Huh, D. S. Yoon, and J. Yang, "Nanobiosensors based on localized surface plasmon resonance for biomarker detection," *Journal of Nanomaterials*, vol. 2012, Article ID 759830, 13 pages, 2012.
- [27] V. VanDelinder and A. Groisman, "Separation of plasma from whole human blood in a continuous cross-flow in a molded microfluidic device," *Analytical Chemistry*, vol. 78, no. 11, pp. 3765–3771, 2006.
- [28] K. K. Lee and C. H. Ahn, "A new on-chip whole blood/plasma separator driven by asymmetric capillary forces," *Lab on a Chip*, vol. 13, no. 16, pp. 3261–3267, 2013.